NUREG/CR-4914
SAND87-0940

The Influence of Selected Containment Structures on Debris Dispersal and Transport Following High Pressure Melt Ejection from the Reactor Vessel

Prepared by M. Pilch, W. W. Tarbell, J. E. Brockmann

Sandia National Laboratories

Prepared for
U.S. Nuclear Regulatory Commission

When printing a copy of any digitized SAND Report, you are required to update the markings to current standards.

NOTICE

This report was prepared as an account of work sponsored by an agency of the United States Government. Neither the United States Government nor any agency thereof, or any of their employees, makes any warranty, expressed or implied, or assumes any legal liability of responsibility for any third party's use, or the results of such use, of any information, apparatus, product or process disclosed in this report, or represents that its use by such third party would not infringe privately owned rights.

NOTICE

Availability of Reference Materials Cited in NRC Publications

Most documents cited in NRC publications will be available from one of the following sources:

1. The NRC Public Document Room, 1717 H Street, N.W.
   Washington, DC 20555
2. The Superintendent of Documents, U.S. Government Printing Office, Post Office Box 37082, Washington, DC 20013-7082
3. The National Technical Information Service, Springfield, VA 22161

Although the listing that follows represents the majority of documents cited in NRC publications, it is not intended to be exhaustive.

Referenced documents available for inspection and copying for a fee from the NRC Public Document Room include NRC correspondence and internal NRC memoranda; NRC Office of Inspection and Enforcement bulletins, circulars, information notices, inspection and investigation notices; Licensee Event Reports; vendor reports and correspondence; Commission papers; and applicant and licensee documents and correspondence.

The following documents in the NUREG series are available for purchase from the GPO Sales Program: formal NRC staff and contractor reports, NRC-sponsored conference proceedings, and NRC booklets and brochures. Also available are Regulatory Guides, NRC regulations in the *Code of Federal Regulations*, and *Nuclear Regulatory Commission Issuances*.

Documents available from the National Technical Information Service include NUREG series reports and technical reports prepared by other federal agencies and reports prepared by the Atomic Energy Commission, forerunner agency to the Nuclear Regulatory Commission.

Documents available from public and special technical libraries include all open literature items, such as books, journal and periodical articles, and transactions. *Federal Register* notices, federal and state legislation, and congressional reports can usually be obtained from these libraries.

Documents such as theses, dissertations, foreign reports and translations, and non-NRC conference proceedings are available for purchase from the organization sponsoring the publication cited.

Single copies of NRC draft reports are available free, to the extent of supply, upon written request to the Division of Information Support Services, Distribution Section, U.S. Nuclear Regulatory Commission, Washington, DC 20555.

Copies of industry codes and standards used in a substantive manner in the NRC regulatory process are maintained at the NRC Library, 7920 Norfolk Avenue, Bethesda, Maryland, and are available there for reference use by the public. Codes and standards are usually copyrighted and may be purchased from the originating organization or, if they are American National Standards, from the American National Standards Institute, 1430 Broadway, New York, NY 10018.

NUREG/CR-4914
SAND87-0940
R3, R4

The Influence of Selected Containment Structures on Debris Dispersal and Transport Following High Pressure Melt Ejection from the Reactor Vessel

Manuscript Completed: July 1988
Date Published: September 1988

Prepared by
M. Pilch, W. W. Tarbell, J. E. Brockmann

Sandia National Laboratories
Albuquerque, NM 87185

Prepared for
Division of Systems Research
Office of Nuclear Regulatory Research
U.S. Nuclear Regulatory Commission
Washington, DC 20555
NRC FIN A1406

ABSTRACT

High pressure expulsion of molten core debris from the reactor pressure vessel may result in dispersal of the debris from the reactor cavity. In most plants, the cavity exits into the containment such that the debris impinges on structures. Retention of the debris on the structures may affect the further transport of the debris throughout the containment. Two tests were done with scaled structural shapes placed at the exit of 1:10 linear scale models of the Zion cavity. The results show that the debris does not adhere significantly to structures. The lack of retention is attributed to splashing from the surface and reentrainment in the gas flowing over the surface. These processes are shown to be applicable to reactor scale.

A third experiment was done to simulate the annular gap between the reactor vessel and cavity wall. Debris collection showed that the fraction of debris exiting through the gap was greater than the gap-to-total flow area ratio. Film records indicate that dispersal was primarily by entrainment of the molten debris in the cavity.

TABLE OF CONTENTS

		Page
1.	INTRODUCTION	1
2.	THE HIPS-3J EXPERIMENT	6
	2.1 Apparatus	6
	2.2 Instrumentation	9
	2.3 Initial Conditions	15
	2.4 Experiment Results and Analyses	15
	2.4.1 Camera Coverage	15
	2.4.2 Pressurization and Blowdown History of the Melt Generator	19
	2.4.3 Structure Interactions	27
3.	THE HIPS-7C EXPERIMENT	32
	3.1 Apparatus	32
	3.2 Instrumentation	32
	3.3 Initial Conditions	37
	3.4 Experiment Results and Analyses	
	3.4.1 Camera Coverage	37
	3.4.2 Pressurization and Blowdown History of the Melt Generator	42
	3.4.3 Structure Interactions	46
	3.4.4 Aerosols	53
4.	THE HIPS-8C EXPERIMENT	59
	4.1 Apparatus	59
	4.2 Instrumentation	62
	4.3 Initial Conditions	64
	4.4 Experiment Results and Analyses	64
	4.4.1 Camera Coverage	67
	4.4.2 Pressurization and Blowdown History of the Melt Generator	67
	4.4.3 Structure Interactions	73
5.	SUMMARY AND CONCLUSIONS	77
6.	REFERENCES	79

LIST OF FIGURES

Figure		Page
1.1	Containment Building of the Zion Reactor Plant	3
2.1	HIPS-3J Test Configuration	7
2.2	Schematic of HIPS Melt Generator	8
2.3	Photo Detector Locations in the Lower Flange	10
2.4	Force Cell Location	13
2.5	X-Ray Cassette Locations	16
2.6	Camera Coverage	18
2.7	Pressurization History of the Melt Generator	20
2.8	Pressure History of the Melt Generator During Melt Ejection and Blowdown	22
2.9	Predicted Ablation of the Discharge Orifice	23
2.10	Upstream and Downstream Sides of the Discharge Orifice Compared to an Unused Orifice Plate	25
2.11	Comparison of Scaled Load Cell Measurements With Model Prediction	28
2.12	Pyrometer Measurements of Jet Exit Temperatures	29
3.1	Details of the Excavity Structure for the HIPS-7C Experiment	33
3.2	Orientation of the Test Apparatus Within the Test Chamber	34
3.3	Closeup Photo Sequence Taken From the Rear (Left Column) and Front (Right Column) of the Structure	40
3.4	Long Range Photo Sequence	41
3.5	Pressurization History of the Melt Generator	43
3.6	Blowdown History of the Melt Generator	44
3.7	Temperature Measurements Outside the Cavity Using a Two-Color Pyrometer	45

LIST OF FIGURES
(Continued)

Figure		Page
3.8	Pressure Measurements at Three Locations in the Cavity	47
3.9	Pretest and Posttest Comparison of Lower Assembly of the Cavity Mockup	49
3.10	Posttest View of the Melt Generator With Frozen Crust on its Surface	50
3.11	Pretest and Posttest Comparison of the Excavity Structure	52
3.12	Particle Trapping by Excavity Structure	54
3.13	Influence of Containment Structures on Debris Behavior	55
3.14	Aerosol Size Distribution	56
3.15	Fraction of Relocated Melt That is Aerosolized	58
4.1	Details of the Melt Generator, Transition Piece, and Cavity Configuration	60
4.2	Arrangement of the Test Apparatus in the Interaction Chamber	61
4.3	Debris Dispersal Through the Normal Cavity Exit	68
4.4	Debris Dispersal Through the Annular Gap	69
4.5	Pressurization History of the Melt Generator	70
4.6	Blowdown History of the Melt Generator	71
4.7	Temperature Measurement Outside the Cavity Using a Two-Color Pyrometer	72
4.8	Pressure Measurements in the Cavity	74

LIST OF TABLES

Table		Page
2.1	Summary of HIPS-3J Instrumentation	11
2.2	Summary of HIPS-3J Camera Coverage	14
2.3	HIPS-3J Initial Conditions	17
2.4	Photo Detector Signal Sequence	26
3.1	Summary of HIPS-7C Instrumentation	35
3.2	Summary of HIPS-7C Camera Coverage	38
3.3	HIPS-7C Initial Conditions	39
3.4	Posttest Debris Inventory	48
4.1	Summary of HIPS-8C Instrumentation	63
4.2	Summary of HIPS-8C Camera Coverage	65
4.3	HIPS-8C Initial Conditions	66

1. INTRODUCTION

The Zion Probabilistic Safety Study, ZPSS, (COMED, 1981) concludes that in over 75% of the accident sequences considered, failure of the reactor pressure vessel (RPV) occurs while the primary system remains at some elevated pressure. The point of failure is predicted to occur at one or more of the RPV instrument tube penetrations, resulting in a small orifice through which the molten core material can be ejected. Substantial ablation of the initially small orifice is predicted. As the molten material enters the cavity region beneath the RPV, it forms a pool of core debris that flows radially outward and into the tunnel region. The analysis suggests that this initial movement of debris coupled with the subsequent blowdown of the primary system will cause virtually all of the expelled core material to be dispersed into the containment regions. These processes are now termed High Pressure Melt Ejection (HPME).

High pressure accidents of this type are identified with either transient (T) or small-break loss-of-coolant (S) initiating events accompanied with failure of recirculation or upper head ejection, loss of feedwater, or station blackout. Based upon a number of probabilistic risk assessments, these accident initiators dominate the core damage frequency (IDCOR, 1984). For 14 reference plants, the estimated core melt frequency for S and T events is over 80% for pressurized water reactors (PWR) and over 90% for boiling water reactors (BWR).

The ZPSS assumes that debris dispersal from the reactor cavity will result in the formation of a relatively shallow bed of debris that is coolable by water located on the floor of the containment. This scenario eliminates the possibility of an extended interaction between the core debris and concrete basemat, thus eliminating the resulting gas and aerosol production that is associated with such interactions. Steam generated by quenching the debris bed is not sufficient to cause containment failure by overpressurization. The ZPSS methodology assumptions have also been used for other plants with essentially the same benign termination of the accident (CONED, 1982).

Study of the ZPSS and other similar documents shows that much of the information presented is conjectural with little experimental support. Many of the assumptions regarding debris dispersal are made without the benefit of appropriate test data. For this reason, research was initiated at Sandia National Laboratories (SNL) to perform an experimental and analytical investigation of the phenomena associated with this type of accident scenario, particularly the dispersal of debris from the reactor cavity. The ensuing effort was termed the High-Pressure Melt Streaming Program, HIPS, (Tarbell, Brockmann, and Pilch, 1984).

A number of scaled cavity experiments (Tarbell et al. 1986) conducted by the HIPS program have shown that debris is indeed

forcibly removed from the cavity. Unlike the film-like flow portrayed in the ZPSS, the debris emerged as fine particulate interspersed in a high-velocity gas stream. In all experiments utilizing concrete cavity models, over 95% of the debris ejected from the melt generator was also dispersed from the cavity. Flash X-ray images and samples of the debris collected following the tests reveal that the mass mean diameter of the dispersed debris particles is approximately 0.5 mm. High speed film records showed that the unimpeded flight of the debris was over 40 meters in elevation with impact on the ground nearly 60 meters downrange.

In some reactor containments, a significant portion of the material that would be swept from the reactor cavity could be carried into portions of the containment atmosphere where the debris might liberate its thermal and chemical (oxidation of metallic constituents) energy. This airborne energy exchange may significantly increase the containment pressure by heating the atmosphere or by boiling of codispersed water (thus increasing the mass of the containment atmosphere). The HIPS experiments and the earlier SPIT experiments have also shown that the energy exchange process is accompanied by intense generation of aerosols (Brockmann & Tarbell, 1984; Tarbell, et al., 1986). This is an important potential contributor to radionuclide release that has not been previously identified. The processes of containment heating and aerosol production have been termed Direct Containment Heating (DCH).

The CONTAIN code (Bergeron, et al., 1985), using an interim DCH model (Williams, et al., 1986), predicts that pressures sufficient to threaten some containments can be generated as a result of these airborne energy exchange processes. These calculations couple DCH with all other forms of exvessel severe accident phenomena. Modeling the influences of plant specific geometry is currently beyond the state-of-the art. Key uncertainties in these calculations are the amount of debris that interacts with the atmosphere and the length of time that the debris interacts with the atmosphere. Both these quantities may be strongly influenced by the plant specific structures near the cavity exit and throughout the plant.

The disparate opinions of the various researchers leads to several major unresolved issues associated with HPME and DCH: (1) the amount of debris dispersal from various cavity configurations, (2) the extent of debris transport beyond the cavity including interaction of the debris with containment structures, (3) the debris/atmosphere energy transfer processes, (4) the production of aerosols, and (5) rapid production and combustion of hydrogen. This report discusses the results of three HIPS experiments that focus on phenomena associated with the issue of debris dispersal and transport in the presence of 'structures.'

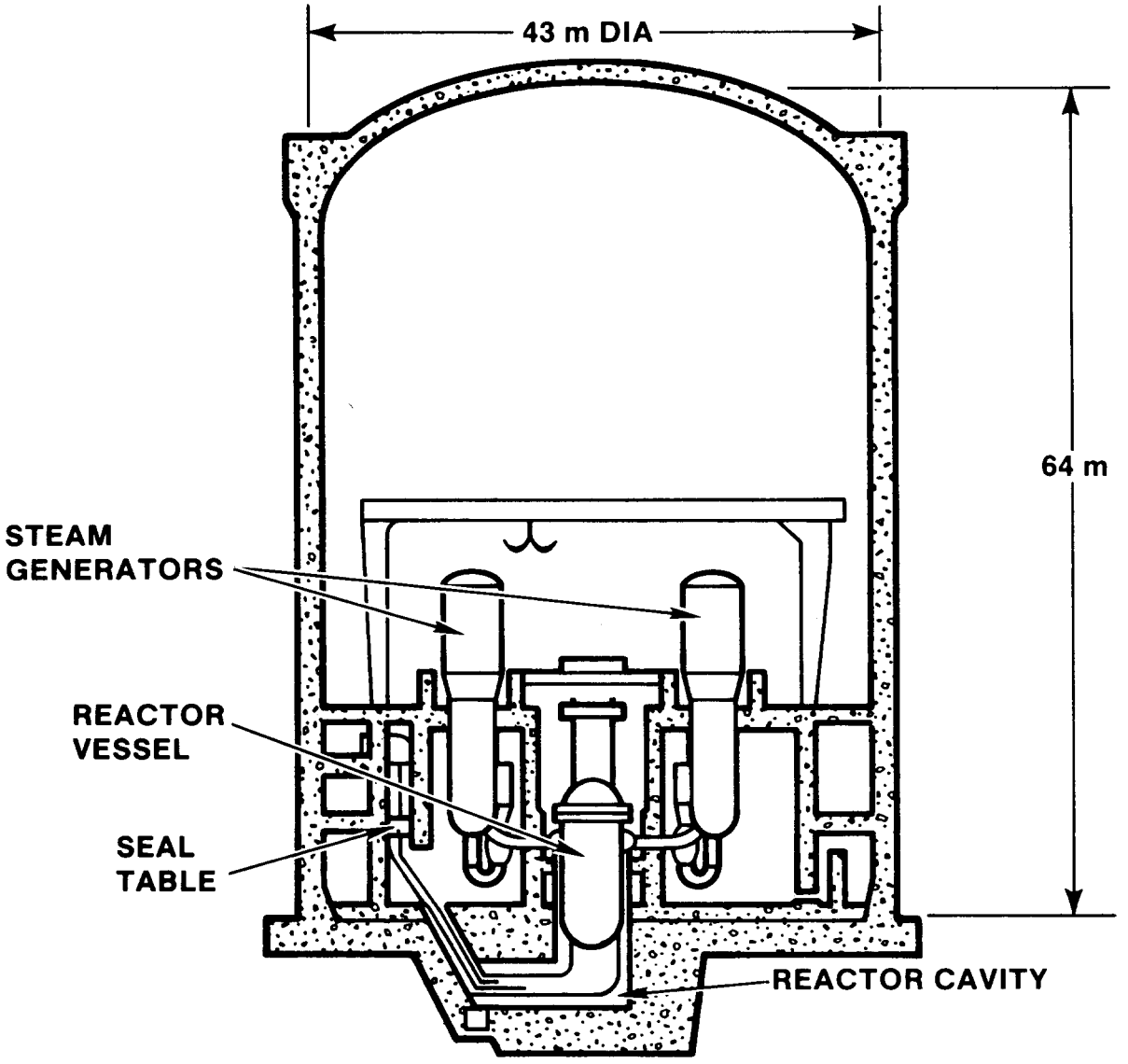

Figure 1.1: Containment Building of the Zion Reactor Plant

While agreeing that blowdown gases can sweep most of the core melt from some reactor cavities, some researchers (Squarer, 1984; Fauske, 1985) argue that obstructions outside the cavity will mitigate the direct heating problem by trapping a significant portion of the melt before it can interact with the containment atmosphere. Figure 1.1 depicts the containment building of the Zion reactor plant illustrating the compartmentalization of the building and a few of the structures and obstacles that could trap debris and thus potentially mitigate the DCH problem.

The angle of inclination of the instrument tube shaft will cause the gas and debris exiting the cavity to be directed into an enclosure beneath the seal table. It has been suggested (Squarer, 1984; Fauske, 1985) that this enclosure will trap the bulk of debris exiting the cavity. The HIPS-7C test, which is described in this report, used a 1:10 linearly scaled concrete model of the reactor cavity and structure beneath the seal table to determine how much debris is trapped by the enclosure. Debris that exits the cavity through the instrument tube shaft and escapes the intervening structure enters an annular room that is bounded by the operating floor, crane wall, and refueling canal wall. This annular room houses the steam generators, coolant pumps, pressurizer, and a large amount of piping associated with these devices. Critics of DCH have argued that debris will freeze on these structures thus depleting the quantity of debris mass that can interact with the atmosphere. The HIPS-3J test, which is described in this report, was the first attempt at understanding how debris interacts with the concrete slabs and steel pipes that are expected to intercept debris.

In many reactor plants, there is an annular gap around the RPV that could allow debris to be transported directly into the refueling canal which in turn is open to the upper dome of the containment building. Debris exiting the cavity by this route will completely bypass structures in the lower part of the containment that might potentially trap debris. The HIPS-8C test, which is described in this report, investigated the potential for debris to escape the cavity via this annular gap. The experiment used the same 1:10 linearly scaled model of the Zion cavity from previous tests except that a simulated annular gap was placed at the scaled height of the RPV.

The experiments discussed in this report are not intended to directly simulate all aspects of HPME accidents. It becomes nearly impossible to scale integral tests that simultaneously simulate complicated processes involving a broad spectrum of rate-dependent processes. The experiments are intended to provide insight into relevant physical processes and to support development of models for specific phenomena relevant to HPME and

DCH. Realistic assessment of plant performance during severe accidents can only be made by integrating phenomenological models into system leel codes (e.g., MELPROG and CONTAIN), which couple all the relevant phenomena associated with a severe accident.

2 . THE HIPS-3J EXPERIMENT

The primary objective of HIPS-3J was to determine the potential for simple structures, such as walls and pipes, to trap and retain debris that would be dispersed from the reactor cavity. To achieve this objective, an 80 kg mass of molten iron and alumina was created and forcibly expelled from a pressurized melt generator. The melt stream was directed at a canted slab of concrete that redirected the melt at a steel pipe.

A secondary objective of the test was to obtain direct and indirect measurements of the transient diameter of the discharge aperture in the melt generator. The oriface size determines the rate at which melt and blowdown gases are discharged into the cavity.

2.1 Apparatus

The apparatus for this experiment consisted of a melt generator, a concrete slab, and a steel pipe. The orientations of the components are shown in Figure 2.1.

The melt generator (Figure 2.2) was intended to produce and deliver a mixture of molten iron and alumina which was produced by the metalothermic reaction:

$$8\ Al + 3\ Fe_3O_4 \rightarrow 9Fe + 4\ Al_2O_3.$$

The melt generator consists of a crucible, a pressure vessel, and a fusible melt plug. The aluminum and iron oxide powders were ignited in the crucible where the reaction progresses from top to bottom. The entire crucible was placed inside a second vessel that is pressurized prior to ignition of the reaction. Pressure-driven ejection of melt was initiated when a fusible plug, which mounted in the lower flange over of the pressure vessel, melts after the reaction progresses to the bottom of the crucible. Additional details of the melt generator are reported elsewhere (Tarbell et al., 1986).

The concrete slab was centered approximately 0.56 m (22 in) below the melt generator and was canted 45° from the horizontal to redirect the melt towards the steel pipe. The slab was a square, 0.46 m (18 in) on a side and 0.10 m (4 in) thick, made from limestone common sand concrete. The slab was intended to represent one of the many concrete walls that exist in reactor containments.

The steel pipe was placed approximately 1 m (36 in) from the concrete slab in the anticipated path of the redirected melt. The pipe was 0.10 m (4 in) in diameter, 0.46 m long, and had a wall thickness of 6 mm. The pipe represented the many steel structures (pipes, steam generators, gratings, etc.) located outside the reactor cavity of most plants.

In the HIPS-2C test (Tarbell et al., 1986), the diameter of the orifice in the lower flange cover increased by nearly a

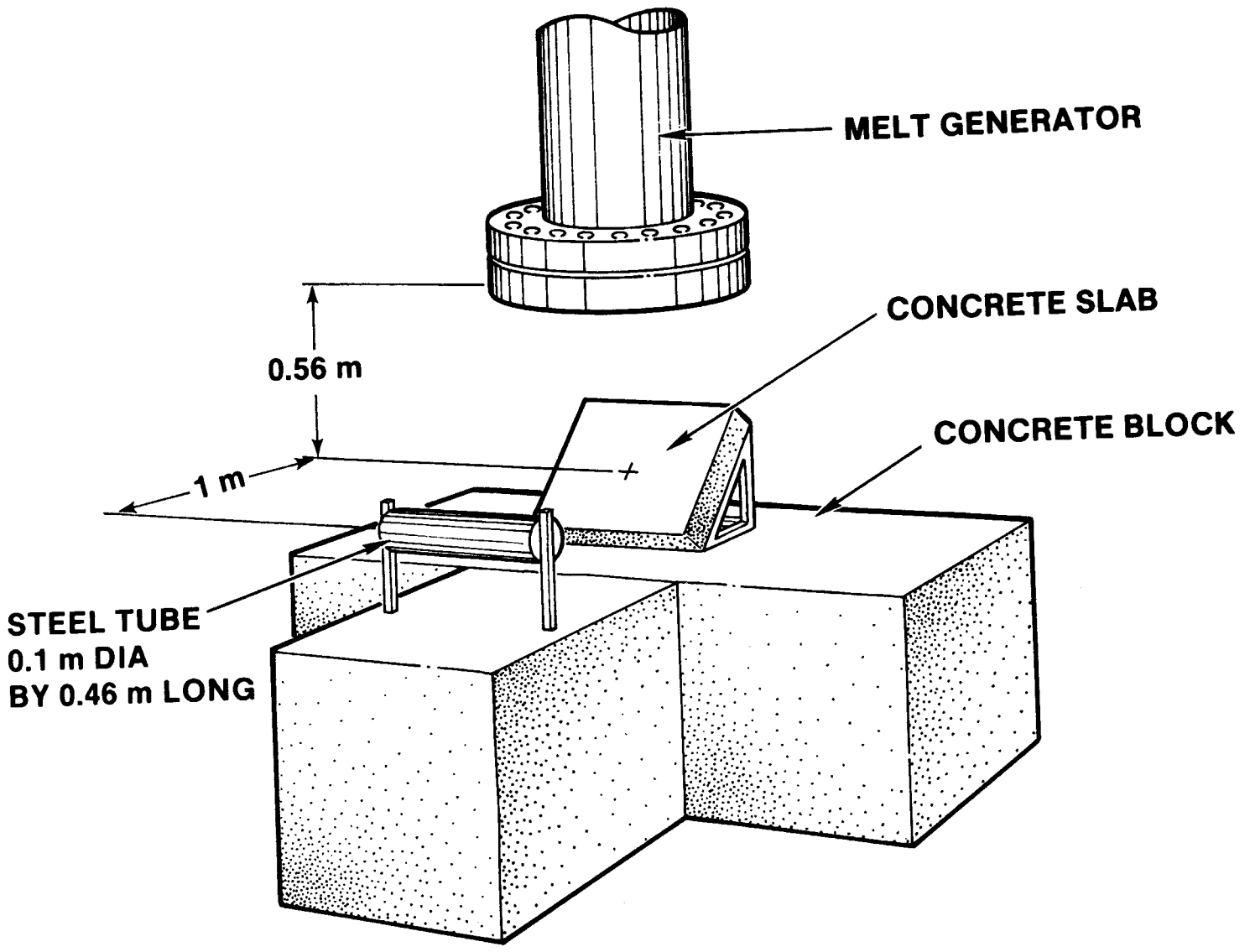

Figure 2.1: HIPS-3J Test Configuration

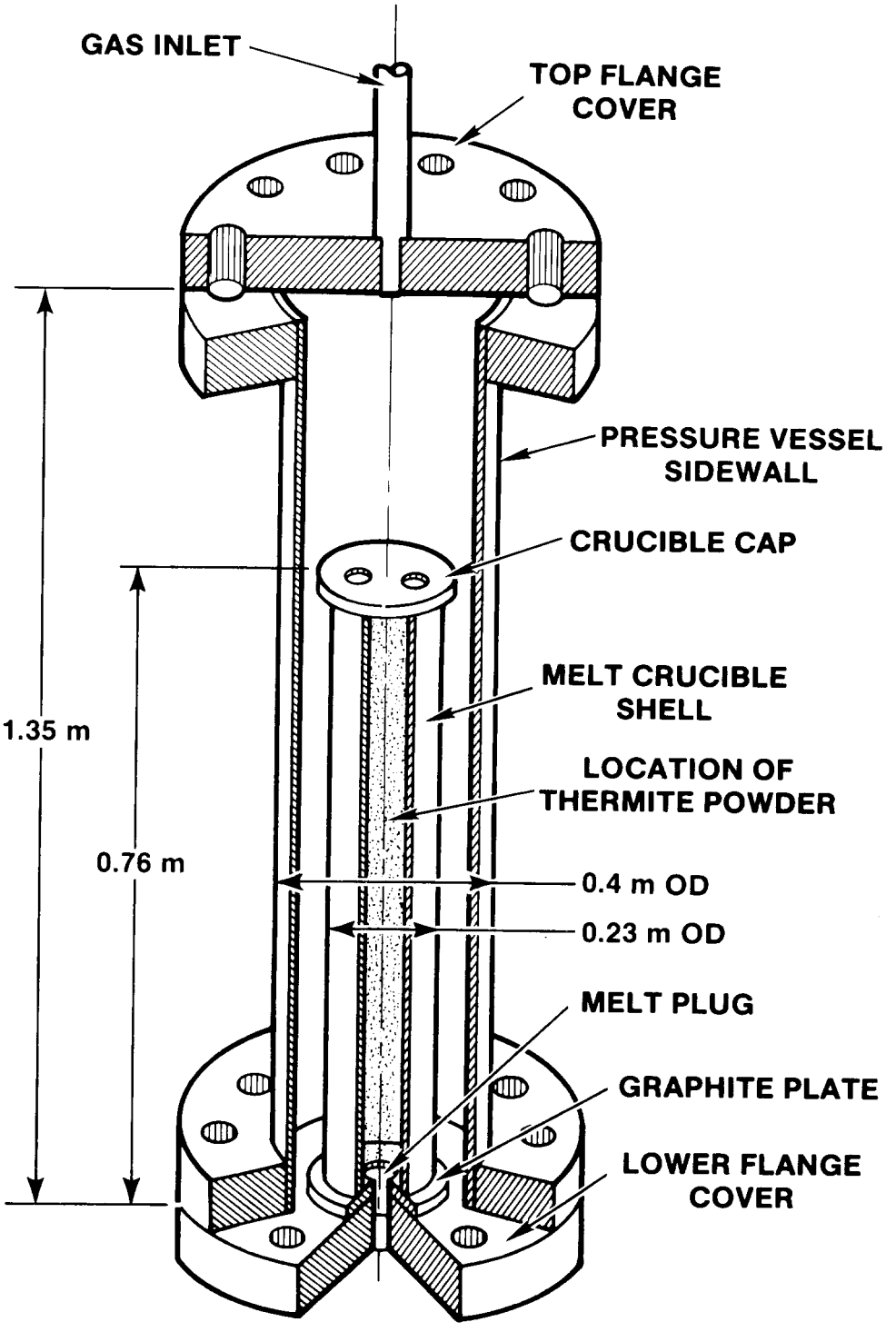

Figure 2.2: Schematic of HIPS Melt Generator

factor of three due to ablation during discharge of melt from the generator. In HIPS-3J, photodetectors were placed at various radial positions in the flange cover in an attempt to measure the rate of hole ablation. It was anticipated that the detectors would record a sharp increasing in light intensity as the ablation process uncovered the end of the detector.

Four pairs of phototransistors (Motorola type MRD310) were embedded in the flange cover, as depicted in Figure 2.3. Each pair was located at increasing radial positions of 0.0222 m (7/8 in), 0.0254 m (1 in), 0.0381 m (1.5 in), and 0.0444 m (1.75 in) respectively. The detectors of each pair were placed 90° apart in order to provide data on the symmetry of the ablation process.

The photo detectors were placed in the end of slots, 13 mm (1/2 in) deep, cut in the bottom surface of the flange cover from the outside edge. The slots were angled radially so as not to interfere with other detectors located along the same radial line. The photo detectors were held in place with high alumina cement; so that as the hole ablated, the detector would be uncovered and exposed to the luminous melt stream.

2.2 Instrumentation

A summary of the HIPS-3J instrumentation is given in Table 2.1. Pressure gauges were placed in the top flange cover of the melt generator to obtain the pressurization and blowdown histories. The primary device was a water-cooled gauge (Precise Sensors Model 111-2) placed in a machined recess filled with steel turnings to protect the sensing element. Another gauge (Kulite Model XT-190) was located in a less hostile position in the gas line near the melt generator. The second device provided a backup in the event that the primary device was affected by the heat flux from the molten pool formed during the thermite reaction.

Two thermocouples were inserted through the flange cover to a depth of approximately 0.30 m to monitor the temperature of the gas above the melt. One sensor had a 3.2-mm diameter stainless steel sheath while the other was a 1.7-mm diameter sheath unit inserted into a 6-mm diameter stainless steel tube. Small diameter holes (0.5-mm diameter) drilled in the steel tube allowed the hot gases to reach the sensor while protecting against possible contact with debris.

Three pyrometers were used to provide temperature data on the melt as it emerged from the melt generator. The first pyrometer was a single-wavelength device using a photodetector for the sensing element (Thermogage Inc.-Serial Number 2589). The response of this unit was on the order of 1 μs, which is significantly shorter than 100 ms exposure the unit had to melt. The device was incorporated into the test to determine if rapid

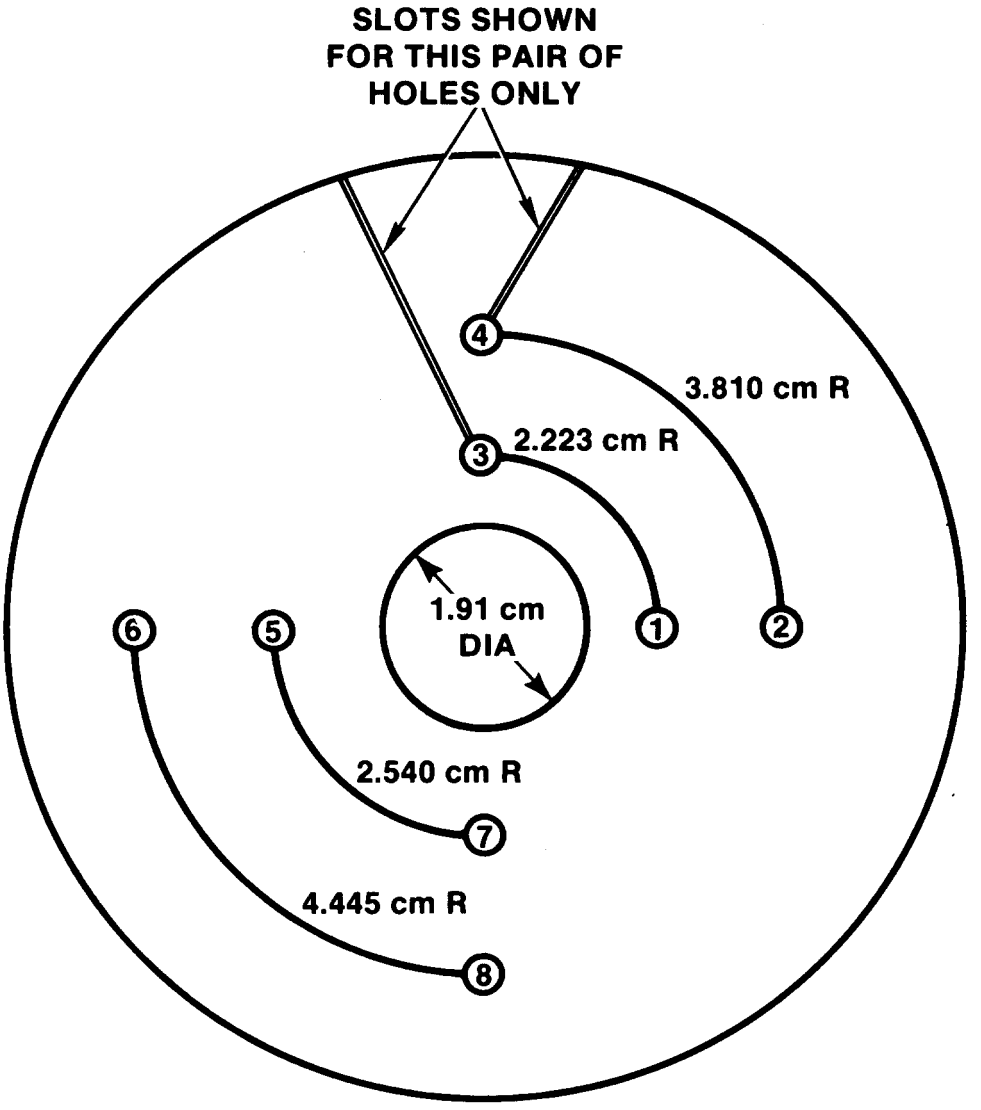

Figure 2.3: Photo Detector Locations in the Lower Flange

Table 2.1

Summary of HIPS-3J Instrumentation

Device Type	No.	Range	Location	Purpose
Pressure	1	0-34.5 MPa	Gas Line	Reference
Pressure	1	0-41.4 MPa	Melt Generator	Blowdown
TC	2	0-1500RC	Melt Generator	Expansion Chamber
Photo Detectors	8		Flange Cover	Transient Hole Diameter
Pyrometer	1	1700-4000RC	Jet	Melt Temperature
Pyrometer	1	1500-3500RC	Jet	Melt Temperature
Pyrometer	1	1500-3000RC	Jet	Melt Temperature
Force Cell	1	-8900-8900 NT	Concrete Slab	Reaction Force
Cameras	7	30-2000 fps	--	Observation
Flash X-Ray	4		Structures	Structure Interactions

variations in the debris temperature occurred during discharge of the melt. Because the emissivity of the molten material is uncertain, the temperature data from this device are somewhat uncertain in magnitude. The pyrometer was focused on the jet 2.5 cm below the melt generator. The circular target area at the jet was approximately 1.2 cm. The second device was also a single-wavelength device (Ircon Model 22B30) incorporating optics to allow placement several meters from the target. The useful range of this instrument was 1500°-3000°C with a response time constant of 30 ms. For this experiment, the device was placed approximately 5 m from the melt generator. At this distance, the spot size of the image was 1.7 cm in diameter.

The other pyrometer (Incon Model R-35C10) was a two-color unit. For this unit, the target material was assumed to behave as a gray body, so that the ratio of transmitted energies at the two different wave-length yields temperature directly without need for emissivity corrections. This feature also reduces the influence of intervening, semitransparent materials, such as aerosols, known to accompany melt discharge.

The two-color pyrometer has a useful range of 1500°-3500°C and a time constant of 10 ms. This time constant is significantly greater than that of one-color pyrometer but still an order of magnitude less than the expected melt discharge time. The pyrometer was focused on the jet 0.5 m below the melt generator, and the circular target area at the jet was approximately 2.5 cm.

The reaction force on the concrete slab resulting from the impinging jet was measured by mounting a single force cell on the frame supporting the slab as depicted in Figure 2.4. The device (Kulite Model TC-2000) uses semiconductor strain gauges to form a balanced 4-arm bridge circuit and a rated capacity of 2000 lb in both tension and compression. The support frame was constructed so that the front edge pivoted about a pin while the back was attached to the gauge. Both the pivot and the load cell were placed on a steel plate laid on the massive concrete block. In this manner, forces exerted on the center of the concrete surface were carried equally by the pivot and the gauge.

Six high-speed photographic film cameras and one video camera were employed to record the test; Table 2.2 summarizes the camera coverage for this test. The 2000 fps cameras (HyCam manufactured by Redlake Corp.) were triggered by a shielded photo detector embedded in the thermite powder near the bottom of the melt crucible. These cameras provided closeup coverage of the melt/structure interactions. The remaining cameras provided overall coverage of the test. These latter cameras were triggered by the signal that initiated ignition of the thermite burn with each camera delayed a predetermined length of time. The entire test was recorded in real time with a video camera.

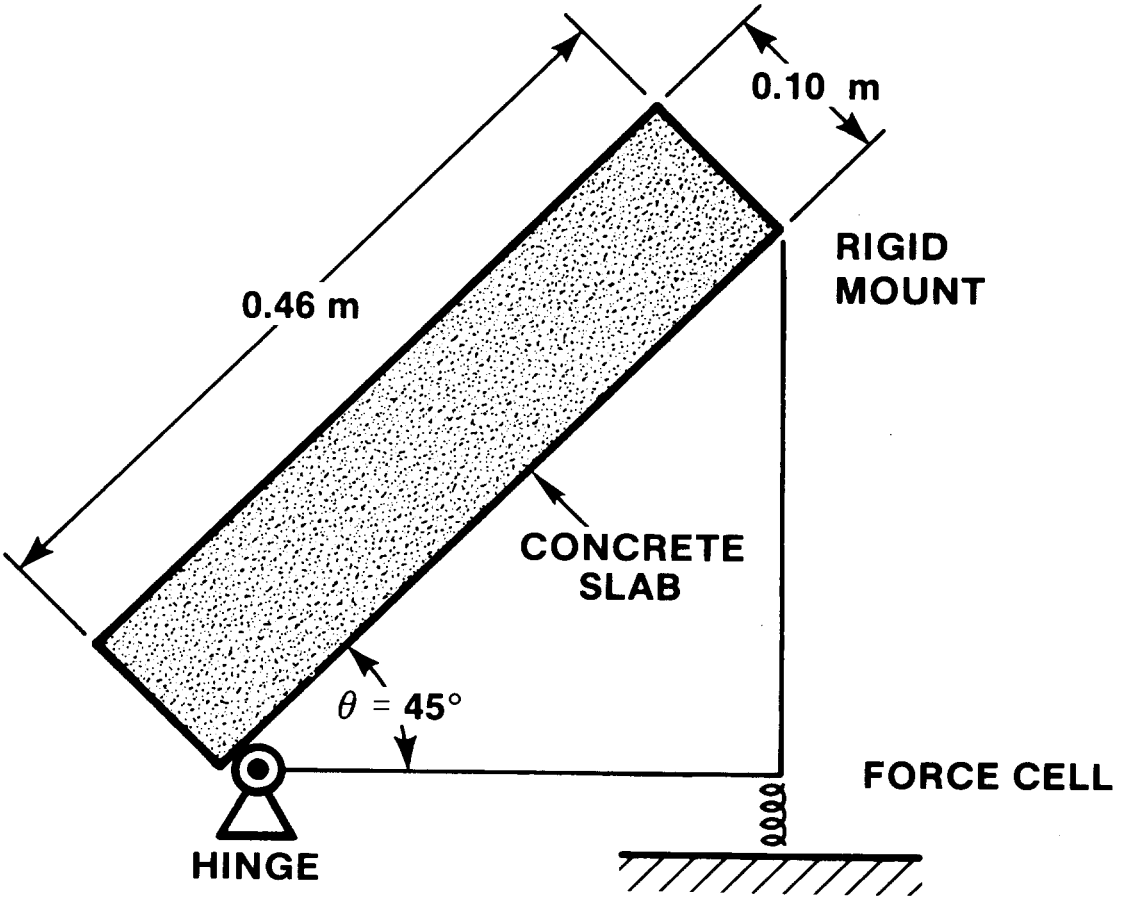

Figure 2.4: Force Cell Location

Table 2.2

Summary of HIPS-3J Camera Coverage

Device	Start Time(a) (s)	Speed (fps)	Field of View
Camera	Trigger	2000	10' - Melt Generator to Concrete Slab
Camera	Trigger	2000	10' - Concrete Slab to Steel Pipe
Camera	-5	100	50' - Overall
Camera	+5	200	200' - Long Range Overall
Camera	+18	1000	20' - Close Overall
Camera	+32	1000	20' - Close Overall
Video	-	30	200' - Long Range Overall

[a] Relative to Ignition of Thermite Powder

Previous experiments have shown that an intense cloud of aerosols is produced during melt discharge from the melt generator. It seemed likely that these aerosols would obscure the nature of melt/structure interactions, thus reducing the value of photographic film as a diagnostic tool. Under these conditions, radiographs are useful because they are not hindered by aerosols or blinded by radiated light from the melt stream. The flash X-ray (Hewlett Packard Model KC-150, 150 keV) technique should be particularly useful because the inherent short exposure times (70 ns) essentially freezes the motion of even the fastest particles.

Figure 2.5 shows the position of the four X-ray film cassettes in relation to the apparatus. The X-ray generators and film cassettes were positioned to give a view parallel to the pipe and orthogonal to the direction of flowing debris. The first cassette looks at the melt stream as it emerges from the melt generator, while the second cassette looks at the point where the melt stream strikes the concrete slab. The third and fourth cassettes look at melt/pipe interactions at the front and rear of the steel pipe respectively.

The aluminum cassettes and X-ray generators were insulated with a refractory blanket to protect them from the splatter of hot melt. The X-ray units (located 4 m from the cassettes) were triggered as sequenced by photo detectors placed at the exit of the melt generator, the surface of the concrete slab, and the pipe surface. It was estimated that the resolution of the X-ray system was no better than 0.3 mm due to the combined effects of film and geometric unsharpness.

2.3 Initial Conditions

The initial conditions for HIPS-3J are summarized in Table 2.3. The gas volume, pressure, and temperature are all values at the onset of melt ejection.

2.4 Experiment Results and Analysis

This section presents the results obtained from the HIPS-3J experiment. Analysis of the test is also presented where appropriate to aid in the understanding and interpretation of the experiment observations.

2.4.1 Camera Coverage

Figure 2.6 summarizes the sequence of events as recorded by the cameras. X-ray coverage of this test, which was focused on melt/structure interactions, failed to provide useful information because a faulty trigger signal caused all X-ray heads to improperly synchronize with melt ejection.

Prior to impact with the slab, the jet appears as a luminous cone. Flash X-rays of similar jets from other tests (Brockmann &

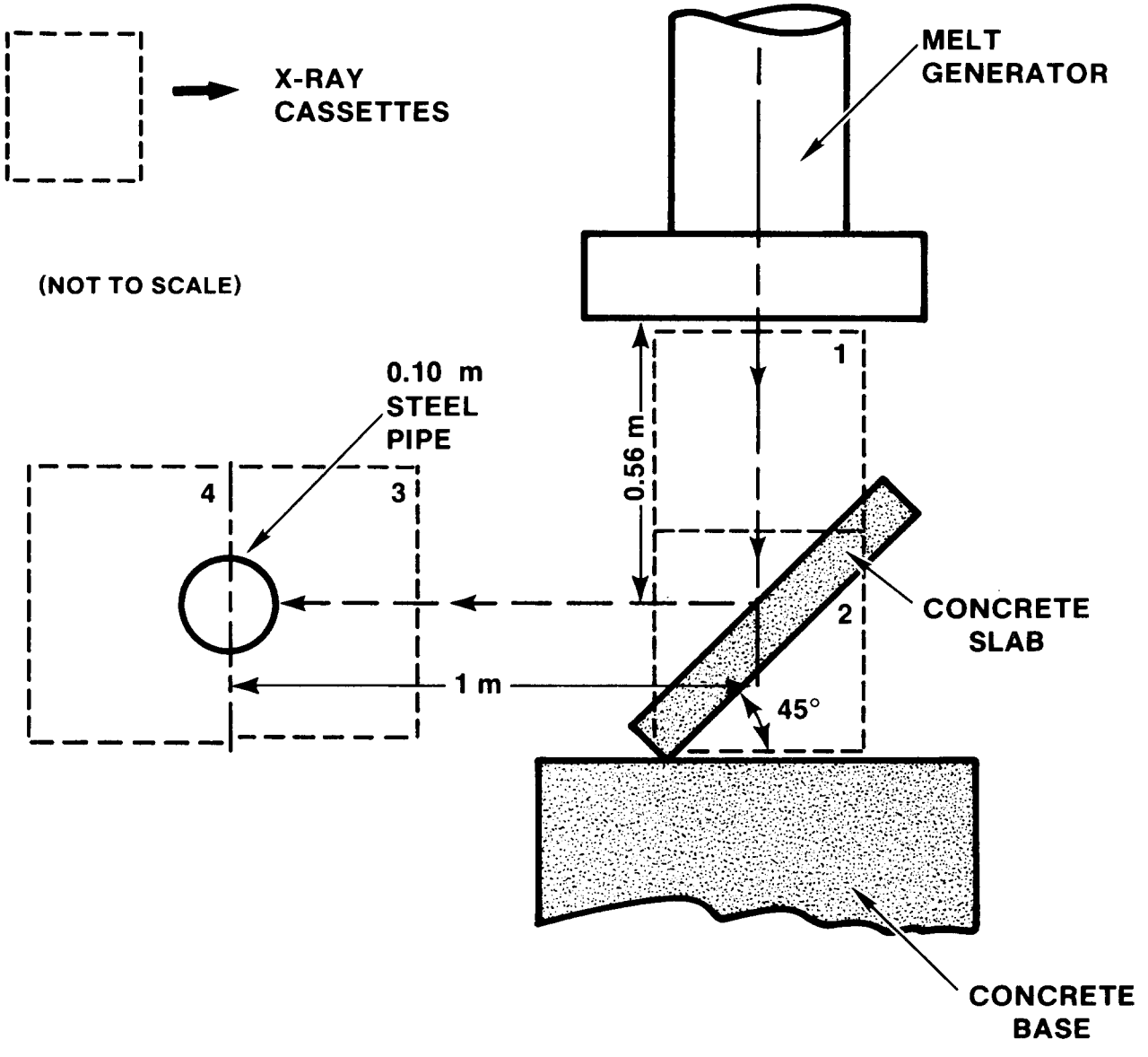

Figure 2.5: X-Ray Cassette Locations

Table 2.3

HIPS-3J Initial Conditions

Melt Mass	80 kg	
Thermite Composition	Iron Oxide (Fe_3O_4)	61.04 kg
	Aluminum (Al)	18.96 kg
Melt Compositions	Iron (Fe) + Alumina (Al_2O_3)	
Dopants	None	
Gas	Carbon Dioxide (CO_2)	
Gas Volume	0.118 m^3	
Initial Pressure	4.18 MPa	
Ambient Temperature	423 K	
Orifice Diameter	0.0191 m	

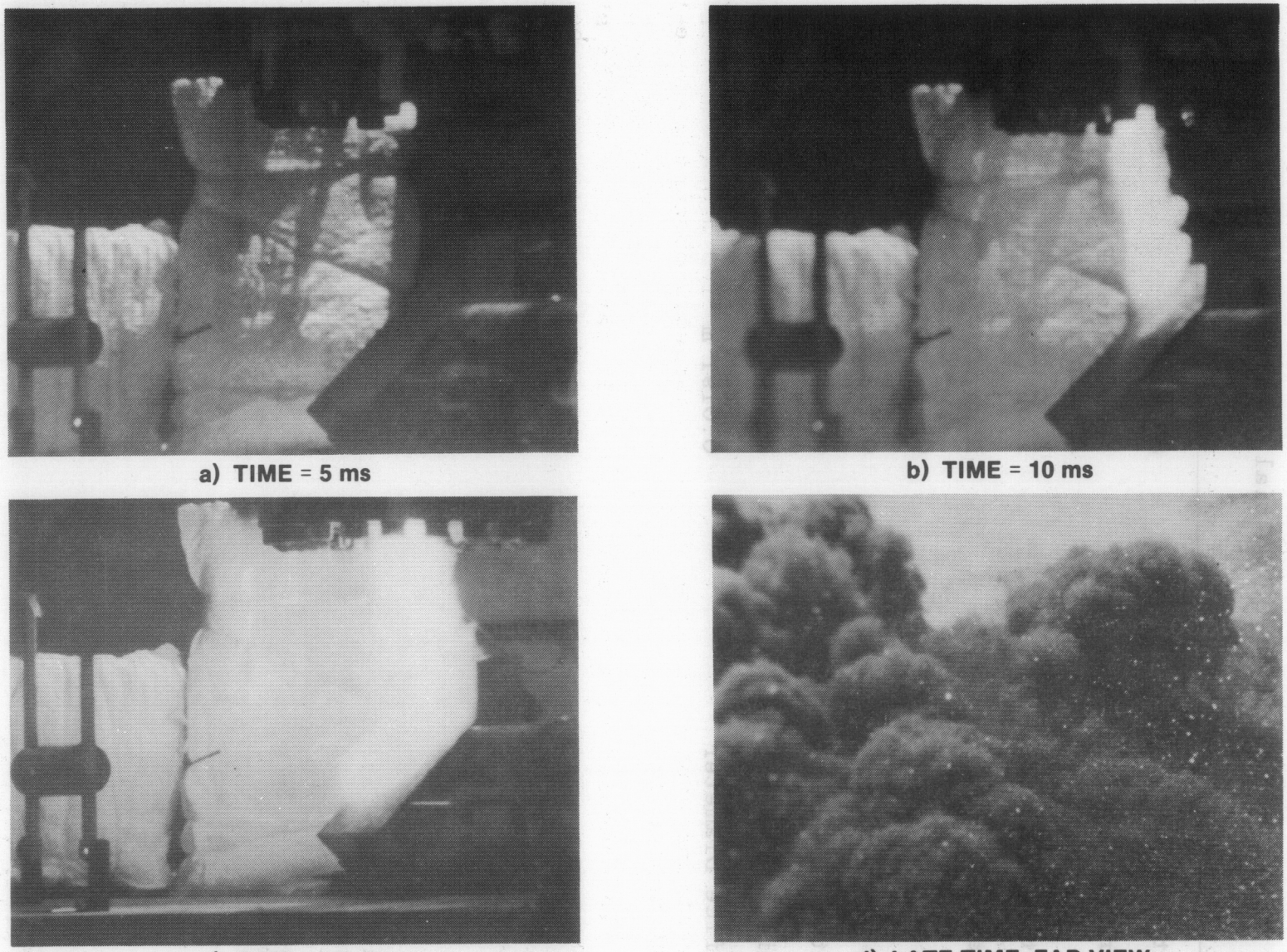

Figure 2.6: Camera Coverage

Tarbell, 1984) where CO_2 was the pressurizing gas indicated that there is a coherent core of melt surrounded by luminous gas and aerosol. As Figure 2.6 indicates, the jet appears to travel about 75% of the distance to the slab in two frames of the film record (10 ms), thus indicating that the initial jet velocity was approximately 42 m/s. This visual estimate of the jet velocity exceeded the predicted value of 28 m/s, assuming liquid discharge and an orifice coefficient of 0.6. The predicted value, as will be discussed later, is consistent with the measured depressurization history of the melt generator during melt discharge. The visual estimate is more closely comparable to the maximum possible liquid discharge velocity of 46.6 m/s, which occurs for a discharge coefficient of unity. It should be noted, however, that the visual estimate of the initial jet velocity suffers from a lack of resolution in the space and time measurements. The predicted values of the jet velocity, which are consistent with other data over the entire duration of melt discharge, are thought to be a more accurate measure of the quasi-steady jet velocity.

Upon impact with the slab, vigorous splashing was observed with the bulk of the material being deflected at a shallow angle relative to the slab. Only a negligible amount of melt was retained on the surface of the concrete slab. Far field photos taken late in the sequence show melt particles propagating in all directions with an intense cloud of aerosols obscuring the entire test apparatus.

Interaction of the redirected melt particles with the steel pipe was completely obscured by the aerosol cloud, which begins to form shortly after the jet struck the slab. Only a small quantity of melt was retained by the pipe in the form of a thin crust on the forward surface of the pipe.

Aerosol instrumentation was not employed on this test so that the quantity and size distribution of the aerosols were not determined. However, the mechanisms of aerosol production, which were identified by Brockmann & Tarbell (1984) for other tests, are believed to be operable in the HIPS-3J test also. Of those mechanisms identified, vaporization (not boiling) from the highly fragmented melt (after splashing) followed by subsequent condensation of the vapors in the cool atmosphere is thought to be the dominant source of the aerosols.

2.4.2 Pressurization and Blowdown History of the Melt Generator

Figure 2.7 summarizes the pressure history of the melt generator. The start of melt discharge is taken as the reference time. Gradual charging of the melt generator with CO_2 gas began at -175 s. Prior to ignition of the thermite at -15 s, the melt generator was isolated from the gas source. The thermite reaction time was 15 s.

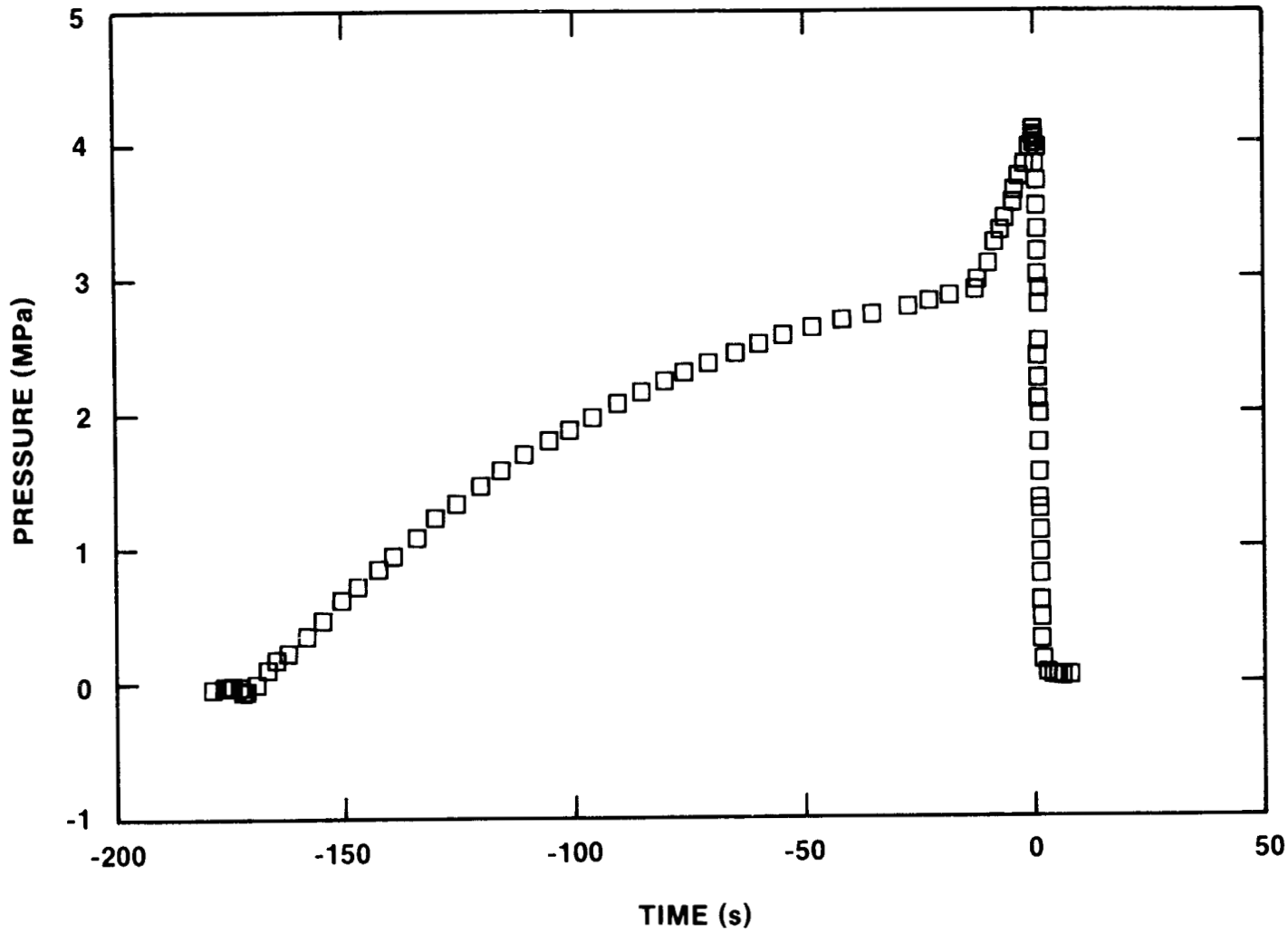

Figure 2.7: Pressurization History of the Melt Generator

Both the temperature and pressure were observed to increase during the thermite reaction. The pressure increase occurred partly because contaminants in the charge powders produced gas during the burn, so it was useful to estimate the magnitude of the effect. By applying the ideal gas law to the gas before and after the burn (subscripts 0 and 1, respectively), the relative change in the gas mass and composition is given by:

$$\frac{\Delta(mR)}{mR} = \frac{T_0}{T_1}\frac{P_1}{P_0}\frac{V_0}{V_1} - 1 \quad .$$

Here m, R, T, P, and V are the mass, gas constant, temperature, pressure, and free volume of the cover gas.

Composition and density changes of the thermite reaction alters slightly the free volume in the melt generator. The ratio V_1/V_0 is estimated to be 0.91. The measured ratios of pressure (P_1/P_0) and temperature (T_1/T_0) of the gas are about 1.36 and 1.42, respectively. Using these values,

$$\frac{\Delta mR}{mR} = .052 \quad ,$$

indicating that contaminant gases contributed only slightly to the pressurizing gas.

Figure 2.8 shows an expanded version of the depressurization history of the melt generator following the onset of melt ejection. Two phases can be distinguished; the first phase, lasting about 475 ms, corresponds to liquid phase discharge during which the pressure decreases because the free volume increases as melt is expelled from the generator. The onset of gas flow out the orifice marked the beginning of the second phase. Gas discharge is accompanied by continued, but reduced, discharge of melt (Pilch & Tarbell, 1985). The second phase lasts 1.5 - 2 s at which time the blowdown of the generator is complete.

Figure 2.8 also shows a model prediction (Pilch & Tarbell, 1985) for the blowdown history. During the first phase, the model couples melt discharge (sharp-edged orifice discharge coefficient of 0.6) with a transient orifice diameter that is calculated to increase in size due to ablation. The excellent agreement between experiment data and model predictions lends confidence in the model's ability to predict ablation rates and time dependent hole sizes prior to the onset of gas blowdown.

Figure 2.9 shows the time-dependent orifice diameter as predicted by the model of Pilch & Tarbell (1985). During the first phase, the ablation rate (based on diameter) is constant and equal to 9.25 cm/s. The predicted ablation rate rapidly approaches zero when gas discharge begins. The final orifice size is predicted to be 6.5 cm, which is in excellent agreement

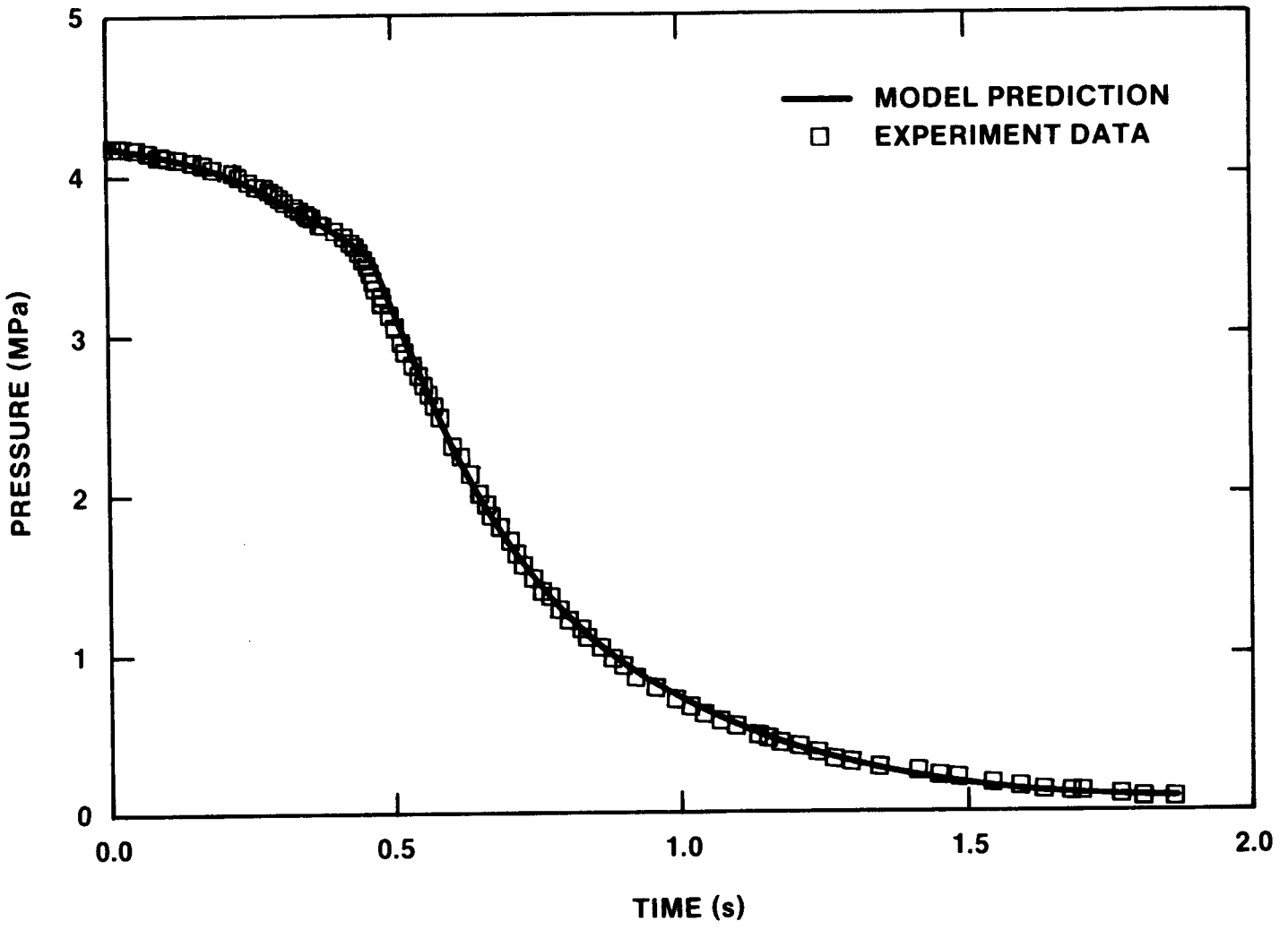

Figure 2.8: Pressure History of the Melt Generator During Melt Ejection and Blowdown

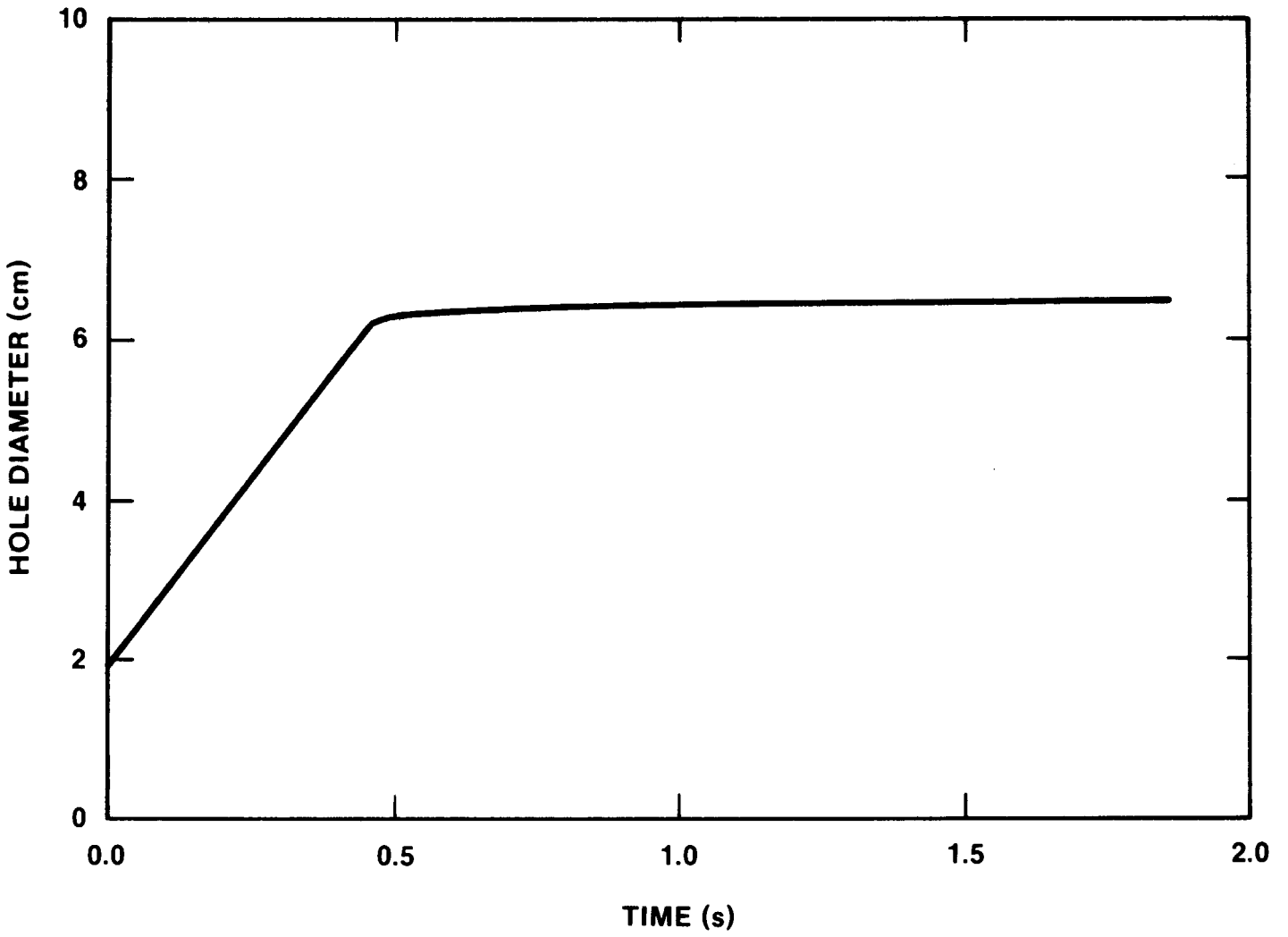

Figure 2.9: Predicted Ablation of the Discharge Orifice

with the posttest observation of 6-7 cm. Figure 2.10 compares an unused discharge orifice with the one removed from the HIPS-3J apparatus to show that the erosion pattern is not exactly symmetric. Notice that the upstream side of the discharge orifice has taken on a bellmouth shape.

In the above discussion, the ablation rate and transient hole diameter were obtained from model predictions that were validated by pressure measurements during the blowdown process. Phototransistors were imbedded in the lower flange at varying distances from the orifice surface in anticipation of directly measuring the transient hole size. Unfortunately, this technique did not provide useful data on hole ablation because of unexplained signal noise.

Figure 2.3 shows the locations of the detectors in the lower flange, and Table 2.4 summarizes the experiment data. Eight combinations of sensors or sensors and initial orifice size were available. Those pairs involving the initial orifice size must be discarded because there was a failure to synchronize the detector signal with the onset of melt discharge. Four detectors signaled melt at their locations when the thermite was ignited, which occurred about 15 s prior to melt discharge. Thus, signal noise dictated that the 3;4, 5;6, and 7;8 pairs also be discarded. Only the 1;2 pair of detectors had complete timing information, and this pair suggested that the ablation rate (based on diameter) is 1058 cm/s. This is two orders of magnitude greater than model predictions, implying a final hole diameter of 503 cm if the ablation rate were constant over the discharge interval. This clearly was not observed.

Based on the slope of the melt generator pressure record, gas blowthrough (Pilch & Tarbell, 1985) occurs at approximately 475 ms after melt discharge was initiated. Following gas blowthrough, there is a simultaneous discharge of melt and gas with pneumatic atomization of the melt occurring in the orifice. Model predictions (Pilch & Tarbell, 1985) for this second phase are compared with experiment data on Figure 2.8. The model assumes that the gas in the melt generator expands isentropically during blowdown. The model assumes that choked, adiabatic, and separated flow occurs in the orifice. The figure shows excellent agreement between model predictions and experiment data for this second, predominantly gas discharge, phase.

As depicted in Figure 2.4, a load cell was centered along the back edge of the rack supporting the concrete slab. Because of the geometry, the load cell measured one-half the force required to deflect the jet downwards along the slab:

$$F = \frac{1}{2} (V_j \dot{m}_j + V_g \dot{m}_g)(1 - \sin^2\theta) \quad ,$$

where the velocities (V) and the mass flow rates ($\dot{m}$) of the melt and gas are taken from the model by Pilch & Tarbell (1985).

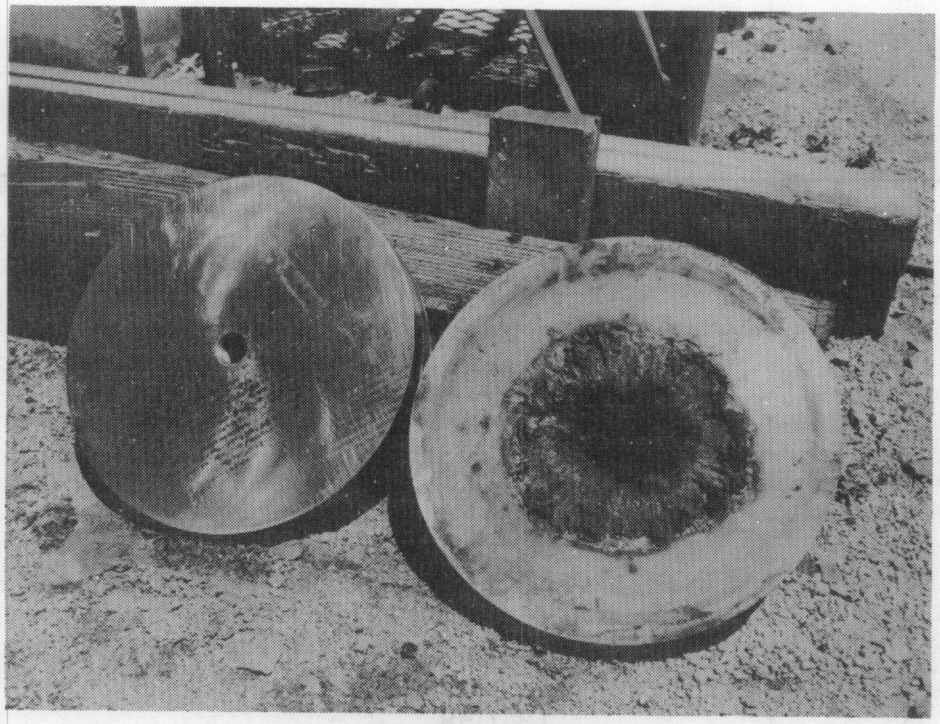

UPSTREAM SIDE

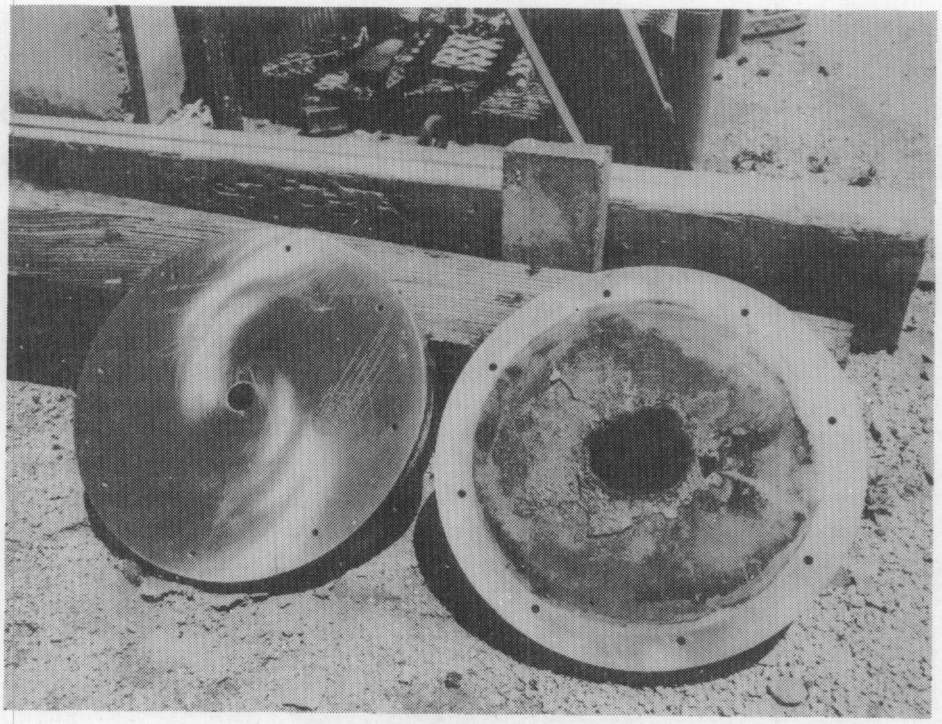

DOWNSTREAM SIDE

Figure 2.10: Upstream and Downstream Sides of the Discharge Orifice Compared to an Unused Orifice Plate

Table 2.4

Photo Detector Signal Sequence

Pair Number	Time of Signal (s)	ΔR(cm)
0	-	
1	13.058	2.223
0	-	
3	13.063	2.223
0	-	
5	13.063	2.540
0	-	
7	Ignition	2.540
1	13.058	
2	13.061	1.587
3	13.063	
4	Ignition	1.587
5	13.063	
6	Ignition	1.905
7	Ignition	
8	Ignition	1.905

As discussed previously, this model successfully predicts the melt ejection and blowdown phases of the discharge process.

Load cell measurements exceeded the predicted forces by about an order of magnitude, which is physically impossible given the initial conditions of the experiment. This suggests a sensitivity error in interpreting the data, but the source of any possible error of this type could not be identified with certainty.

Figure 2.11 compares model predictions with experiment data that are arbitrarily scaled downwards by a factor of ten. Model predictions and experiment data show that the reaction force increases during the melt ejection phase. The reaction force increases because the orifice increases in size thus allowing more melt to impinge on the slab as time increases. The reaction force is seen to drop off rapidly once gas discharge begins. This is because the low density gas does not carry the same momentum as the higher density melt despite the fact that gas velocities are much higher. The experiment data also exhibit a low frequency oscillation, with the time constant (~0.21 s) is comparable to the the time scale of melt discharge. This oscillation is much slower than the natural frequency of the slab/load-cell system, and it most likely results from oscillations of the support structure.

Three pyrometers were used to measure the temperature of the melt jet: 1 one-color pyrometer and 2 two-color pyrometers. The one-color pyrometer was placed in close proximity to the melt stream where its function was compromised shortly after it was struck by the melt. The one-color pyrometers require an emissivity value for the melt in order to quantify the temperature, and a constant value of 0.3 (Touloukian, 1967), which is appropriate for the alumina phase (by volume), was used in the calculations. The two-color pyrometers require no such correction.

Figure 2.12 compares the measured temperatures from the three pyrometers. Peak temperatures range from 2170 K to 2470 K. These temperatures are well below the theoretical value of 3200 K for a complete and adiabatic reaction, thus suggesting that the reaction was neither complete nor adiabatic. The measured temperatures are well above the freezing point (1700 K) and well below the boiling point (3200 K) of the iron phase of the melt. However, the peak temperatures straddle the freezing point (2300 K) of the alumina phase of the melt.

2.4.3 Structure Interactions

The film records reveal that splashing is a significant interaction when high velocity jets and particle streams strike simple structures. Only a small amount of material was retained by the surfaces (including the steel surface), with the retained

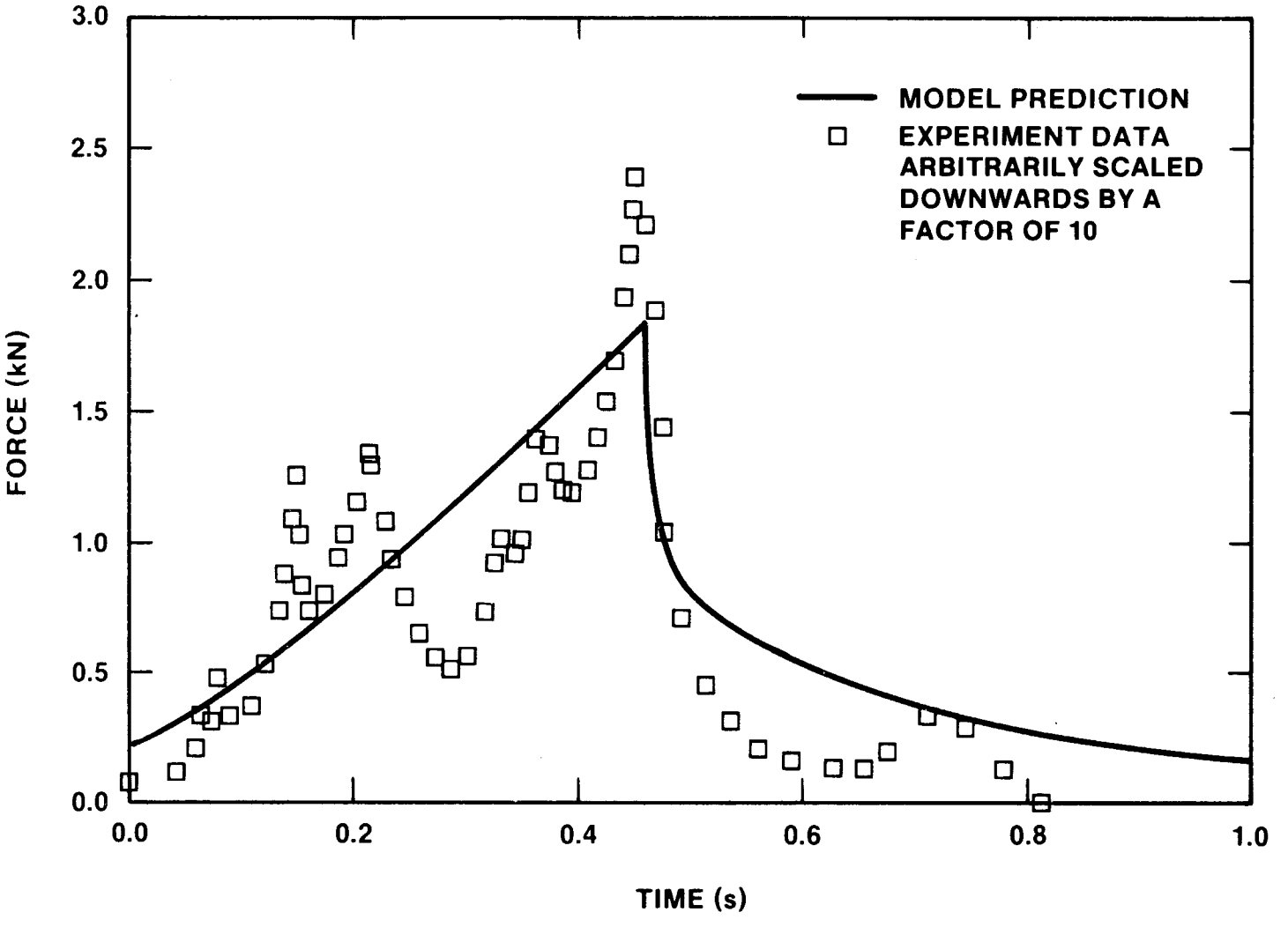

Figure 2.11: Comparison of Scaled Load Cell Measurements With Model Prediction

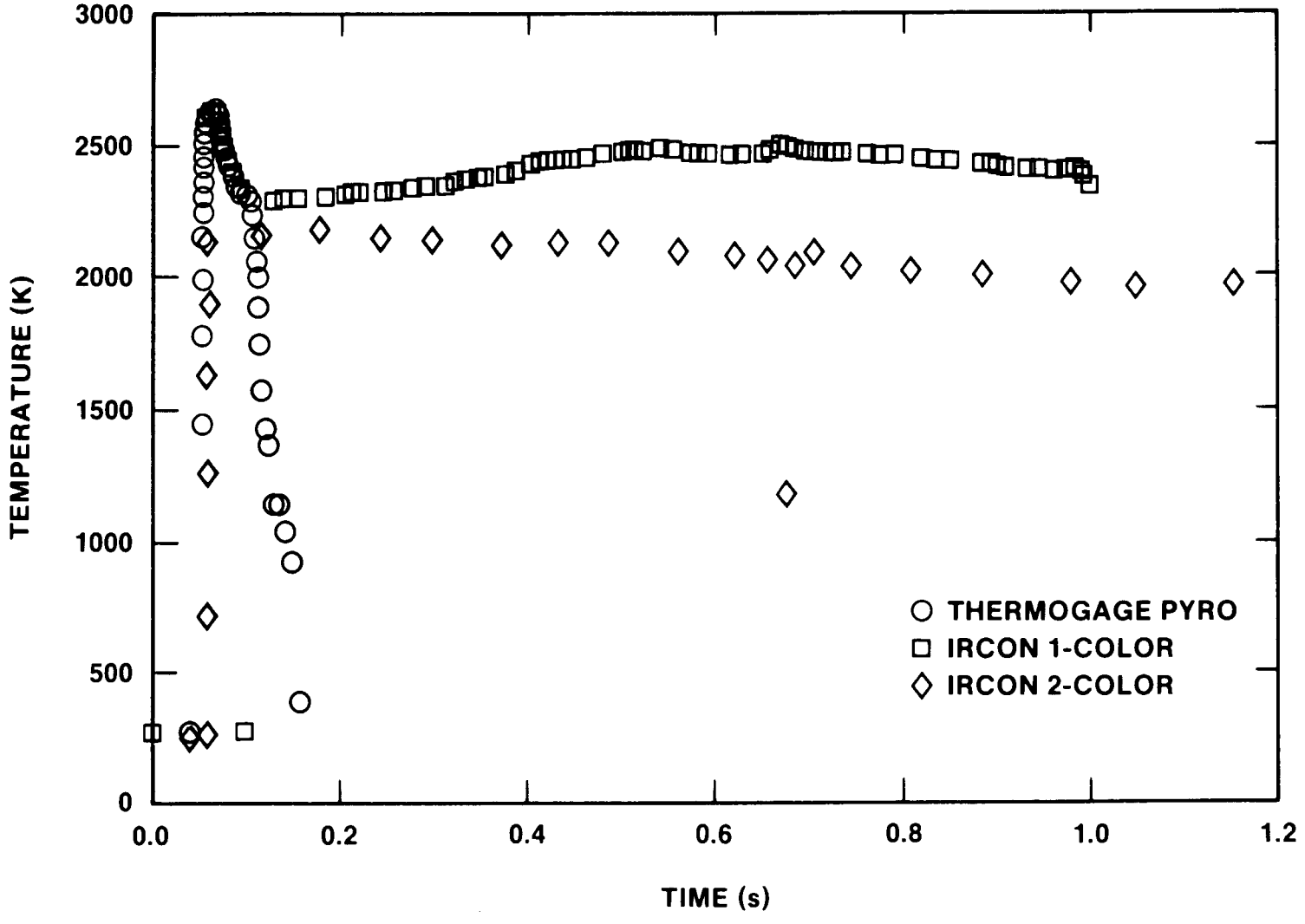

Figure 2.12: Pyrometer Measurements of Jet Exit Temperatures

material in the form of a thin crust. The impact of melt streams with structures does not guarantee that the melt will be trapped or retained by the structure.

The interaction of melt streams with structures alters the direction and character of the stream. Figure 2.6 shows that the bulk of the deflected material skids along the surface of the slab. This is consistent with observations of Tarbell et al. (1984) in the SPIT-19 experiment. The film records clearly show that the melt jet fragments when it impacts the concrete slab, thus greatly increasing the surface area of the melt stream. Thus the structure interaction may also promote mixing of the melt with the atmosphere since splashed particles are observed to propagate in many directions.

Crust formation was the only observed mechanism for retaining material on the simple structures used in this test. However, only limited and somewhat isolated crust formation was observed on the concrete slab, with the surface appearing slightly eroded (<1 cm). This observation is consistent with reported observations from other tests (Tarbell et al., 1986). It is speculated that decomposition of the concrete surface under the applied heat load prevents a stable crust from adhering to the concrete. Concrete is an ineffective material for retaining melt by crust formation.

A more uniform crust, approximately 0.5 mm thick, was observed on the forward-facing surface of the steel pipe. No crust was observed on the rear surface, which was shadowed from the debris stream. Thus, when extrapolating to reactor geometry, it must be recognized that melt can be retained as a crust only on those steel surfaces that are exposed to the melt.

The maximum quantity of material that might be retained as a crust can be estimated by assuming conduction freezing of an infinite supply of melt on an infinitely thick surface. The crust thickness (δ) after a period of time (t) is given by

$$\delta = 2\lambda\sqrt{\alpha t} \quad ,$$

where λ is a growth rate parameter for a superheated melt and is determined by a transcendental equation (Carslaw & Jaegar, 1959), and α is the thermal diffusivity of the frozen crust. The values for λ and α are 0.5 and 2.8×10^{-6}, respectively, for iron/alumina thermite on room temperature steel.

The predicted thickness of crust that could develop during the melt relocation time (0.5 - 1.0 s) is 1.1 - 1.7 mm. This predicted thickness is a factor of 2 - 3 greater than the observed crust thickness. This suggests that the freezing process was limited by the supply of melt to the surface. Indeed, Figure 2.6 shows that a large portion of the melt skids along the slab surface and is not redirected towards the pipe. An upper bound to the fraction of melt splashed into a conceptual

hemisphere above the slab can be estimated by assuming that all splashing melt is retained as a uniform crust 0.5 mm thick on the surface of the hemisphere. Approximately 30 kg, representing 37% of all the melt, would be retained in this fashion.

3. THE HIPS-7C EXPERIMENT

The objective of the HIPS-7C experiment is to determine if a specific excavity structure, such as that found in the Zion plant, would be effective in trapping melt that is dispersed from the reactor cavity. To achieve this objective, an 80 kg mass of molten iron and alumina was expelled from a pressurized melt generator into a scaled model of the Zion reactor cavity. Melt dispersed from the cavity then impacted on a scaled model of the excavity structure found in the Zion plant. The entire apparatus was placed in a large open-ended steel box in order to facilitate posttest recovery of the debris.

3.1 Apparatus

In the HIPS-7C test, 80 kg of molten iron and alumina, doped with 1.5 kg of fission product mocks, was ejected from a pressurized melt generator through an ablating orifice. The melt generator is essentially the same fixture as used in the HIPS-3J test (Figure 2.2) and other HIPS tests (Tarbell et al. 1986). The jet of melt was directed into a 1:10 linearly-scaled concrete model of the Zion reactor cavity. The cavity model is the same one used in previous tests (HIPS-2C, HIPS-5C) and details can be found in Tarbell et al. (1986).

Just outside the cavity was a 1:10 linearly scaled model of a structure which, in the Zion containment (Figure 1.1), allows instrument tubes to pass from the reactor cavity into the seal table room. The structure was made from three slabs (0.1 m thick) of limestone common-sand concrete. This structure is essentially a three-sided room with a roof and a short overhang on the open side. Details of the structure are given in Figure 3.1 The structure and cavity exit are oriented in such a way that all debris exiting the cavity will impact the structure unless it is redirected by the deflected gas stream.

The entire apparatus (melt generator, cavity, and excavity structure) was placed in a large steel chamber (45 m^3) that was open on one end. The apparatus was oriented such that the open side of the structure faced the closed back of the chamber. Details of the apparatus and the chamber are given in Figure 3.2.

3.2 Instrumentation

A summary of the HIPS-7C instrumentation is given in Table 3.1. The melt generator was instrumented with two pressure transducers and one thermocouple to determine the gas pressure and temperature, respectively. One pressure gauge (Kulite model H19S-375) was placed in a machined recess in the top flange cover. Stainless steel metal turnings in front of the gauge face protected the device from damage by melt particles. A similar gauge was mounted in a tee fitting in the gas line heading to the

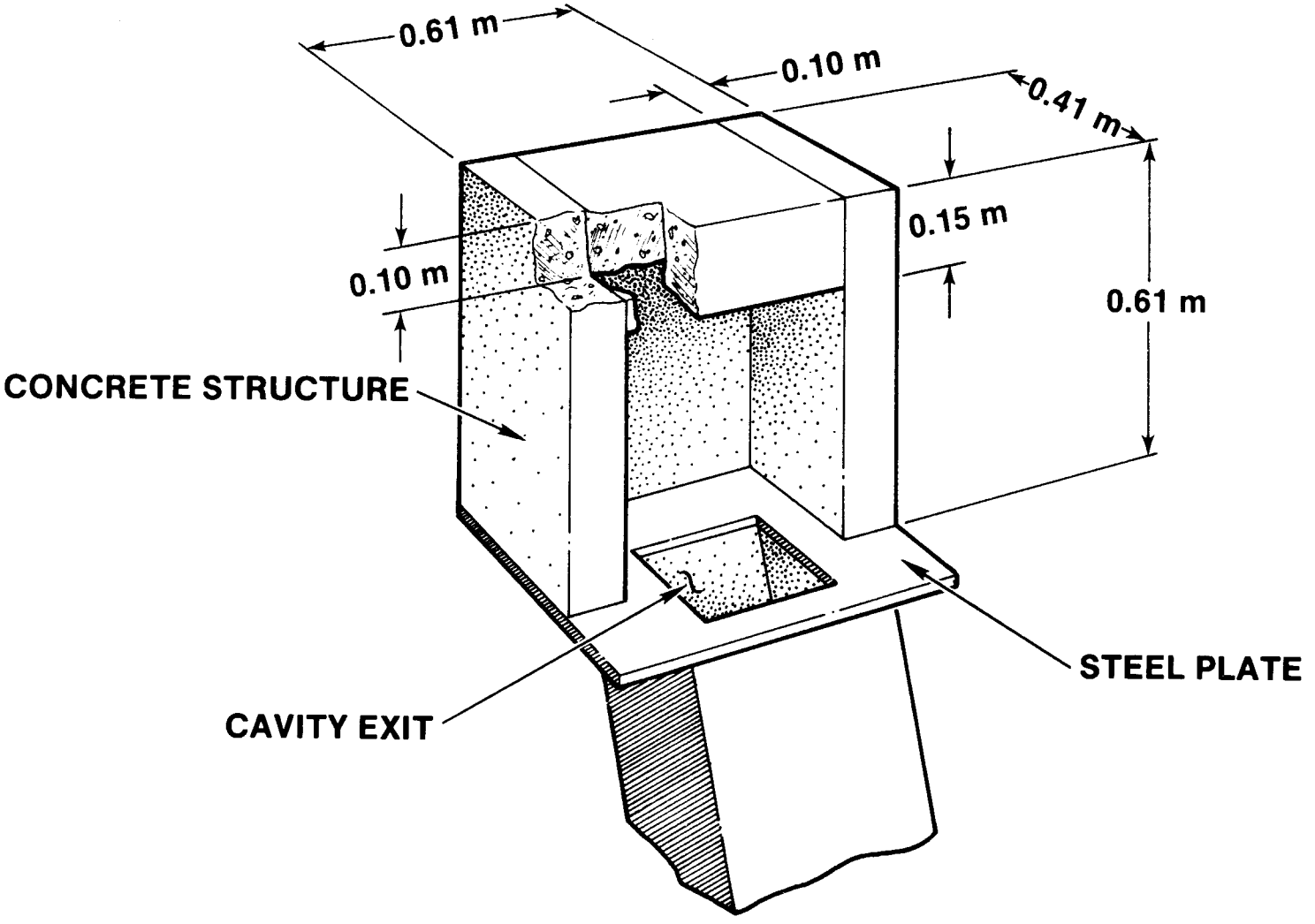

Figure 3.1: Details of the Excavity Structure For HIPS-7C

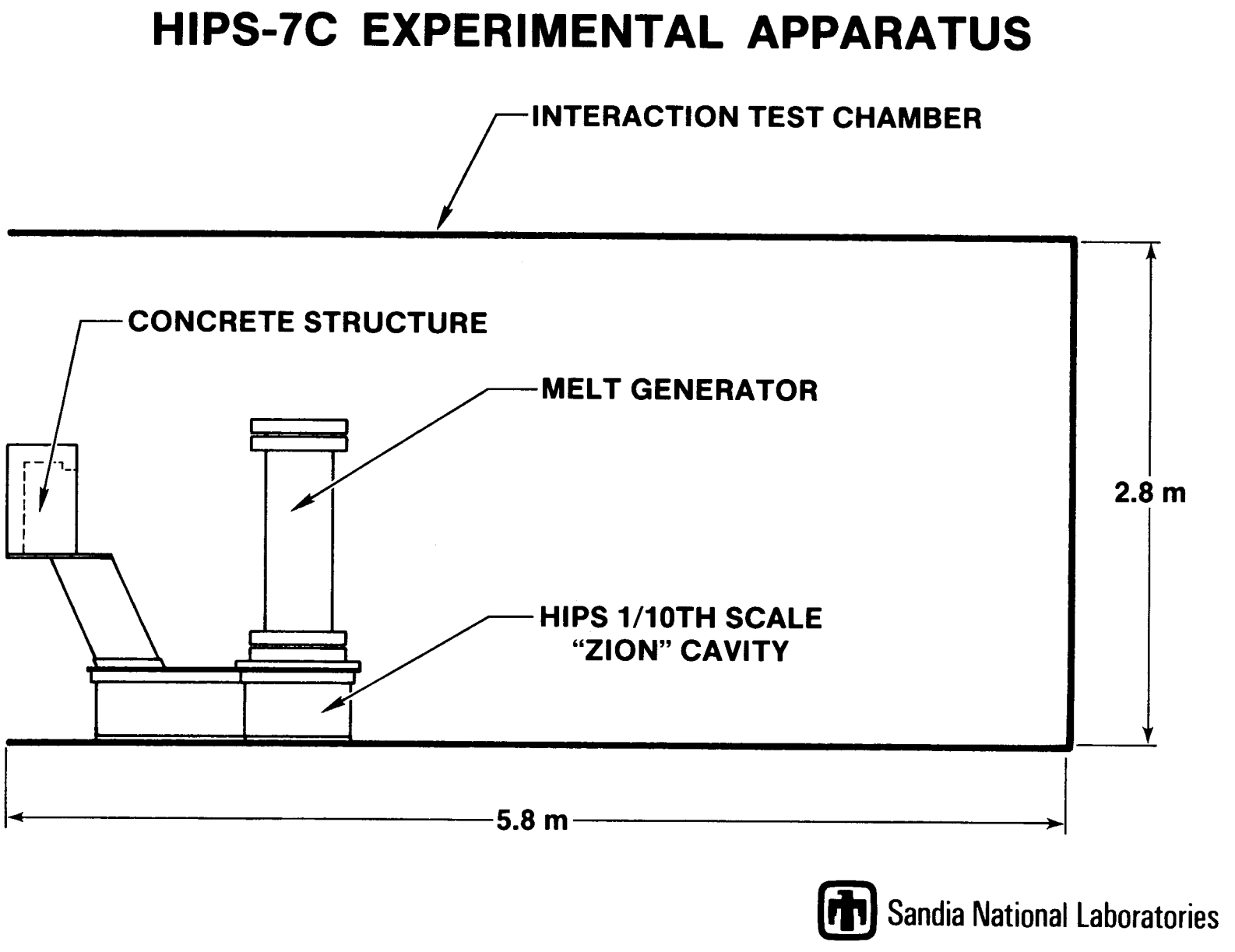

Figure 3.2: Orientation of the Test Apparatus Within the Test Chamber

Table 3.1

Summary of HIPS-7C Instrumentation

Device Type	No.	Range	Location	Purpose
Pressure	1	0-6.9 MPa	Melt Gen	MG Blowdown
Pressure	1	0-6.9 MPa	Gas Line	MG Reference
Pressure	3	0-2.1 MPa	Cavity	Cavity Pressure
Pressure	2	0-0.7 MPa	Chamber	Chamber Pressure
Pyrometer	1	1500-3500RC	Cavity Exit	Chamber Temperature
TC	1	0-1100RC	Melt Gen	Gas Temperature
Photo Detector	1	--	Melt Plug	Timing
Photo Detector	1	--	Cavity	Timing
Cameras	6	10-400 fps		Observation
Filters	2	--	Chamber	Aerosol Concentration
Impactors	3	--	Chamber	Aerosol Size Distribution

melt generator. The location was selected to isolate the device from the high-temperature environment inside the melt generator.

The thermocouple was a Type-K unit with a stainless-steel sheath. The sheath (3.2 mm in diameter) was inserted through the flange cover into the gas volume (46 cm distance) above the thermite reaction crucible.

Three pressure transducers (Kulite XT-190) were attached to the cavity to measure pressure changes caused by the ejected melt. The location of the gauges were in the circular cavity opposite the tunnel opening, halfway along the tunnel, and on the inclined tunnel section. In all cases, the gauge was connected to the internal cavity by a 9.5 mm diameter steel tube through the concrete placed flush with the inner surface. This arrangement has been shown to not significantly degrade the frequency response for the phenomena considered (Tarbell, et al. 1987).

Transient overpressure in the box housing the experiment was measured with two low-range devices (Kulite Model XT-190). These were placed directly through the 6-mm thick steel wall of the box, one along the long side and the second in the closed end opposite the position of the apparatus. The gauge faces were positioned flush with the inner surface of the steel without any external protection.

A two-color pyrometer (Ircon Model R-35C10) was mounted to a bracket on the melt generator and aimed at the cavity opening. The spot size at the cavity opening was nominally 2.5 cm in diameter. The placement was designed to monitor the debris just outside the cavity, but before interaction with the structure model.

The two photodetectors were designed to give a sharp signal output when exposed to the light emanated by the melt. The first was positioned just under the fusible plug to detect the melt just after plug failure. The second was placed on the cavity floor directly under the melt generator. This latter device was shielded so that only light emitted directly into the device would cause a signal output. By comparing the output of the two devices, the average jet velocity from the melt generator to the cavity floor was determined.

The aerosol filters (Millipore Type L5, 47 mm in diameter) and cascade impactors (Anderson Mk-II) were placed outside the chamber and sampled the atmosphere by 12.5-mm diameter steel tubing probes. Each device was controlled by a remotely operated valve on the outlet to isolate the device from a vacuum suction system. By cycling the valve for a set time interval, a critical orifice controlled the volume of gas flowing through the sampler. The aerosol concentration was then determined following the test

by weighing the collected mass in the filter and dividing by the total gas flow through the device. The cascade impactors were actuated in a similar manner with the size distribution determined from the material collected on each sampling stage. A more extensive discussion of these devices can be found in Tarbell et al. (1987).

Table 3.2 summarizes the camera coverage for this test. Six high-speed film cameras plus one video camera recorded the test. In addition, two Hulcher cameras, using 70 mm film, provided high quality still pictures.

3.3 Initial Conditions

The initial conditions for HIPS-7C are summarized in Table 3.3. The gas volume, pressure, and temperature are values at the onset of melt ejection. Direct measurement of the gas temperature failed during this test because the noise level of the thermocouple signal was comparable to the absolute signal itself. The temperature reported in Table 3.3 was determined from the measured pressure rise, estimated volume change (of melt), and the estimated increase in gas mass (from HIPS-3J) during the thermite burn.

3.4 Experiment Results and Analysis

This section presents the results obtained from the HIPS-7C experiment. Analysis of the test is also presented where appropriate to aid in the understanding and interpretation of the experiment observations.

3.4.1 Camera Coverage

Figure 3.3 presents a close-up photo sequence of the test. Photos in the left column were taken looking into the interaction chamber and at the outside back face of the structure mockup. Photos in the right column were taken looking through a plexiglass port on the back wall of the chamber. The structure mockup is mostly hidden behind the melt generator. Melt primarily deflects off the structure in the direction of the back wall. Each photo in the pair (left column and right column) were taken at the same instant in time.

The photo sequence in Figure 3.3 shows that a great deal of melt appears to splash off the structure. Melt is directed downwards, upwards, and to the sides (taken through the port in the back door of the chamber). Late time camera records show a large quantity of material raining down as particles from the ceiling and along the back wall.

Figure 3.4 shows the sequence of events taken from a long-range camera placed outside the interaction chamber. The most striking feature is the intense cloud of aerosols that accompanies the process. The second notable feature is the appearance of melt particles coming out the open side of the

Table 3.2

Summary of HIPS-7C Camera Coverage

Device	Start Time(a) (s)	Speed (fps)	Field of View
Camera	-5	100	50′ Head On
Camera	-5	100	50′ Side On
Camera	+5	400	20′ Head On
Camera	+5	400	20′ Side On
Camera	+5	400	10′ Chamber Rear
Camera	-5	100	100′ Hilltop Rear
Hulcher	-5	10	Hilltop Rear
Hulcher	-5	20	45°
Video		30	

a Relative to ignition of Thermite Powder.

Table 3.3

HIPS-7C Initial Conditions

		Mass (kg)
Melt Mass		81.50
Thermite Composition	Iron Oxide (Fe_3O_4)	61.04
	Aluminum (Al)	18.96
Melt Composition	Iron (Fe) + Alumina (Al_2O_3)	
Dopants	ZrO	0.25
	La_2O_3	0.25
	Mo	0.50
	Nb	0.50
Gas	Carbon Dioxide (CO_2)	
Melt Generator Gas Volume	0.118 m^3	
Pressure	5.58 MPa	
Temperature	526 K	
Melt Plug Diameter	0.0191 m	

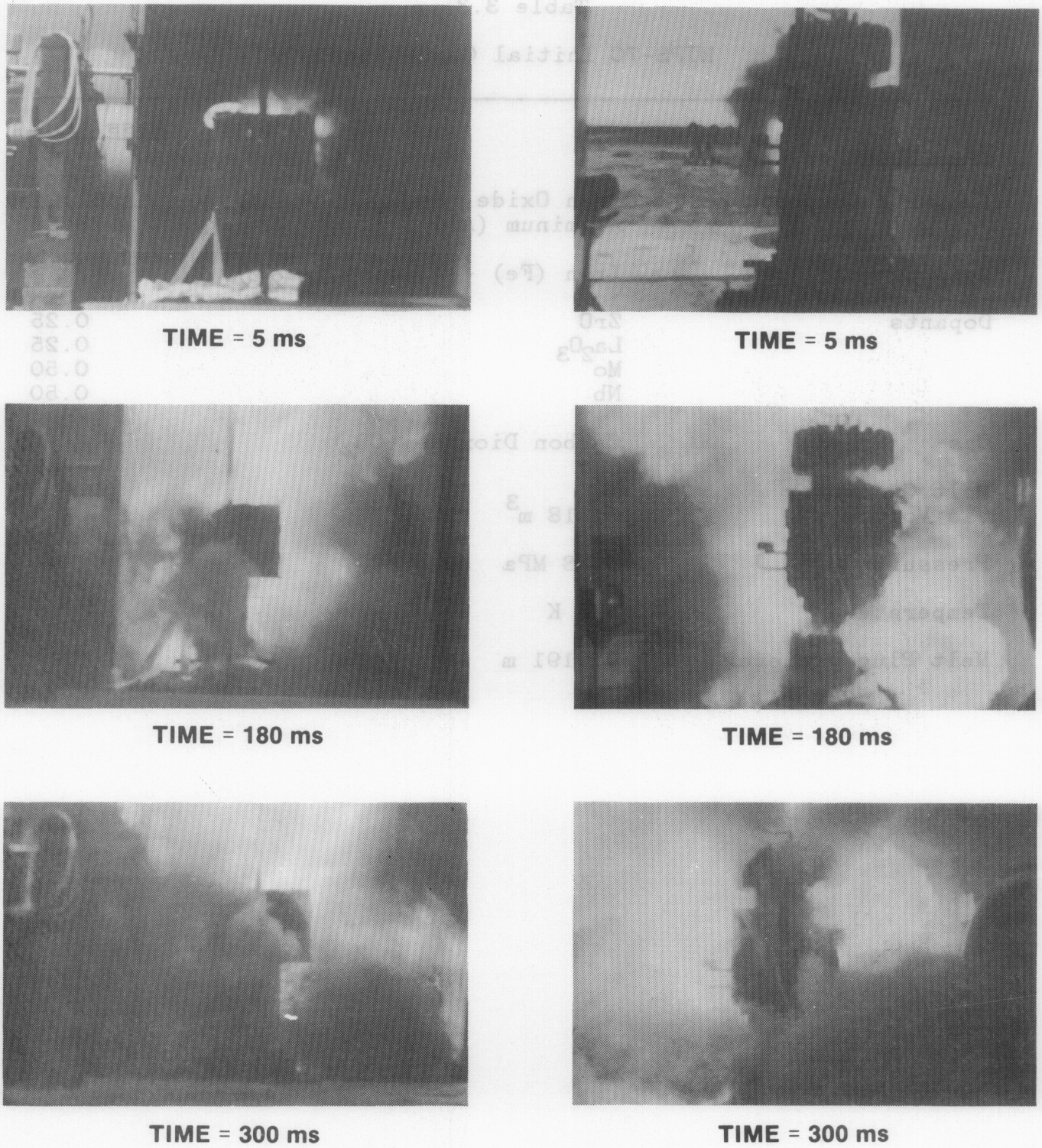

Figure 3.3: Closeup Photo Sequence Taken From the Rear (Left Column) and Front (Right Column) of the structure.

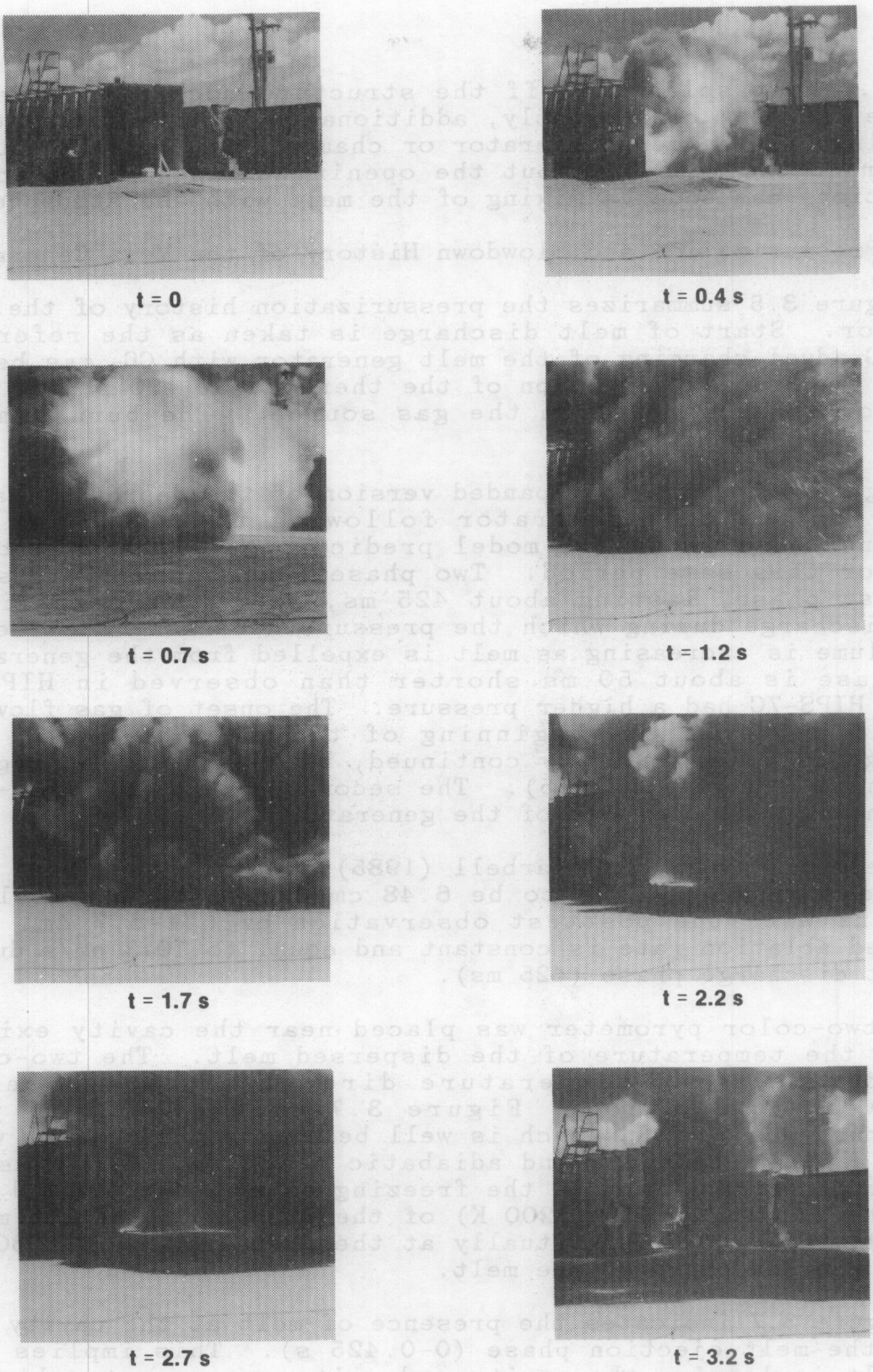

Figure 3.4: Long Range Photo Sequence

chamber. Melt splashing off the structure mockup is directed into the chamber; consequently, additional structure interactions (splashing off the melt generator or chamber walls) are required to redirect the melt back out the opening. Vigorous structure interactions can enhance mixing of the melt with the atmosphere.

3.4.2 Pressurization and Blowdown History of the Melt Generator

Figure 3.5 summarizes the pressurization history of the melt generator. Start of melt discharge is taken as the reference time. Gradual charging of the melt generator with CO_2 gas begins at -330 s. Prior to ignition of the thermite at -20 s, the melt generator is isolated from the gas source. The burn time is 20 s.

Figure 3.6 shows an expanded version of the depressurization history of the melt generator following the onset of melt ejection. Also shown are model predictions (Pilch & Tarbell, 1985) for this same period. Two phases can be distinguished. The first phase, lasting about 425 ms, corresponds to liquid phase discharge during which the pressure decreases because the free volume is increasing as melt is expelled from the generator. This phase is about 50 ms shorter than observed in HIPS-3J because HIPS-7C had a higher pressure. The onset of gas flow out the orifice marks the beginning of the second phase. Gas discharge is accompanied by continued, but reduced discharge of melt (Pilch & Tarbell, 1985). The second phase lasts 1.5 - 2 s at which time the blowdown of the generator is complete.

The model of Pilch & Tarbell (1985) predicts the final size of the discharge orifice to be 6.48 cm, which is in excellent agreement with the posttest observation of 6.1-6.7 cm. The predicted ablation rate is constant and equal to 10.3 cm/s during the melt discharge phase (425 ms).

A two-color pyrometer was placed near the cavity exit to measure the temperature of the dispersed melt. The two-color pyrometer measures temperature directly and requires no emissivity correction. Figure 3.7 shows that the peak temperature was 2350 K, which is well below the theoretical value of 3200 K for a complete and adiabatic reaction. The measured temperatures are well above the freezing point (1700 K) and well below the boiling point (3200 K) of the iron phase of the melt. The peak temperature is virtually at the freezing point (2300 K) for the alumina phase of the melt.

Figure 3.7 indicates the presence of melt at the cavity exit during the melt ejection phase (0-0.425 s). This implies that some melt is leaving the cavity under its own momentum because blowdown gases have not yet entered the cavity. There is an abrupt, but temporary, drop in output at 0.825 s, which might indicate when most of the melt is dispersed from the cavity. The final drop in output occurs at 1.2 s, which corresponds closely to the end of the blowdown phase (see Figure 3.5).

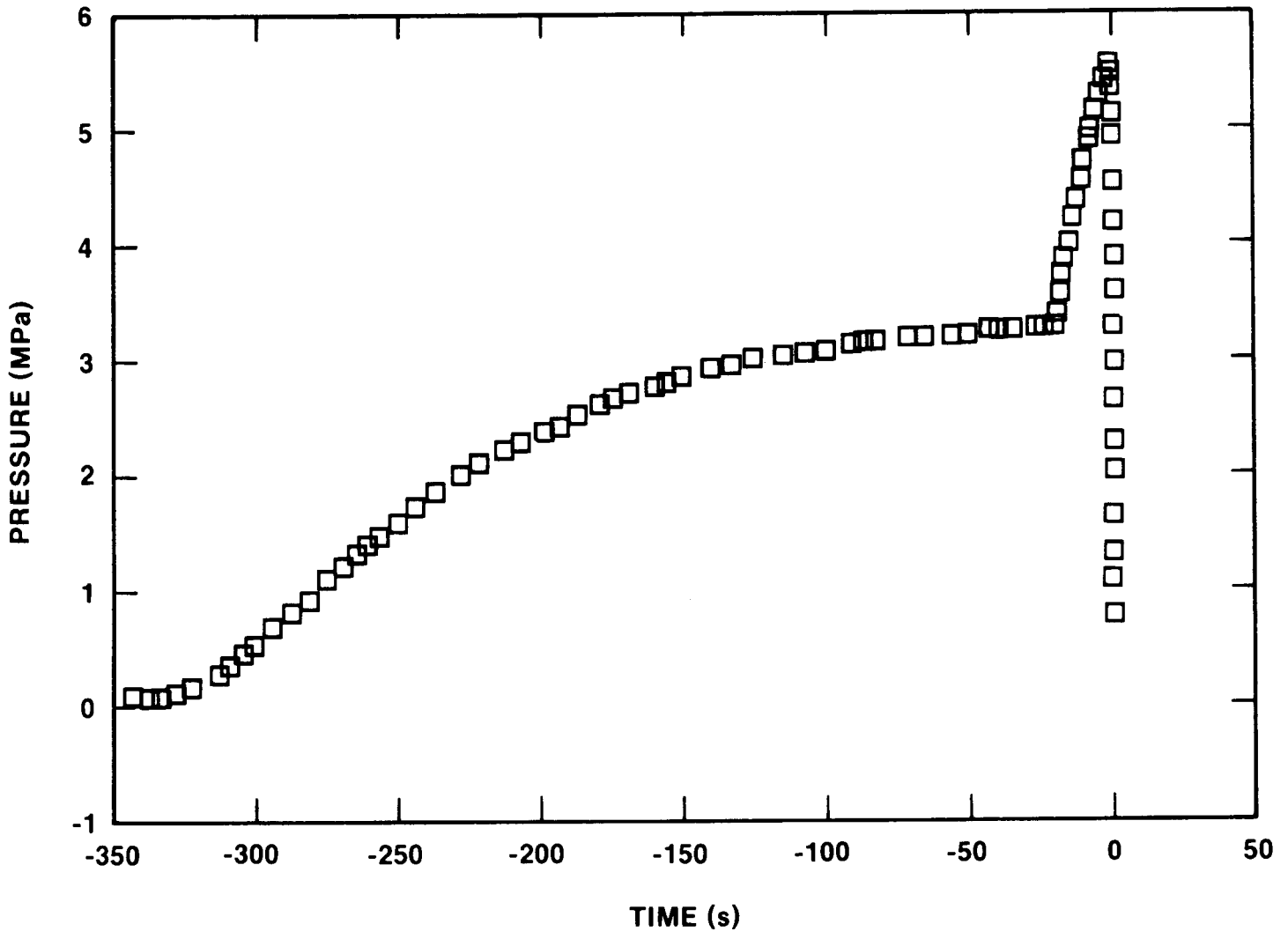

Figure 3.5: Pressurization History of the Melt Generator

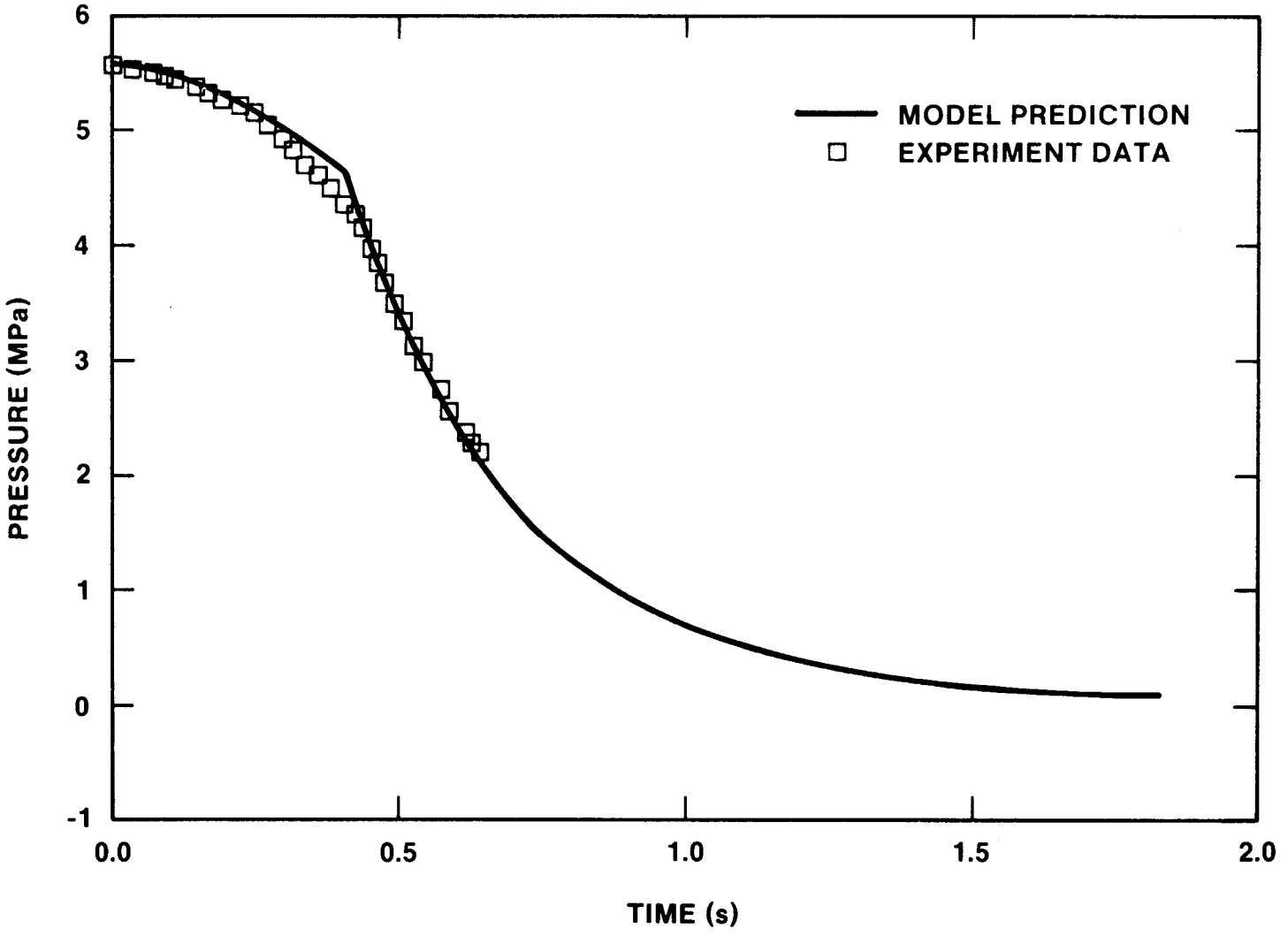

Figure 3.6: Blowdown History of the Melt Generator

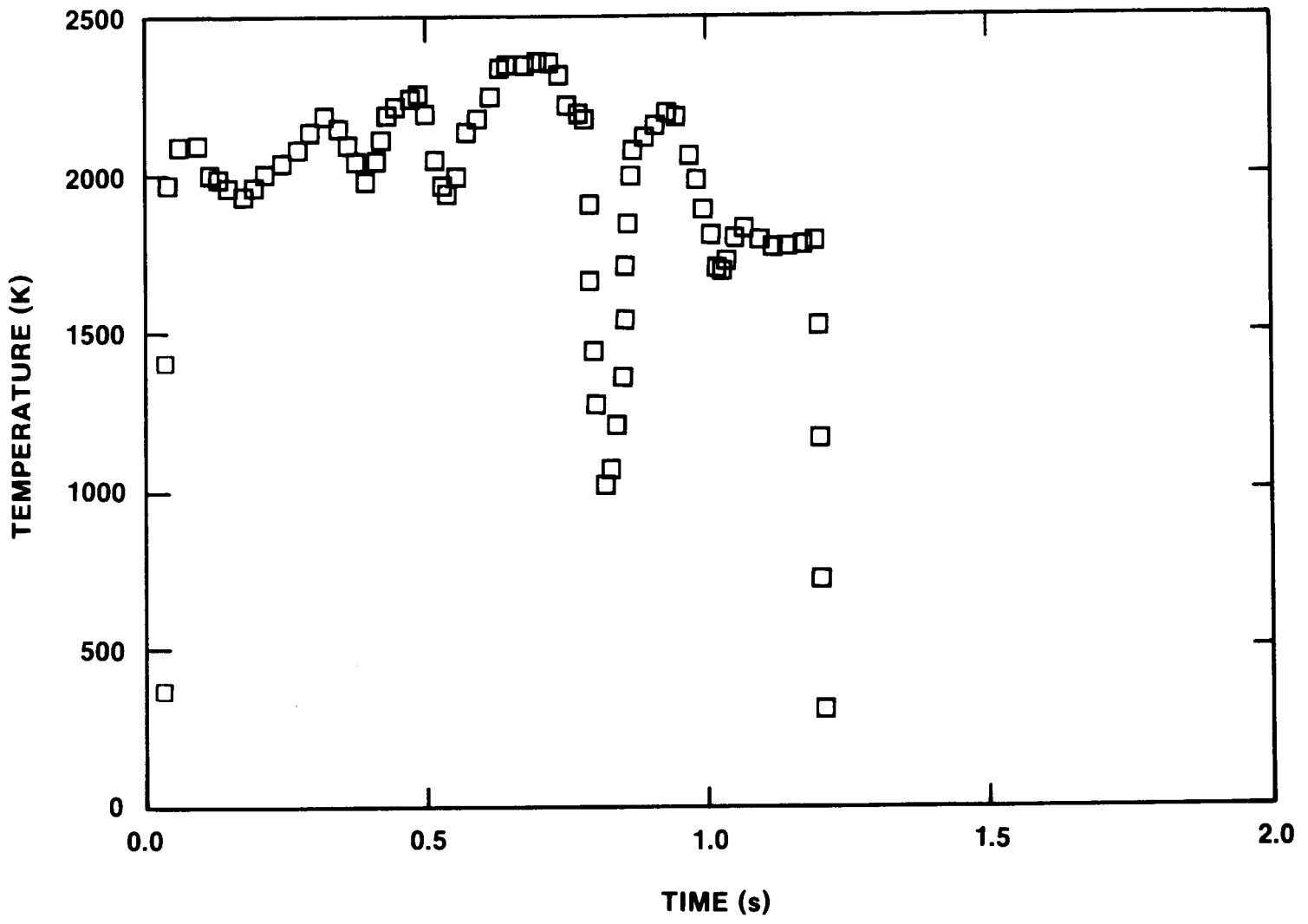

Figure 3.7: Temperature Measurements Outside the Cavity Using a 2-Color Pyrometer

Figure 3.8 shows pressure measurements made at three different locations in the cavity. The measured back pressures in the cavity are small compared to pressures in the melt generator. The measured pressures drop abruptly at about 0.8 s, which coincides with the temporary drop in the pyrometer output. This might be an indication of the end of the dispersal phase. Beyond 0.8 s, the measured pressure in the cavity oscillates wildly from positive to negative values and are not shown on Figure 3.8. It is believed that hot aerosol or high heat fluxes were adversely affecting the pressure transducers.

3.4.3 Structure Interactions

Table 3.4 shows the posttest location of the debris for the HIPS-7C test, which accounts for 97% of the melt. Some of the melt particles that come out the opening in the chamber, land on the concrete pad and some land in the dirt beyond the pad. The latter are not accounted for in the posttest mass inventory. In addition, some aerosol mass is unaccounted for in the aerosol cloud that billows out of the chamber.

The posttest mass inventory shows that approximately 2.7 kg of melt remained in the melt generator. This agrees well with the predicted value of 2.2 kg using the model of Pilch & Tarbell (1985). The model couples the competing rates of melt and gas discharge with hole ablation calculations and a criteria for the onset of gas blowthrough.

Approximately 1.3 kg of debris was found adhering to the inside of the concrete cavity, as a very thin crust (Figure 3.9). Thus, 98% of the melt ejected from the melt generator was dispersed from the cavity. This result is consistent with other HIPS tests using concrete cavities (Tarbell et al. 1986). Dispersal from cavities of this type is nearly complete.

The design of the HIPS-7C apparatus places the melt generator in the path of some of the debris that leaves the excavity structure. Posttest examination of the outside of the melt generator (Figure 3.10) reveals a crust of melt that is 1.0-1.4 mm thick. The expected crust thickness that could develop during the melt relocation time (0.4-1.0 s) is given by:

$$\delta = 2\lambda \ (\alpha t)^{1/2}$$

where $\lambda = 504$ and $\alpha = 2.8 \times 10^{-6}$ for molten iron/alumina melt on steel. Thus, a crust thickness of 1.1-1.7 mm, which is in substantial agreement with observation for this test. In this test, the mass flux of melt onto the steel surface of the melt generator could be two orders of magnitude larger than the freezing flux (assuming all the dispersed melt strikes the steel surface). Consequently, the melt/steel interaction is predominantly hydrodynamic with only a small fraction of the melt being trapped by freeze-out and with the bulk of the melt splashing from the surface.

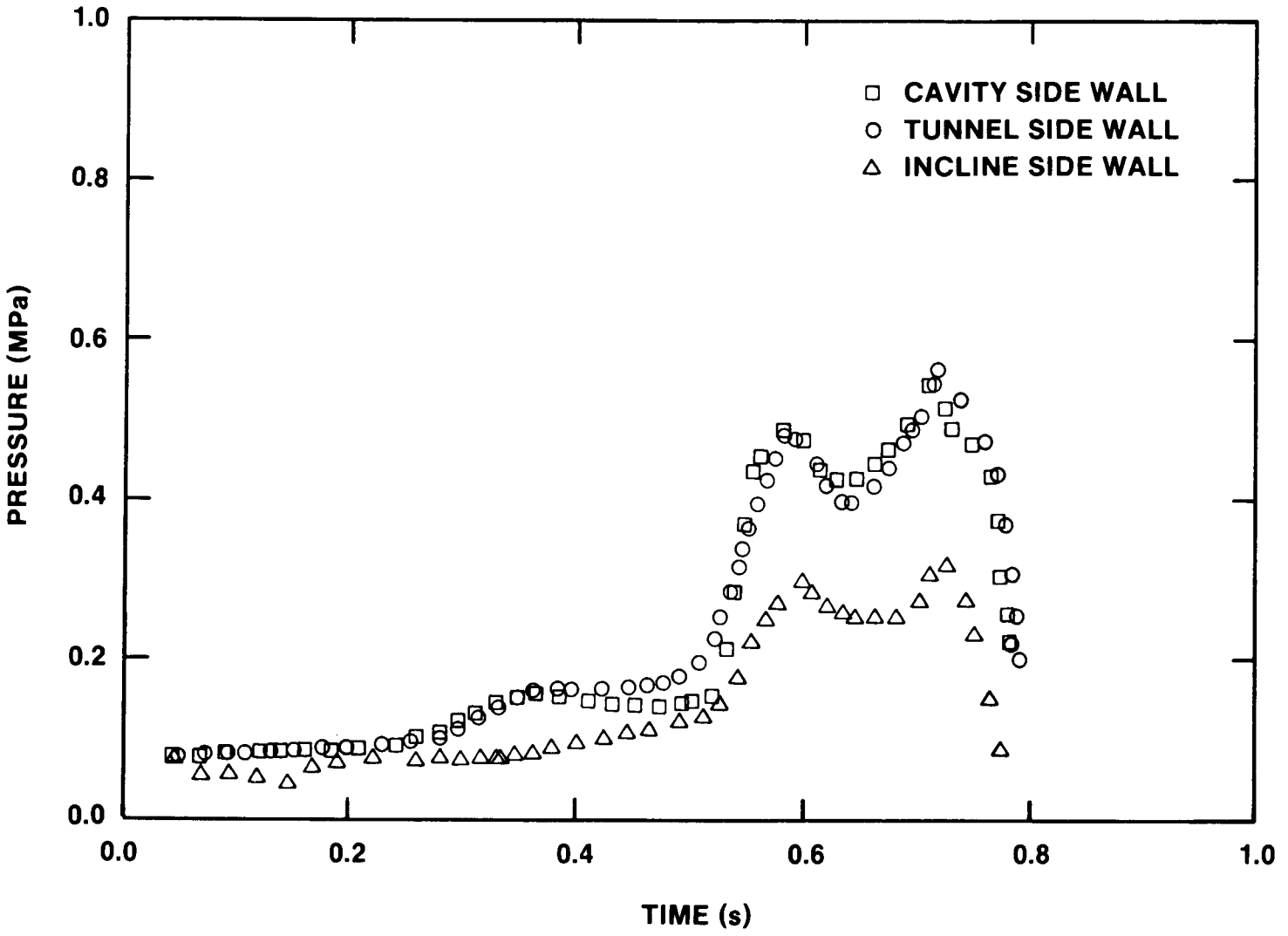

Figure 3.8: Pressure Measurements at Three Locations in the Cavity

Table 3.4

Posttest Debris Inventory

	Mass (kg)
Remaining inside melt generator	2.716
Adhering to inside of concrete cavity	1.295
Adhering to outside of melt generator and its mounting plate to concrete cavity	13.313
Adhering to ceiling above the excavity structure	0.210
On floor of chamber, back 1/4	24.219
On floor of chamber, back center 1/4	9.826
On floor of chamber, front center 1/4	14.314
On floor of chamber, front 1/4	8.584
On concrete pad outside chamber	1.845
Retained by excavity structure	3.290
	79.612

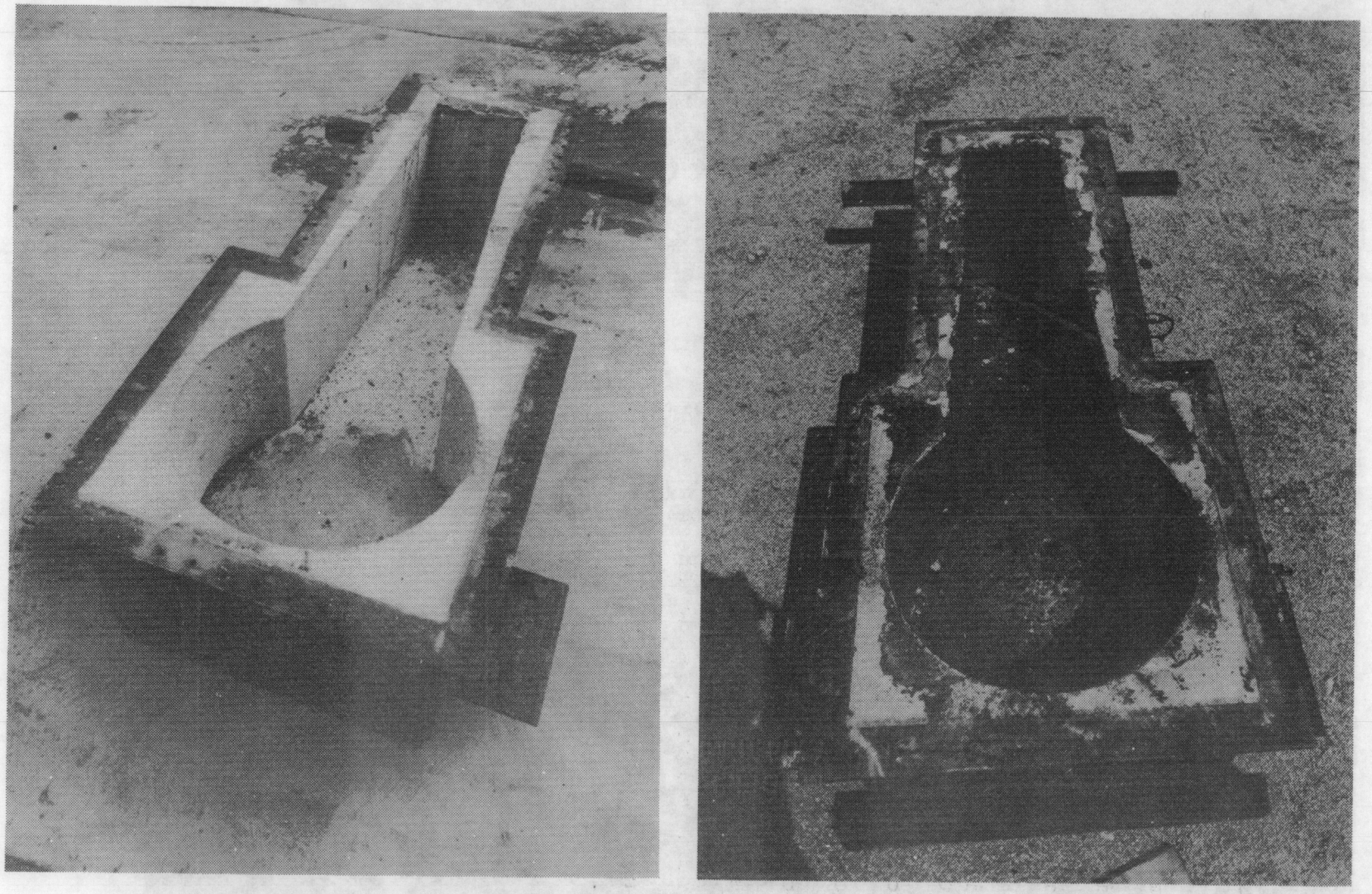

Figure 3.9: Pretest and Posttest Comparison of Lower Assembly of the Cavity Mockup

Figure 3.10: Posttest View of the Melt Generator With Frozen Crust on its Surface

The 0.21 kg of material collected from the ceiling of the containment chamber directly over the excavity structure has the appearance of fine particles sprayed onto the ceiling. Photomicrographs show the bulk of this material to be comprised of sintered particles with diameters less than about 10 μm. Analysis shows that particles of this size will deflect with the gas stream and not impact the structure. Details of this analysis will be discussed later.

Most of the debris (56.9 kg) recovered after the test was found on the floor of the interaction chamber. Of this debris, 42.5% (24.2 kg) was recovered along the back wall of the chamber. High speed films reveal that a large, though indeterminant, portion of this melt rains down from the ceiling near the back wall of the chamber. Most of the debris recovered from the floor was in the form of large coherent masses, indicating that the material was still molten when it struck the floor.

Finally, Table 3.4 shows that only 3.3 kg, representing only 4% of the melt swept from the cavity, was retained by the excavity structure. The quantity of retained material is significantly less than the geometry of the structure might suggest. If the roof of the structure is filled with melt to the lip of the overhang, then 24.5 kg of material could be retained, which in turn is significantly less material than could be supported by the peak stagnation pressure of gas. Figure 3.11 shows the structure as it appeared before and after the test. A coherent crust (<1.5 cm thick) was found along the top back edge, which is where the melt struck the structure. Elsewhere on the structure, the melt appears as splatter clinging to the surface. Much of the retained material was found along the bottom back edge of the structure with an additional crust spread over the steel "floor" outside the cavity.

The following analysis suggests that nearly all the melt struck the structure, although retention was minimal. Figure 3.12 depicts a melt particle that is being swept from the cavity by blowdown gas moving at velocity V_0. Outside the cavity, the gas is assumed to deflect 90 degrees by the structure. The gas velocity (V_1) after deflection is less than the gas velocity in the cavity because of an increase in flow area. Melt particles are deflected from their straight line path by the gas stream. Owing to their inertia, large particles will not be deflected sufficiently to escape impact with the structure walls. The fraction (f) of particles with diameter (d) that impact (and are potentially trapped by) the structure is given by Cook [1987] as

$$f = \frac{1}{\lambda W} \ln \left\{1 + \lambda W\left[\frac{W}{L} - \left(\frac{W}{L} - 1\right) f\right]\right\}$$

where

$$\lambda W = \frac{3}{4} C_d \frac{\rho_g}{\rho_1} \frac{W}{d} .$$

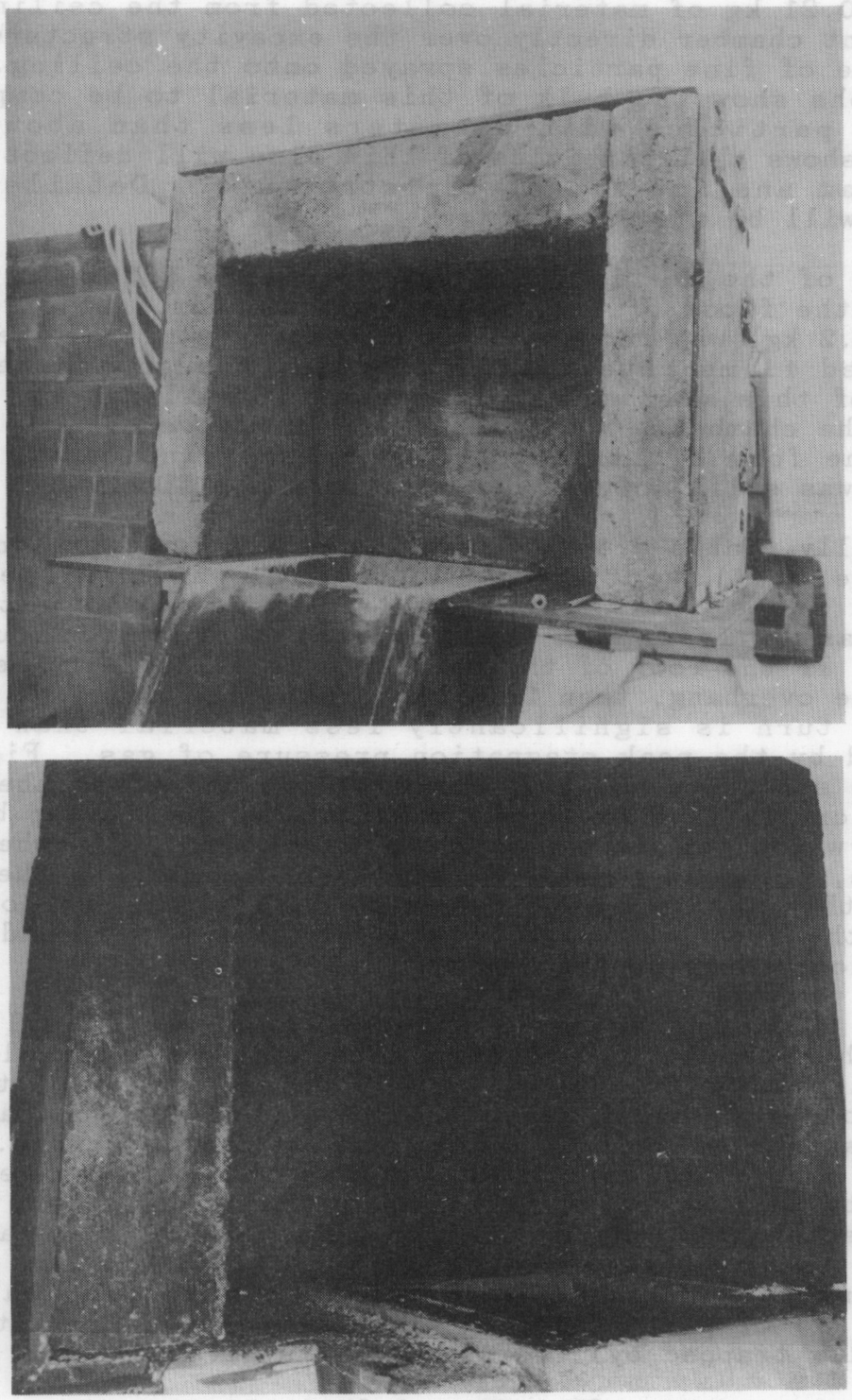

Figure 3.11: Pretest and Posttest Comparison of the Excavity Structure

Here, C_d is the drag coefficient on the particle, ρ_γ is the gas density, $\rho_<$ is the particle density; and W and L are geometric dimensions as illustrated in Figure 3.12.

Figure 3.13 shows the fraction of particles that are deflected away from the structure by the redirected gas stream without ever striking it. For a mass mean particle size of 500 μm (Tarbell et al., 1986), more than 95% of the particles are expected to strike the HIPS-7C structure. Figure 3.13 shows that the foreshortened geometry enhances the potential for trapping in scaled experiments over the full-size reactor geometry. The results from the HIPS-7C experiment show that the debris does interact with the enclosure, but the test observations do not support the implied analytical assumption that the debris is trapped.

The discrepancy in the trapped fraction arises because the analysis assumes that particles striking the structure are trapped. The bulk of the melt does strike the structure; however, vigorous splashing "reentrains" the melt back into the deflected gas stream. The vigorous splashing of melt from the concrete slab in the HIPS-3J test supports this hypothesis. Splashing as a dominant reentrainment mechanism was also reported by Dallman & Kirchner (1980) in their studies of water drop deentrainment in the upper plenum of a PWR during the reflood stage of a loss-of-coolant accident. They reported that 80-90% of the water striking the structures was reentrained by splashing. They observed even more reentrainment if the gas velocity was sufficiently high to cause reentrainment by the classic mechanisms of Kelvin-Hemholtz instability.

The material collected from the ceiling of the containment chamber directly over the excavity structure supports the theory that small particles can be deflected with the gas stream and not interact with the excavity structure. The 0.21 kg of material found in this location has the appearance of fine particles being sprayed onto the ceiling. Photo-micrographs show that the bulk of this material to be comprised of sintered particles with diameters less than 10 μm. Particles of this size are consistent with the preceding analysis, which predicts that they will deflect with the gas stream and not impact the structure.

3.4.4 Aerosols

An intense cloud of aerosols has been observed in all HIPS tests [Tarbell, Brockmann & Pilch, 1983, 1984; Brockmann & Tarbell 1984A, 1984B; Tarbell et al., 1986], and the HIPS-7C test is no exception. Aerosol measurements were made inside the HIPS-7C containment chamber. Figure 3.14 shows that the aerosol size distribution is bimodal: a small size peak (aerodynamic diameters < 3 μm) characteristic of condensation aerosols, and a large size peak characteristic of fragmentation processes. Similar aerosol distributions have been reported for unconfined jet experiments and other scaled cavity tests [Tarbell et al., 1986].

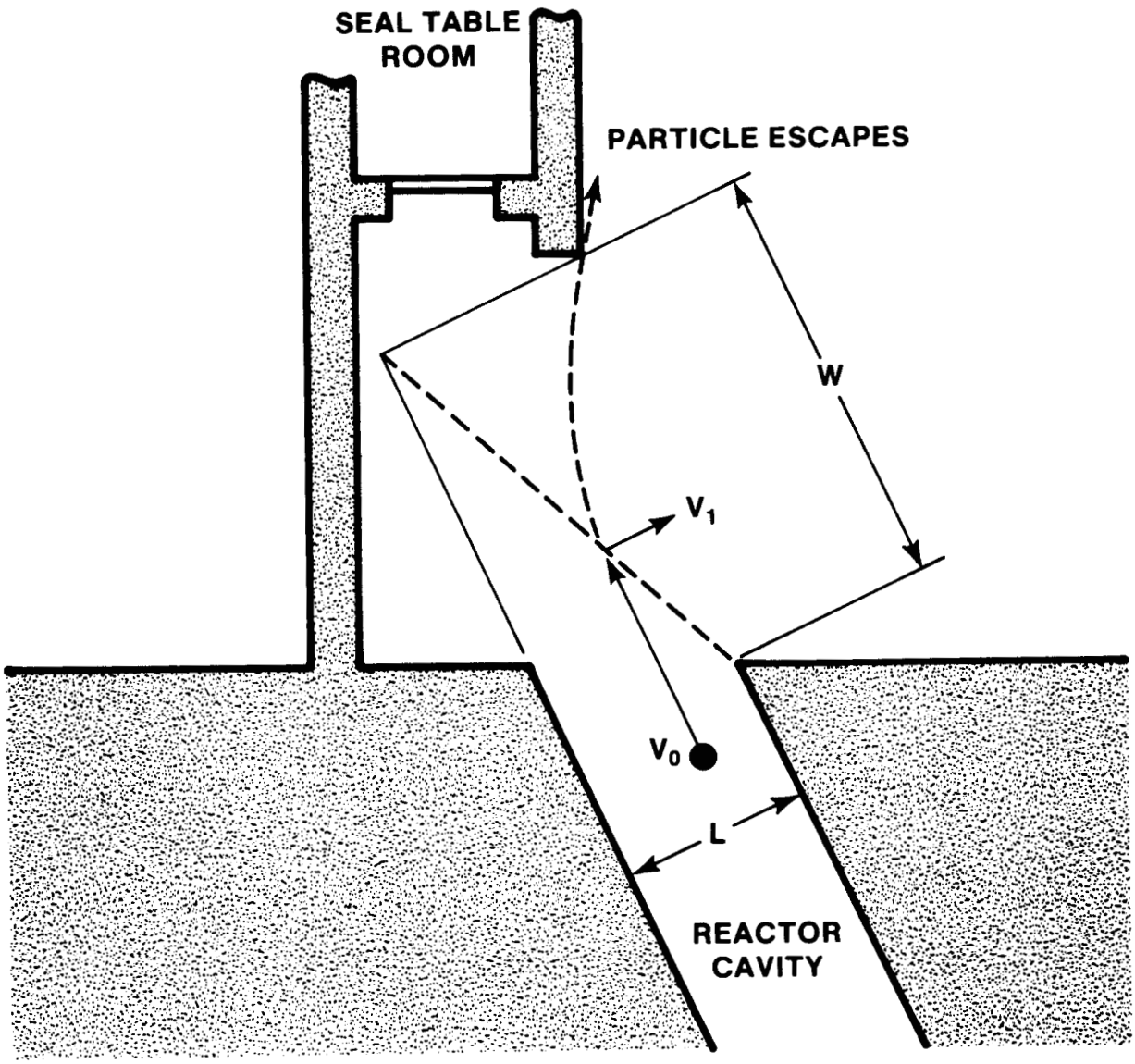

Figure 3.12: Particle Trapping by Excavity Structure

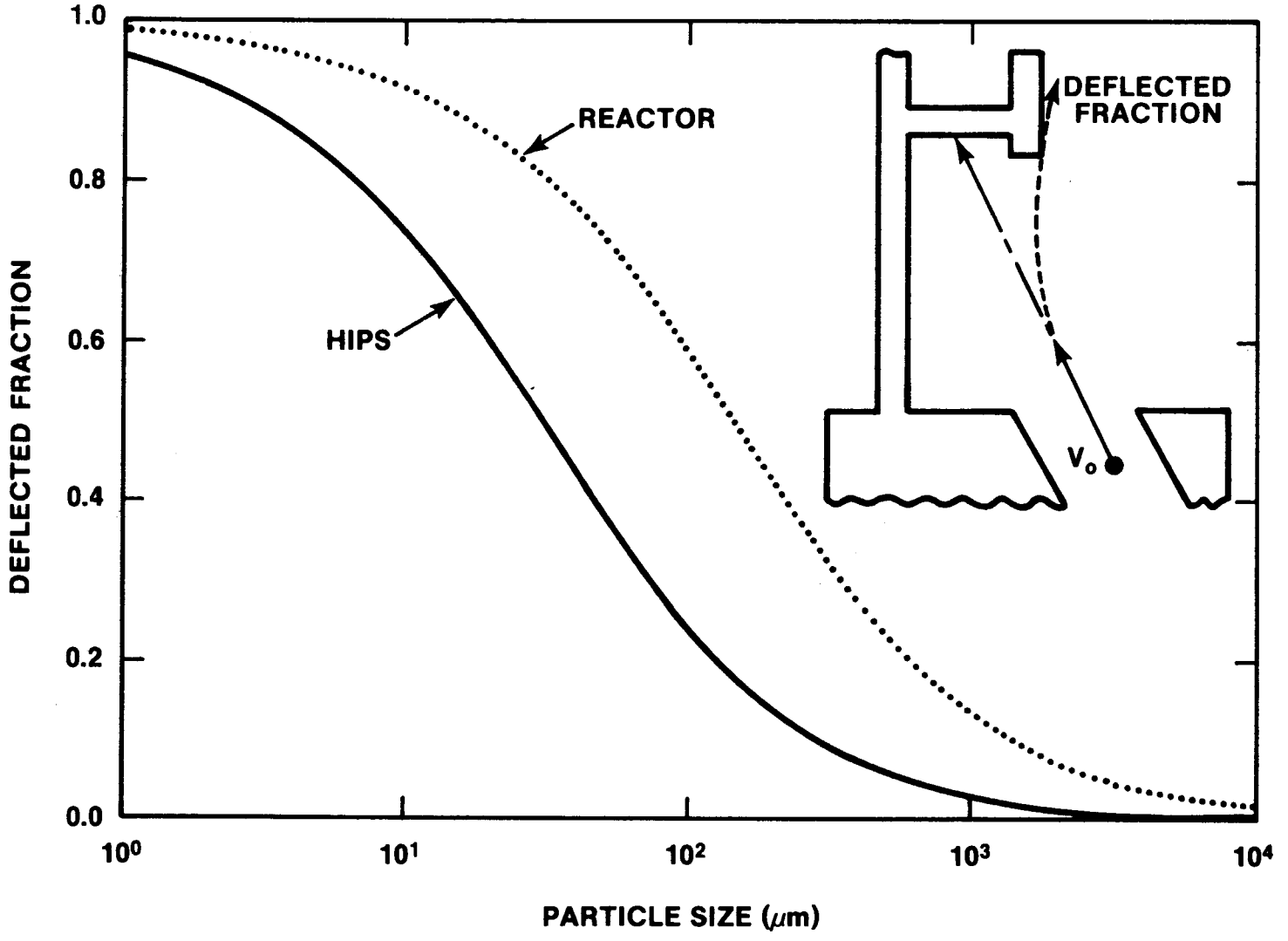

Figure 3.13: Influence of Containment Structures on Debris Behavior

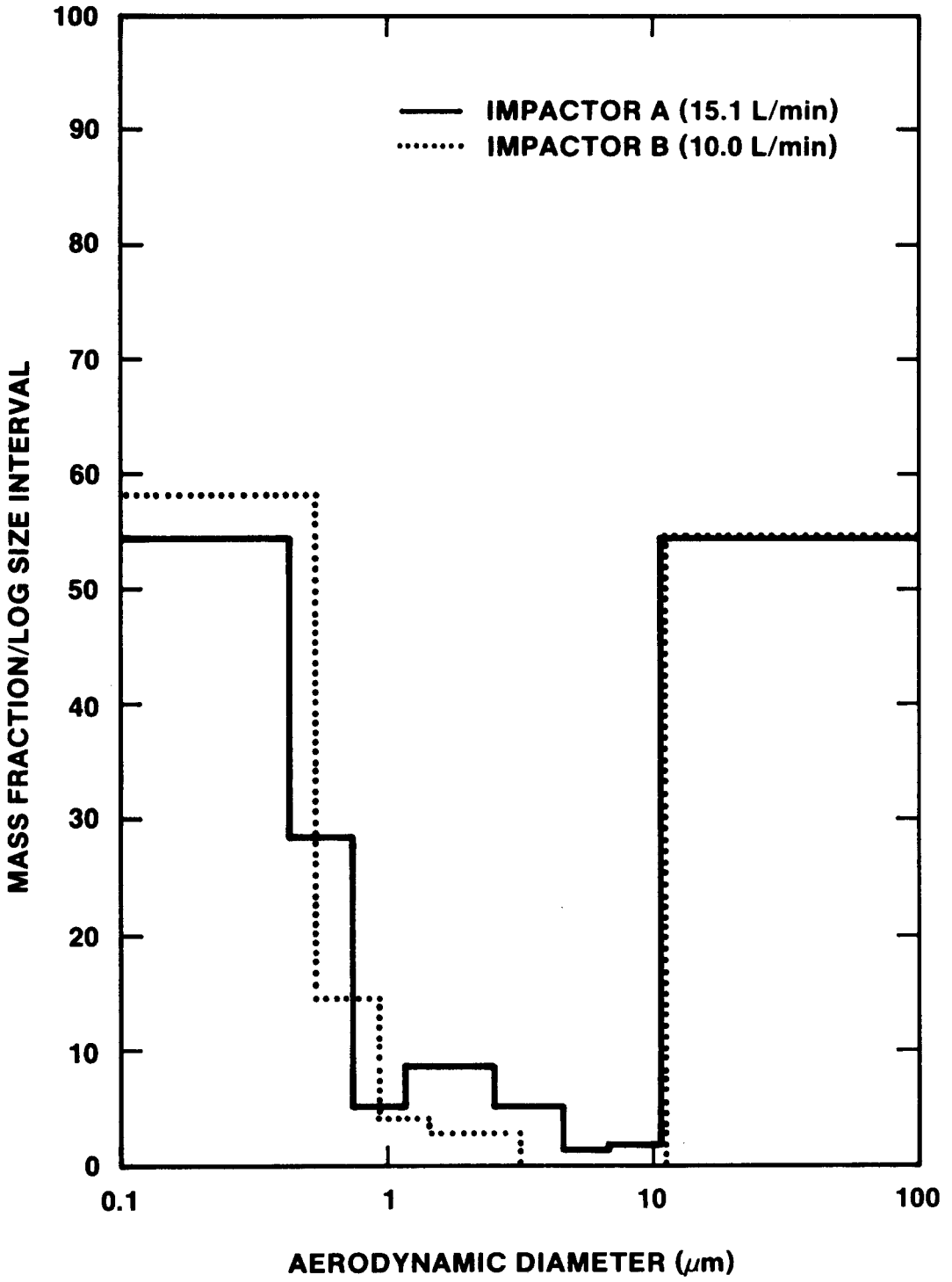

Figure 3.14: Aerosol Size Distributions

Figure 3.15 shows the estimated fractions of relocated melt that are less than 10 μm and less than 1 μm in size. The two SPIT tests [Tarbell et al., 1986] indicated in Figure 3.15 are 1:20 linearly scaled cavity tests involving 10.3 kg of iron/alumina melt. The uncertainty in these results is an indication of the difficulty in obtaining accurate aerosol mass loadings unless complete containment of the atmosphere can be attained. In the HIPS-7C test, the aerosols were not completely confined in the chamber and the cloud volume is estimated from photographs. There appears to be a higher fraction of condensation aerosols in the HIPS-7C test than in the two SPIT experiments. It is not clear whether this effect is related to the larger melt mass or whether it is related to the excavity structure.

Brockmann & Tarbell (1984A) showed that the abundance of iron and alumina (the bulk constituents of the melt) in the condensation aerosols could be ranked by their respective vapor pressure at the melt temperature. Fission product mocks were added to the melt in HIPS-7C in an attempt to extend these results to other constituents. All melt constituents, including fission product mocks, were detected in the aerosols using X-ray microprobe analysis. Release fractions for the constituents were not attempted because of the large uncertainty in the total mass of aerosol.

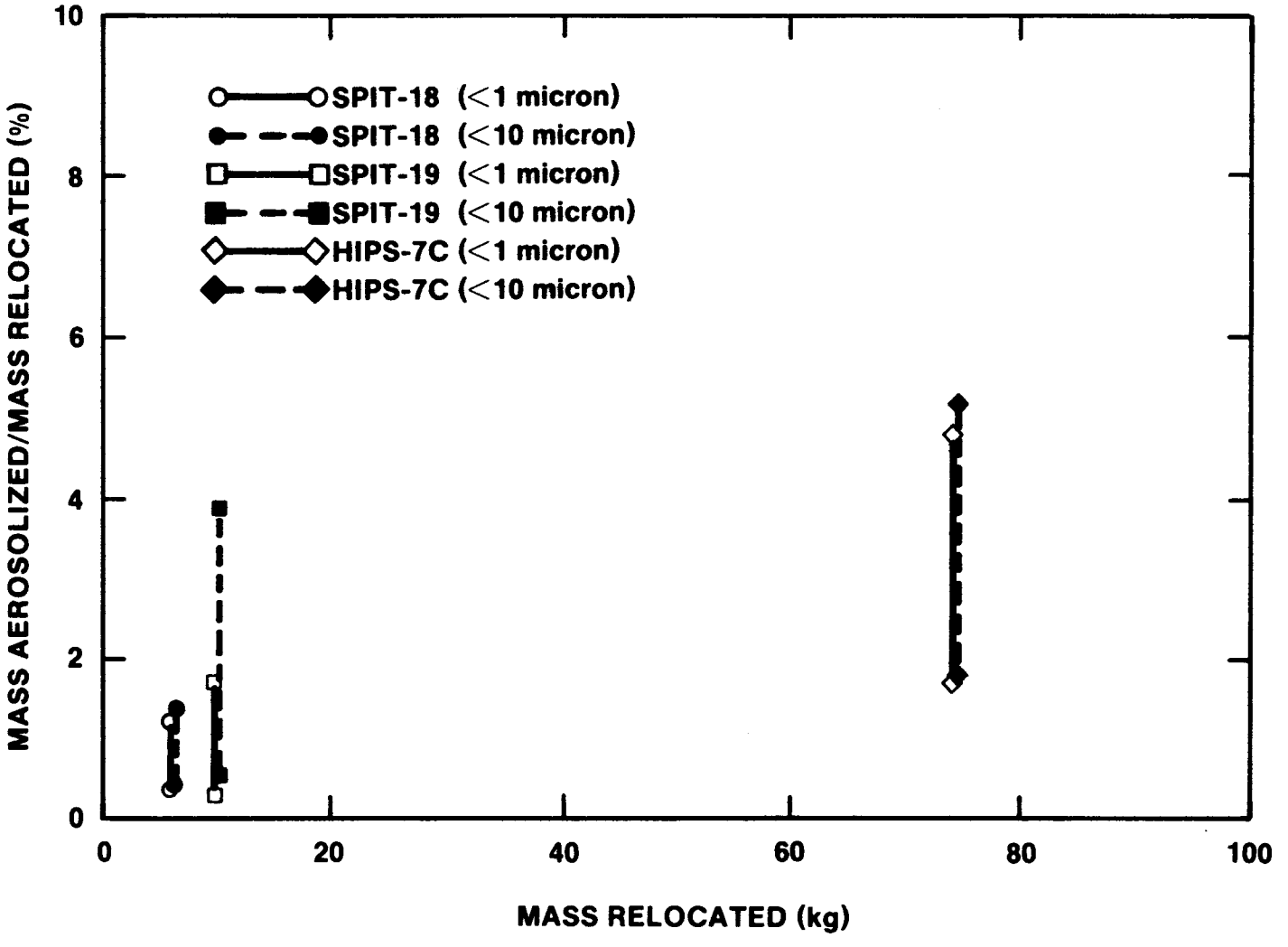

Figure 3.15: Fraction of Relocated Melt That is Aerosolized

4. THE HIPS-8C EXPERIMENT

The objective of the HIPS-8C experiment was to determine the potential for debris to escape the cavity via the annular gap between the reactor pressure vessel and the cavity wall. In most plants (and the Zion plant in particular, see Figure 1.1), this gap represents a pathway through which core debris can be dispersed directly from the cavity into the upper dome of the containment. This escape path bypasses the potential mitigation of structures located outside the normal cavity exit and the lower regions of the containment. The melt generator and cavity assembly (but not the excavity structure) used in the HIPS-7C test was modified to include a mockup of this escape path. The fixture was placed in a chamber in such a way that debris escaping the cavity through the annular gap could be separated and collected.

4.1 Apparatus

The experiment used the same melt generator and scale model of the Zion cavity from the HIPS-7C test except that a simulated annular gap was placed at the scaled height of the RPV. As depicted in Figure 4.1, the melt generator and cavity model were connected by a transition piece. The transition piece was used to form the annular gap and to deflect dispersed melt away from the bottom flange of the melt generator. The transition piece was made from 6.4-mm thick steel plate and included a 15.2-cm ID tube to duct material from the discharge orifice in the melt generator to the cavity below.

In the Zion plant, the gap between the RPV and concrete wall is partially filled by thermal insulation, constructed of multiple layers of thin metal sheets, each separated by a 1-2 cm air space. The width of the gap, with and without the insulation in place, is estimated to be 7 cm with and 14 cm, respectively. It is assumed that the insulation will be an insignificant hindrance to the flow of debris through the gap region. Therefore, the width of the gap in the experimental apparatus (1.3-1.4 cm) was based on a 1:10 linear scaling of the Zion geometry without the thermal insulation.

The apparatus in the HIPS-8C experiment is placed so that the normal cavity exit is just outside the end cover of the interaction chamber (see Figure 4.2). The cover was sealed around the apparatus so that the annular gap was inside the chamber. In this manner, the division of dispersed debris between the two exits could be estimated by a posttest collection of the mass in the apparatus and chamber. The debris leaving the normal cavity exit was directed against an inclined Plexiglass surface (see Figure 4.2) to observe the interaction of the particles with the surface of an obstruction. The rear wall of the interaction chamber was modified to include a baffle that would trap all debris within the chamber while allowing the heated chamber atmosphere to vent, thus preventing over pressurization.

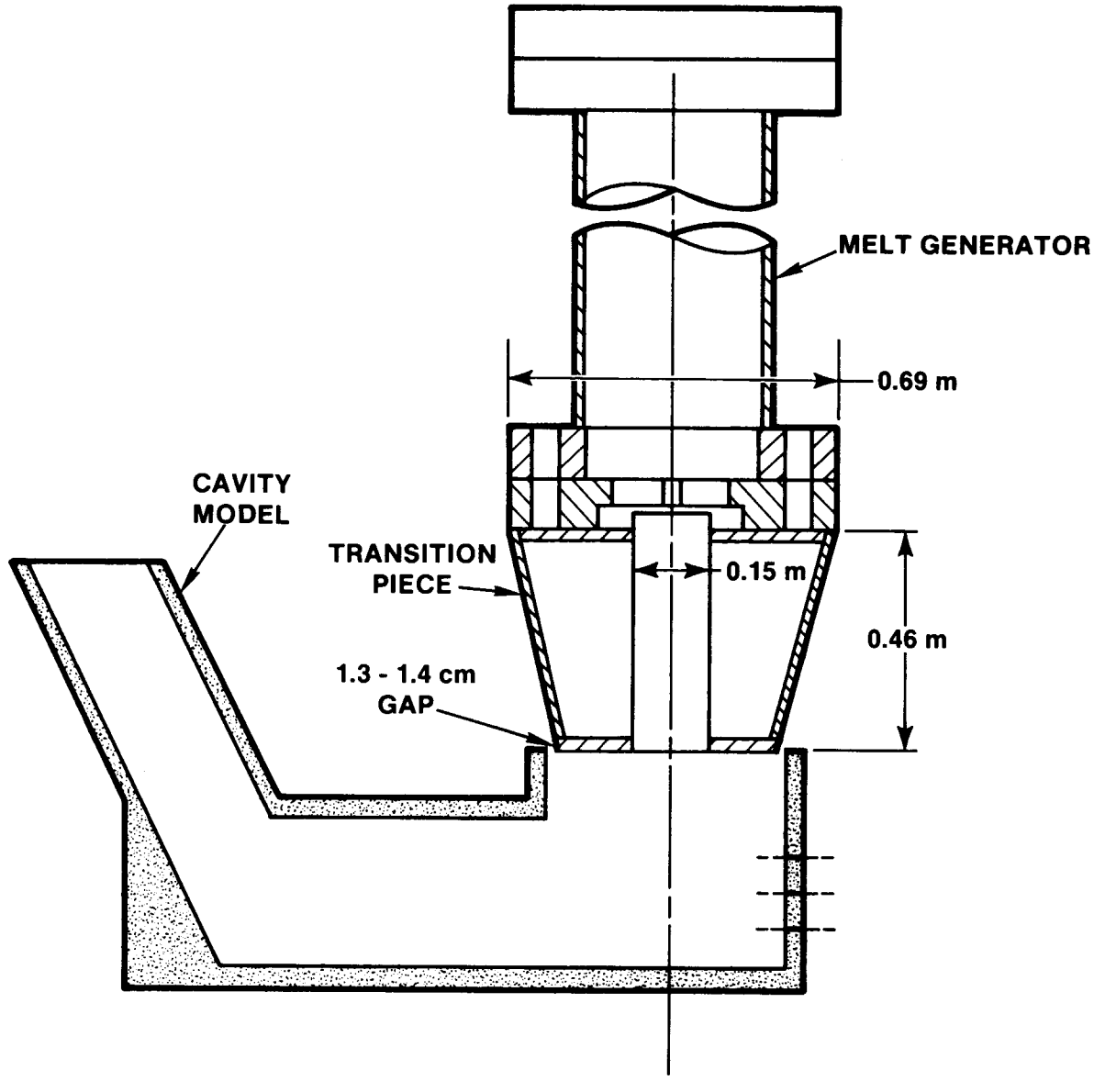

Figure 4.1: Details of the Melt Generator, Transition Piece, and Cavity Configuration

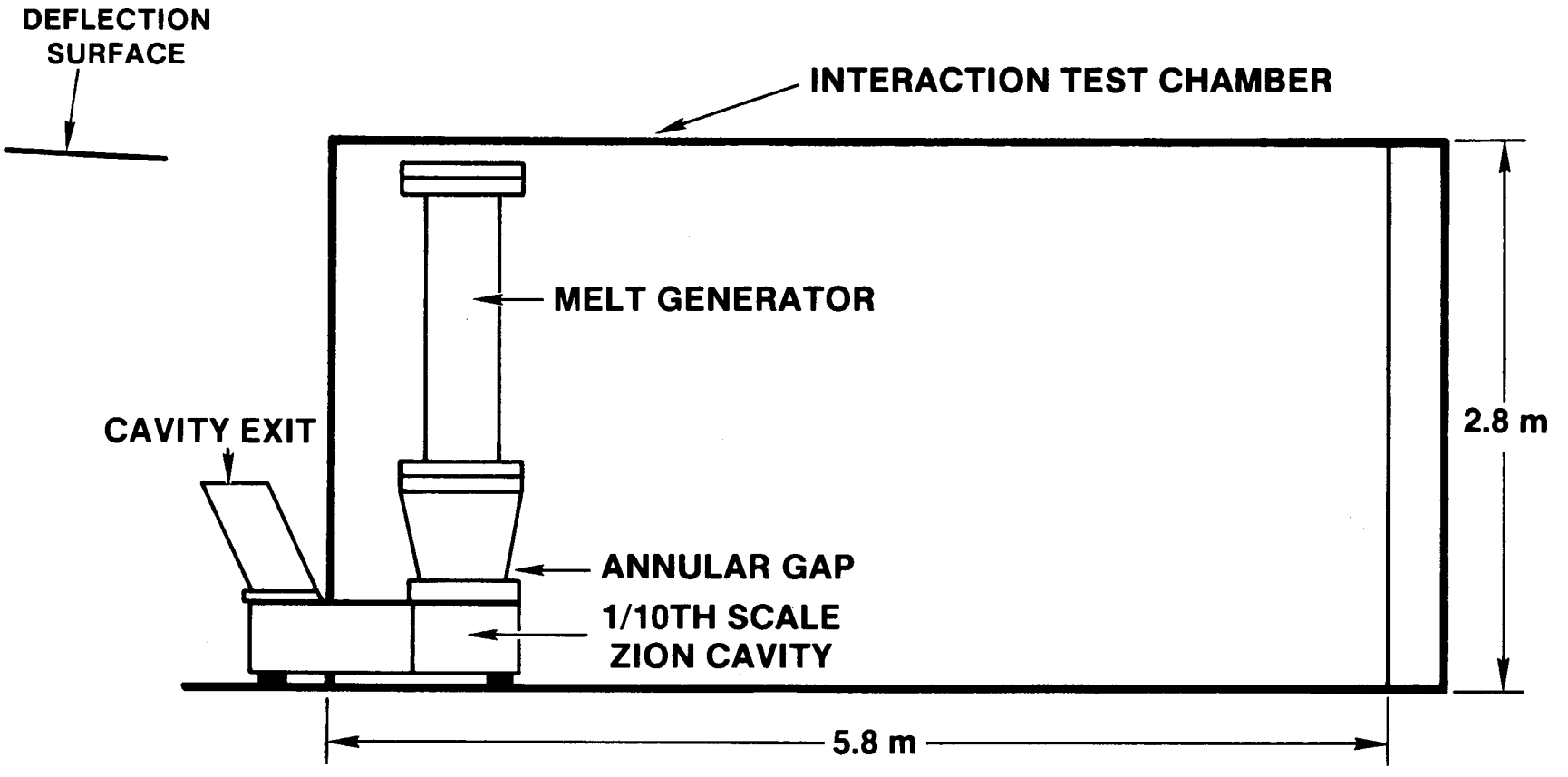

Figure 4.2: Arrangement of the Test Apparatus In the Interaction Chamber

4.2 Instrumentation

A summary of the HIPS-8C instrumentation is given in Table 4.1. Two pressure gauges (Kulite He14-375) were used to monitor the pressurization and blowdown of the melt generator. One was placed in a machined recess in the top flange cover, protected by steel metal turnings. The second was inserted in a tee fitting in the gas line near to the melt generator. The latter was intended as a backup device in a location well away from the hot environment of the space above the melt pool.

Two pressure gauges (Kulite XT-190) were used to monitor the gas pressure in the tunnel region of the cavity. Both were installed on a common toe fitting connected to a short section of 9.5-mm diameter steel tubing that penetrated the cavity wall midway along the tunnel length. A small amount of steel turnings was placed in the tube to mitigate the migration of debris particles to the sensing face of the gauges. An analysis of the influence of the tube on the response of the gauges is discussed in (Tarbell et al., 1987A).

The possible pressure increase caused by debris into the chamber atmosphere was monitored by two gauges (Kulite XT-190). One gauge was placed at the midpoint of the west chamber wall while the second was located at the center of the chamber door away from the apparatus. Both gauges were installed in drilled and tapped holes in the 7.9-mm thick chamber wall. No protection of the gauge sensing elements was attempted.

The two-color pyrometer (Ircon Model 35G10) was the same device as used in the HIPS-7C experiment (Section 3.2). For this test, the device was located outside the chamber and aimed at the debris emerging from the cavity exit. The line of sight was from the east to the west at a distance of approximately 2 m from the cavity. The spot size at the cavity exit was nominally 2 cm diameter.

Thermocouples were used to measure gas temperature inside the melt generator and the chamber. The melt generator device was a Type-K with a 3.2 mm diameter steel sheath. The sensor was inserted through the top flange cover to a depth of about 46 cm into the melt generator. Two Type-K thermocouples, 0.5 mm in diameter, were installed adjacent to the chamber pressure gauges. The small diameter was selected to improve the response time of the device relative to the larger devices previously used. Each thermocouple penetrated into the chamber approximately 8 cm to avoid possible boundary layer effects near the wall surface.

A phototransistor (Motorola Type MRD310) was placed under the fusible plug to provide an accurate timing reference to the start of melt ejection. The output of the device was also used to trigger a strobe lamp unit that allowed synchronization of the electrical and film records.

Table 4.1

Summary of HIPS-8C Instrumentation

Device Type	No.	Range	Location	Purpose
Pressure	1	0-6.9 MPa	Melt Gen	Melt Generator Blowdown
Pressure	1	0-6.9 MPa	Gas Line	Reference
Pressure	1	0-3.4 MPa	Cavity	Cavity Pressure
Pressure	1	0-0.7 MPa	Cavity	Cavity Pressure
Pressure	2	0-0.4 MPa	Int Chamber	Atm Heating
Pyrometer	1	1500-3500R C	Cavity Exit	Debris Temperature
TC	1	0-1500R C	Melt Gen	Gas Temperature
TC	2	0-1500R C	Int Chamb Walls	Atm Temperature
Photo Det	1	--	Fusible Plug	Timing
Filters	10	--	Chamber	Aerosol Mass Concentration
Cameras	10	--	--	Observation
Real Time X-Ray	1	2000 fps[a]	Cavity Exit	Debris Character

[a] Frames per second

The X-ray imaging device was employed to view the debris emerging from the cavity and impacting onto the Plexiglass deflection shield. The advantage of X-ray over normal optical observation is that aerosol and illumination do not hamper the view of the debris. The X-ray source was provided by a Norelco Model CK-150 that produced a continuous stream of 150 keV photons. The imaging device (Precise Optics P600) converted the incident photons to electrons that were then focused on an internal fluorescent screen. The screen image was detected by a high-speed digitizing video camera (SPIN-Physics Model 2000 camera and recorder). This system permitted a full-screen image to be recorded at framing rates of up to 2000 fps.

The image intensifier was placed along side the Plexiglass deflection plate so that plane of the shield was across the face of the detector. The distance from the center line of the Plexiglass as the face of the image intensifier was approximately 60 cm. The X-ray head was mounted on a tripod directly opposite the image intensifier so that photons emitted from the center of the source would be parallel to the surface of the Plexiglass. This technique eliminated distortion that would be caused by non-normal incident X-rays. Locating the X-ray approximately 2 m from the object gave a geometric expansion factor of 1.3 for the image at the center of the Plexiglass. For a framing rate of 2000 fps, the recorder could operate for a total time of 45 s.

The cameras employed to give a visual record of the test are summarized in Table 4.2 Most of the units were Hycam's (Redlake Corp.), operating at either 100 or 400 fps. The two Hulcher cameras use 70-mm film to give high quality still pictures. The framing rates of these devices (10 and 20 fps) were inadequate to provide fine resolution of the events during the experiment.

4.3 Initial Conditions

The initial conditions for the HIPS-8C test are summarized in Table 4.3. The gas volume, pressure, and temperature are values at the onset of melt ejection. The thermocouple, intended to measure the gas temperature in the melt generator, was adversely affected during the thermite reaction. The temperature value reported in Table 4.3 was estimated from the measured pressure rise, estimated volume change (of melt), and the estimated increase in gas mass (from HIPS-3J) during the thermite burn.

4.4 Experiment Results and Analysis

This section presents the results obtained from the HIPS-8C experiment. Analysis of the test is also presented where appropriate to aid in the understanding and interpreting of the experiment observations.

Table 4.2

Summary of HIPS-8C Camera Coverage

Device	Start Time(a) (s)	Speed[b] (fps)	Field of View
Camera	-5	100	100' Overall from East
Camera	+5	400	30' Normal to Cavity Exit
Camera	+5	400	30' Parallel to Cavity Exit
Camera	+5	400	Chamber Top Viewport
Camera	+5	400	Chamber Side Viewport
Camera	+5	400	Chamber Rear Viewport
Camera	+5	400	Deflection Shield
Camera	+5	400	Deflection Shield
Hulcher	+15	20	100' Normal to Cavity Exit
Hulcher	+15	10	100' Parallel to Cavity
Video	--	30	

[a] Relative to ignition of thermite powder.

[b] Frames per second.

Table 4.3

HIPS-8C Initial Conditions

Melt Mass	80 kg	
Thermite Composition	Iron Oxide (Fe_3O_r) Aluminum (Al)	61.04 kg 18.96 kg
Melt Composition	Iron (Fe) + Alumina (Al_2O_3)	
Gas	Carbon Dioxide (CO_2)	
Gas Volume	0.118 m^3	
Initial Pressure	3.5 MPa	
Ambient Temperature	525 K	
Melt Plug Diameter	0.0355 m	

4.4.1 Camera Coverage

Melt dispersal from the HIPS-8C cavity is partitioned into two streams. One stream emanates from the normal cavity exit, which discharges into the desert outside the interaction chamber. Figure 4.3 shows this stream before and after it is redirected by the deflection shield. The sequence of events is similar to that reported in other tests (Tarbell et al., 1986): particles are launched great distances into the desert with the now expected aerosol generation accompanying the process.

The second stream of dispersed material leaves the cavity through the annular gap where it is confined within the interaction chamber. The sequence shown in Figure 4.4 shows the dispersal process through the annular gap. In the first three frames, there is an ordered venting of luminous gas with the visual intensity increasing as more melt is injected into the cavity. There is no evidence that deflected or splashed melt is leaving the cavity through the gap. The last frame depicts the process after the melt generator starts discharging gas into the cavity. The process suddenly becomes chaotic with melt particles being swept through the gap. Failure to plug thermocouple holes in the cavity model (used in a previous test) results in two jets of gas and melt that can be seen in the lower right hand corner of each frame.

4.4.2 Pressurization and Blowdown History of the Melt Generator

Figure 4.5 summarizes the pressurization history of the melt generator. The start of melt discharge is taken as the reference time. Gradual charging of the melt generator with CO_2 gas begins at -275 s. Prior to ignition of the thermite at -20 s, the melt generator is isolated from the gas source. The burn time is 20 s.

Figure 4.6 shows an expanded version of the depressurization history of the melt generator following the onset of melt ejection. Also shown are model predictions (Pilch & Tarbell, 1985) for the same period. Two phases can be distinguished. The first phase lasting about 350 ms, corresponds to liquid phase discharge during which the pressure decreases because the free volume is increasing as melt is expelled from the generator. Despite the lower pressures in this test, this phase is shorter than that reported for the HIPS-3J and HIPS-7C tests because the initial diameter of the discharge orifice is nearly twice as large in this test. The onset of gas flow out the orifice marks the beginning of the second phase. Gas discharge is accompanied by continued, but reduced, discharge of melt (Pilch & Tarbell, 1985). The second phase lasts 1-1.5 s at which time the blowdown of the generator is complete.

Figure 4.7 shows that the peak temperature recorded by the two color pyrometer was 2200 K, which is well below the

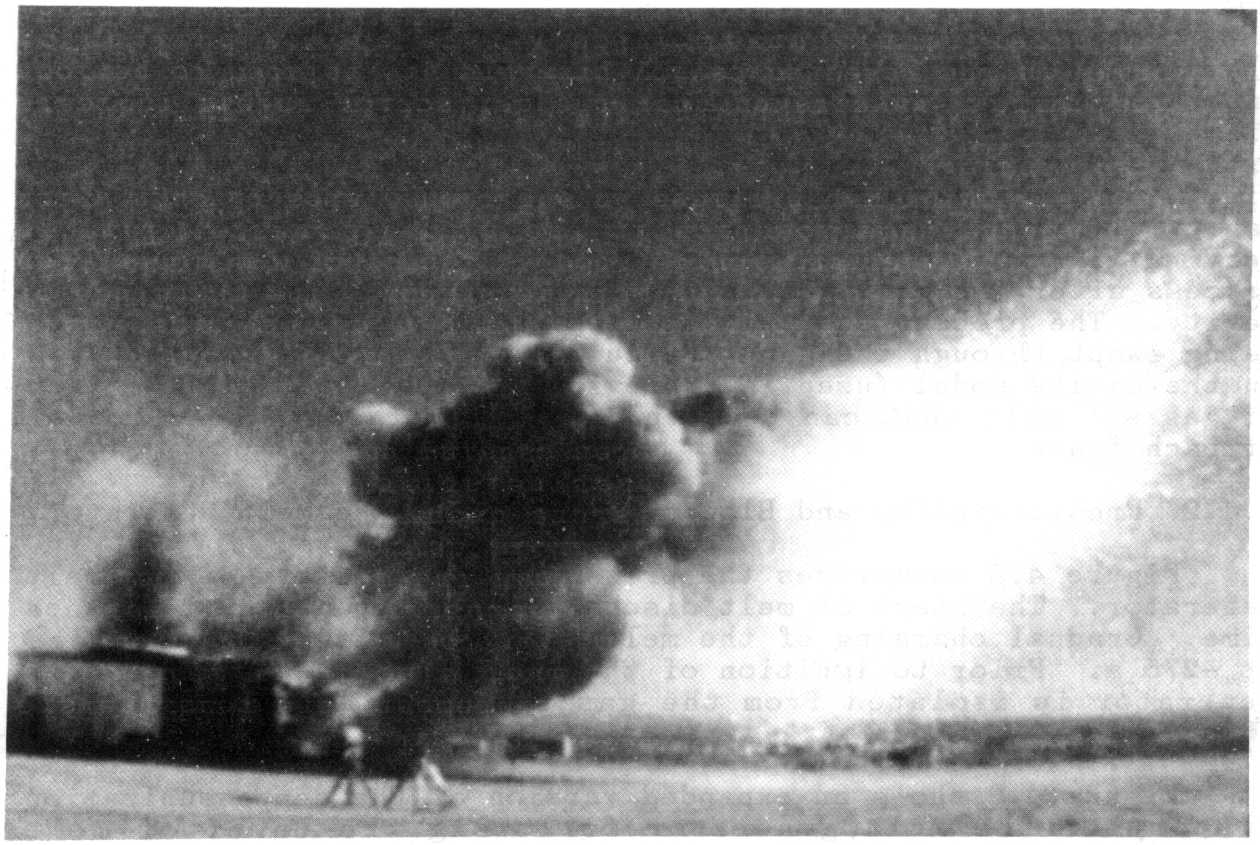

Figure 4.3: Debris Dispersal Through the Normal Cavity Exit

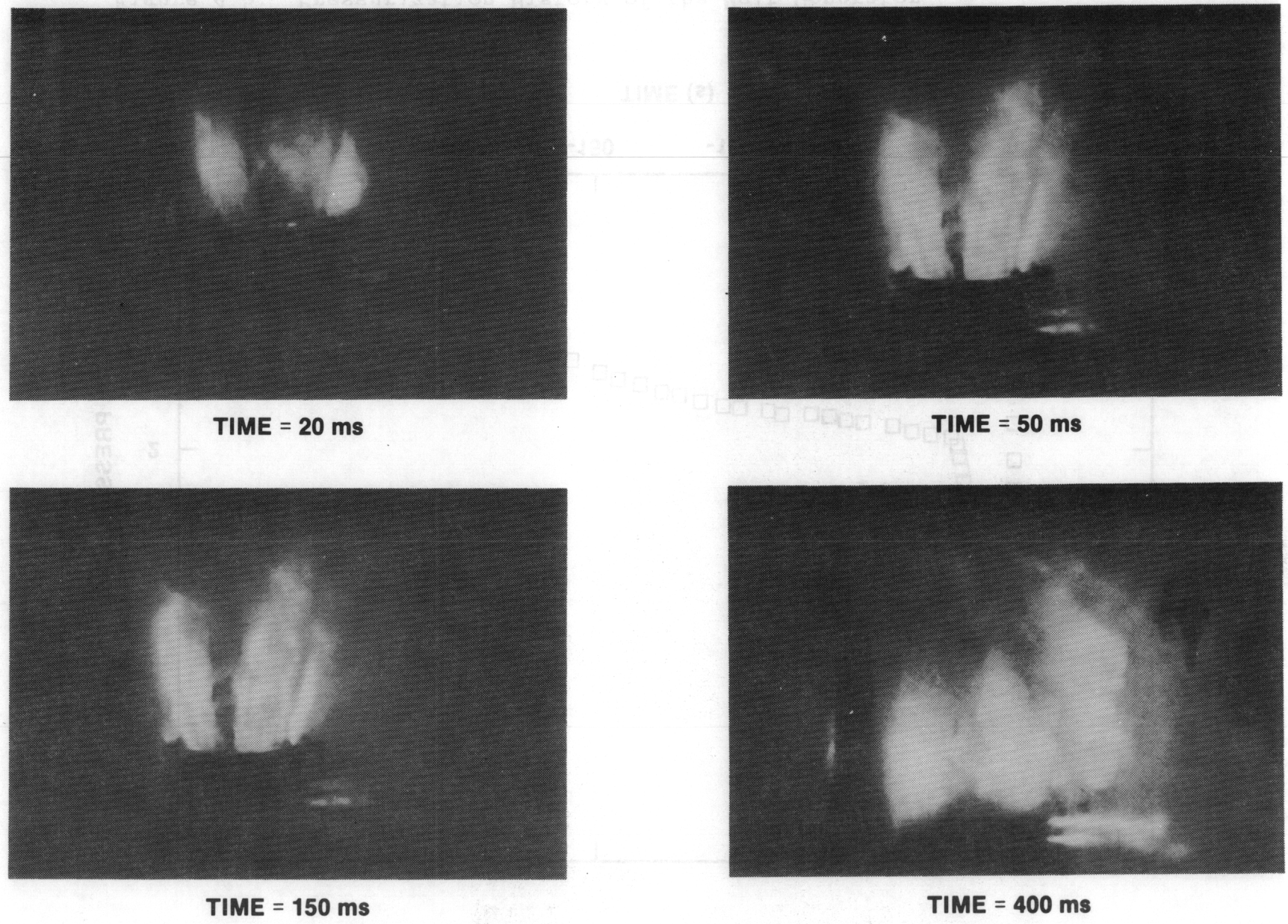

Figure 4.4: Debris Dispersal Through the Annular Gap

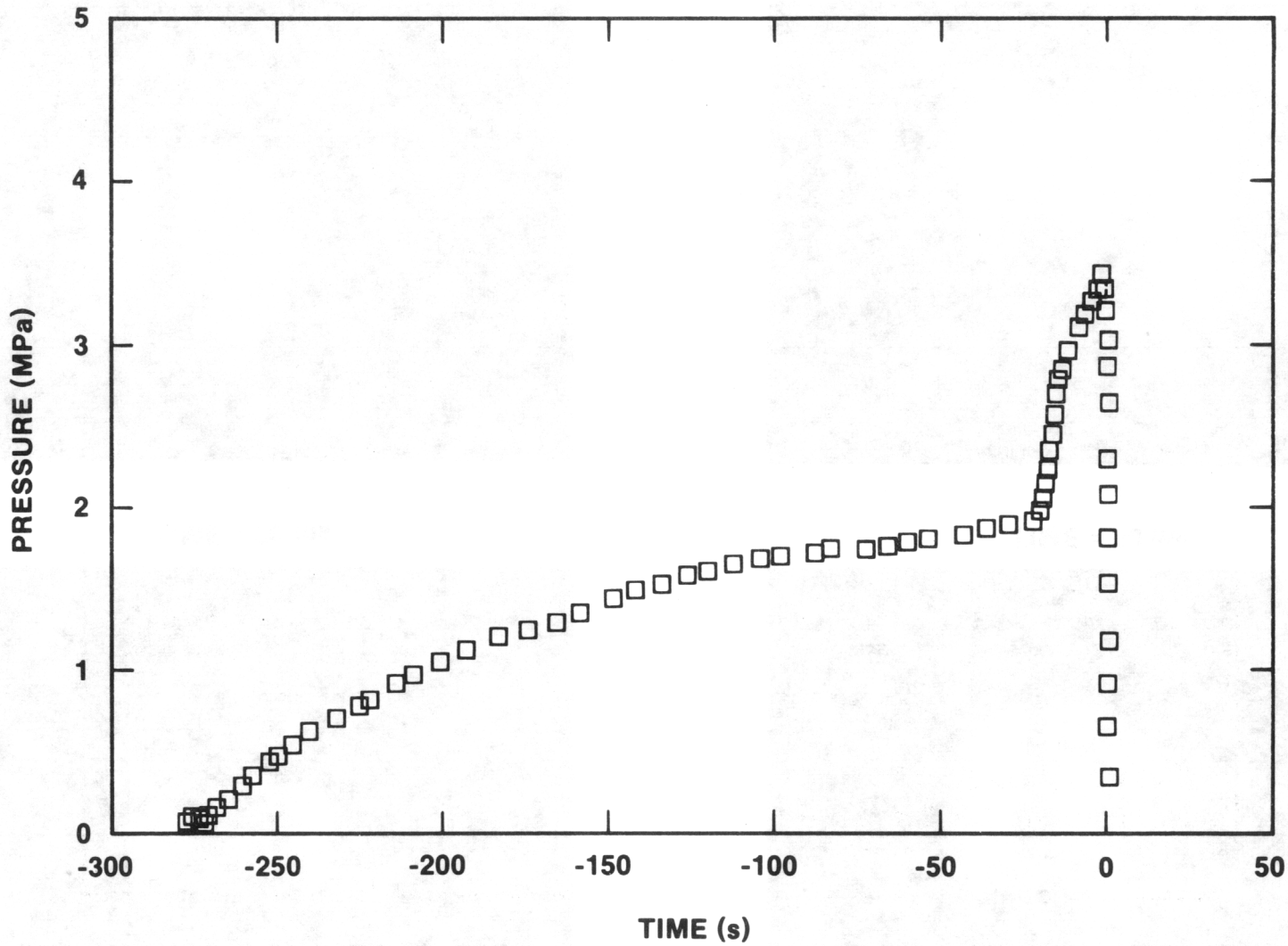

Figure 4.5: Pressurization History of the Melt Generator

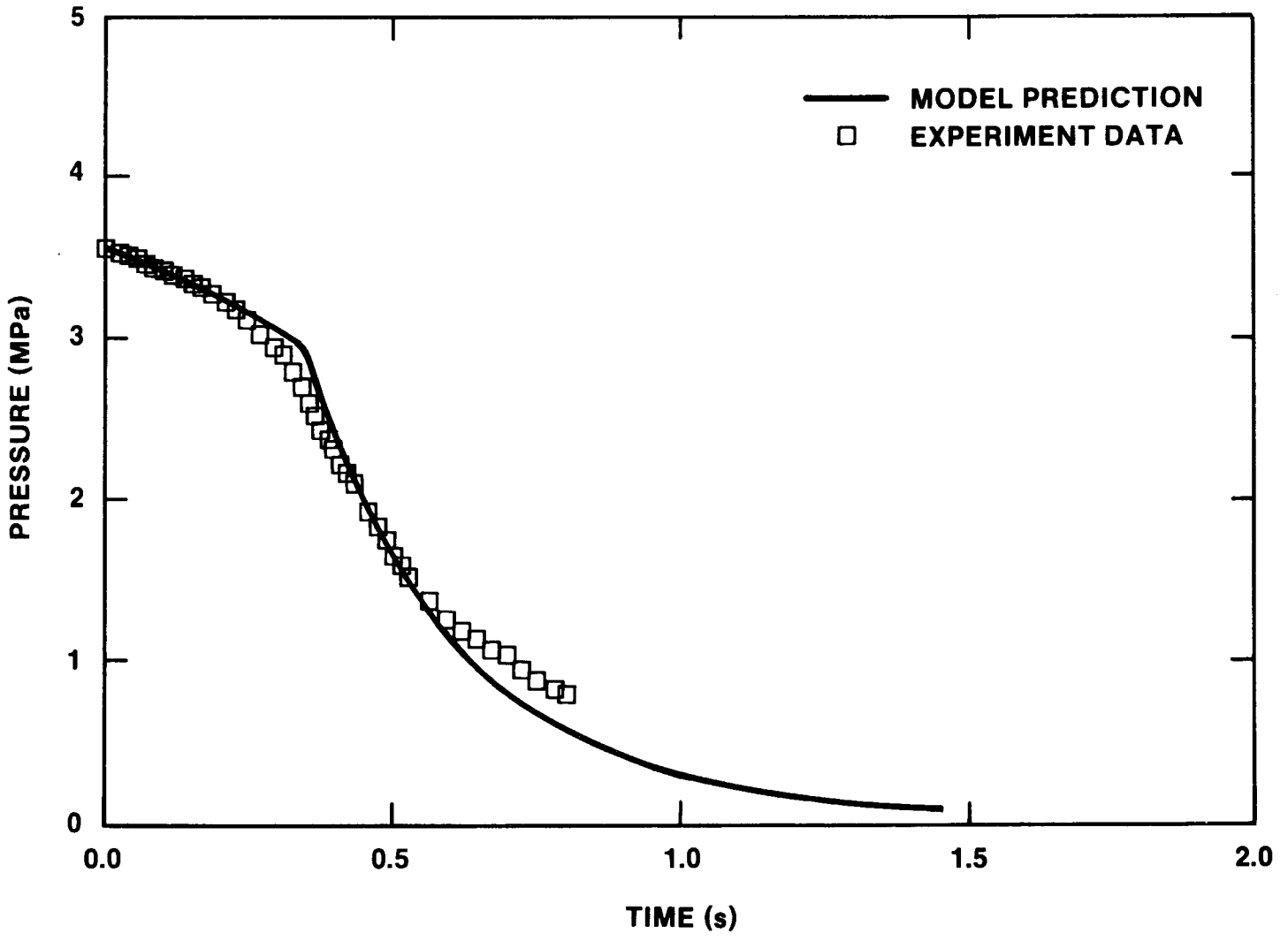

Figure 4.6: Blowdown History of the Melt Generator

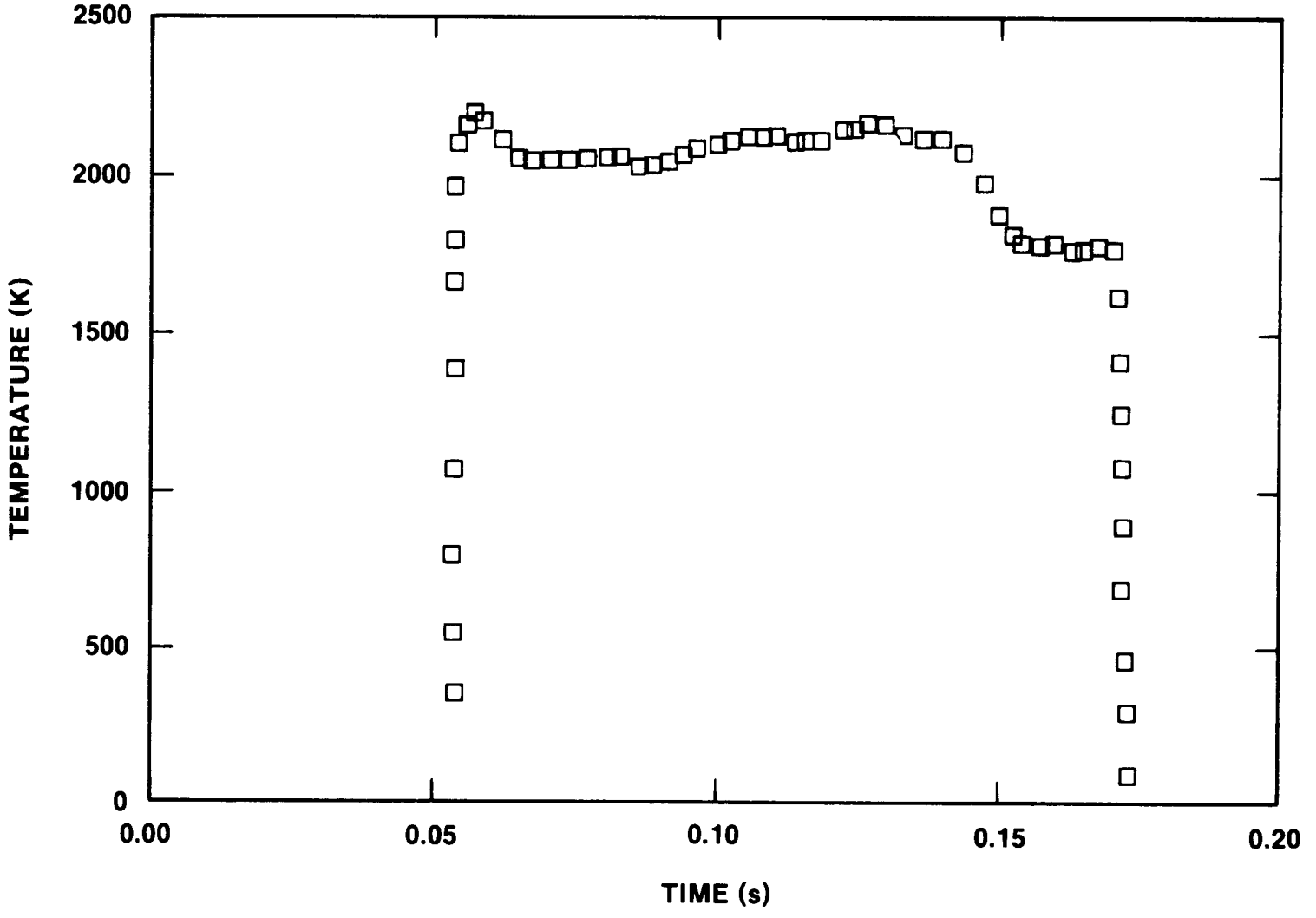

Figure 4.7: Temperature Measurement Outside the Cavity Using a 2-Color Pyrometer

theoretical value of 3200 K for a complete and adiabatic reaction. The measured temperatures are well above the freezing point (1700 K) and well below the boiling point (3200 K) of the iron phase of the melt. The measured peak temperature is essentially at the freezing point (2300 K) for the alumina phase of the melt.

Figure 4.7 shows that the initial temperature readings are delayed 0.05 s after the start of melt ejection. This delay represents the expected transit time for the melt to pass through the cavity. The pyrometer output abruptly drops to zero at 0.17 s, which is significantly less than the melt ejection time. The two-color pyrometer is a threshold device that provides a negative output when the temperature drops below 1500 C. For this test, it is speculated that relatively cold aerosols shielded the melt from the pyrometer causing the output to vanish at 0.17 s.

Figure 4.8 shows pressure measurements made at the cavity sidewall. The measured pressures in the cavity are small compared to the pressure in the melt generator. The magnitude of the cavity overpressurization is about a factor of two lower than observed at the same location in the HIPS-7C test.. This is because the annular gap provides an additional area through which gases can vent.

Real time X-rays taken near the deflection shield indicate that peaks in the measured cavity pressure are related to periods of high material dispersal. The X-rays show a buildup of dispersed material followed by a relatively quiescent period. The quiescent period is seen to occur in the X-ray film at approximately 0.3 s, which corresponds closely with a minimum in the cavity pressure. The quiescent period occurs before the onset of gas discharge into the cavity.

Gas discharge begins at about 0.35 s (Figure 4.6), which corresponds to the beginning of the second peak in the cavity pressure curve. The real time X-rays confirm that this marks the beginning of a more vigorous period of melt dispersal. The X-rays also reveal that dispersal from the cavity ceases abruptly at about 0.6 s, which corresponds to the end of the third peak in the cavity pressure curve. Thus, dispersal ends approximately 0.25 s after the onset of gas discharge into the cavity.

4.4.3 Structure Interactions

The extent of debris dispersed from the cavity through the annular gap is important in determining the potential direct heating of the containment atmosphere. In order to extrapolate the experimental results to a realistic scale, the mechanisms of debris dispersal through the gap must be identified. It is assumed that debris may be driven or carried out of the reactor cavity via the annular gap around the RPV by one or more distinct

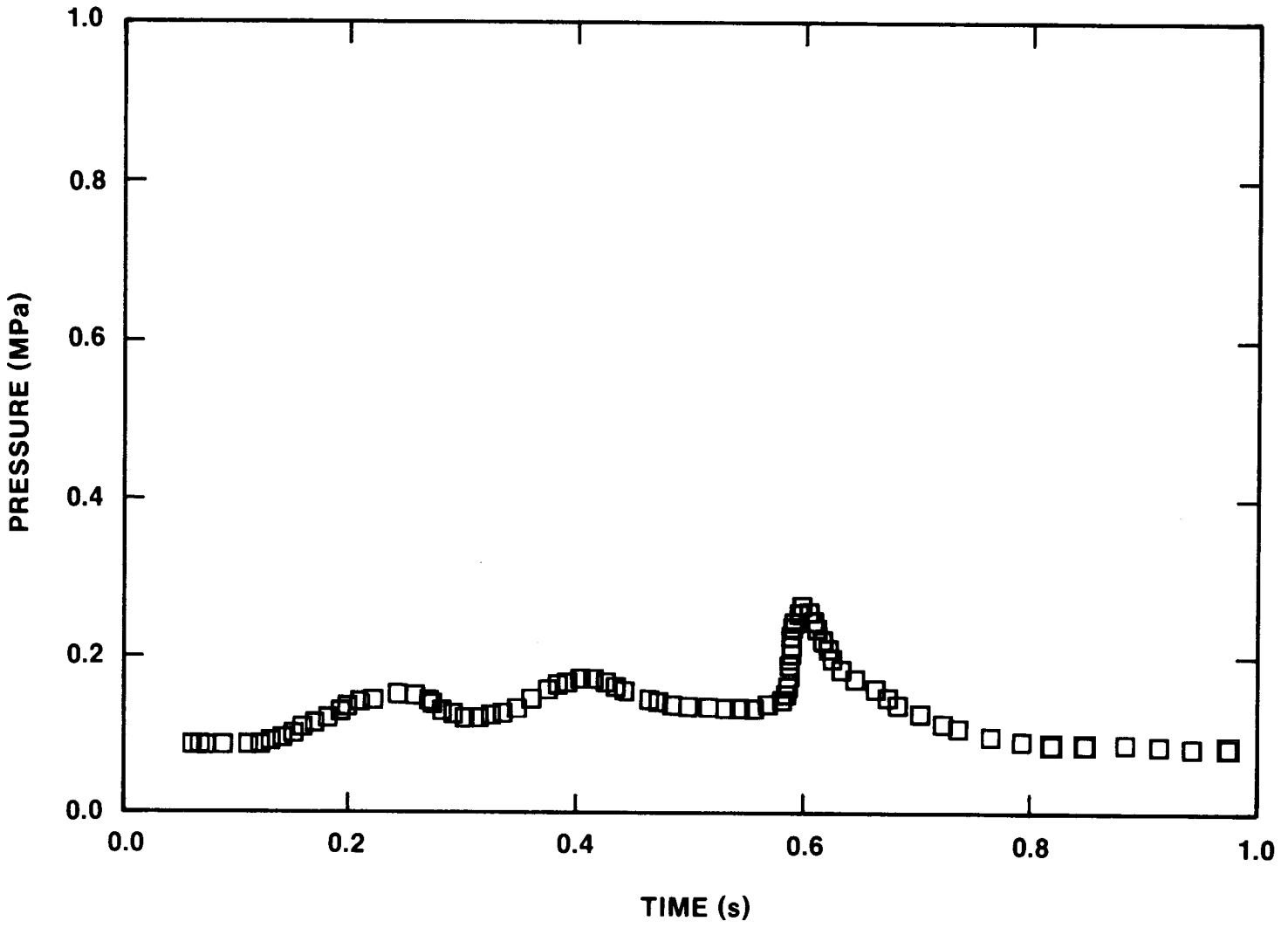

Figure 4.8: Pressure Measurements in the Cavity

mechanisms; splashout, jet deflection, or entrainment. Splashout can occur if the debris entering the cavity forms a hydraulic jump of sufficient height to allow material to enter the gap region. It is unlikely that this will be the dominant mechanism because the vertical dimensions of most reactor cavities are significantly greater than the predicted jump height. For example, the Zion cavity is more than twice as high as the calculated height of the hydraulic jump.

Jet deflection occurs when the ejected debris impacts the cavity floor and deflects upward along the cavity walls towards the RPV. The height attained by the deflected material is dependent on its initial velocity and the amount of energy lost during interactions with the floor and walls of the cavity. For the accident conditions depicted by the HIPS-8C experiment, the debris could reach a height on the order of 50 meters.

Melt entrained and removed via the annular gap occurs by the same mechanism attributed to debris dispersal from the normal cavity exit. The high-velocity gas from the RPV during primary system blowdown will divide between the gap and the tunnel according to the flow patterns established by the geometry of the cavity. Linear scaling of the cavity dimensions maintains the correct relationship between the flow areas and should preserve the flow patterns.

Determining the mechanism responsible for debris removal through the annular gap can be inferred by observing the nature and timing of the dispersal. For example, both splashout and jet deflection will occur soon after the start of ejection, and will be in the form of a film or sheet of material. Figure 4.4 shows that this was not observed. Particle entrainment depends on the flow of gas out of the vessel and will occur later in the sequence of events. This was the observed mechanism of dispersal. In the HIPS-8C experiment, the onset of gas discharge begins nominally 200-300 ms after the start of the ejection cycle. Observing when material begins to exit the gap and its form will identify the predominant removal mechanisms.

The debris retained by the interaction chamber was collected after the experiment to determine the amount of material discharged through the annular gap. Aluminum collection pans were placed on the floor of the enclosure in an attempt to resolve the distribution of the debris with respect to the apparatus. Aluminum proved to be a poor selection for this purpose because many of the pans were severely damaged by the deposited debris. Approximately 20 kg of debris material was collected in this manner with a small contribution due to the melted aluminum adhered to the debris.

A portion of the extension tube connecting the melt generator with the cavity (Figure 4.1) was eroded during the discharge process. Approximately 14 kg of the melt was trapped within the hollow portion of the transition piece. An additional 4 kg of debris was recovered from the melt generator and cavity. Of the 62 kg actually dispersed from the cavity, 20 kg (32%) was actually dispersed through the annular gap.

Figure 4.1 depicts the geometry of the cavity. There are two paths by which melt can escape the cylindrical region under the melt generator; the annular gap, and the tunnel leading to the normal exit from the cavity. The flow area into the tunnel (for the test) is 0.0955 m^2; and the gap flow area is 0.0209 m^2, which represents 18% of the total area leading to escape from the cavity. In comparison, the test revealed that 32% of the melt escaped the cavity through the gap, thus indicating a preferential dispersal out the gap.

Preferential dispersal out the gap is expected given the flow patterns of melt and gas in the region beneath the vessel. Melt and gas striking the floor spreads radially until it is deflected vertically along the cylindrical portion of the cavity. This deflected melt is inline with the annular gap and its flight path is not easily influenced by further changes in gas direction that might occur under the vessel.

Only that portion of the radially flowing melt (along the cavity floor) that is aimed at the tunnel is immune from potential dispersal out through the gap. Thus, the geometry places an upper limit of about 79% that potentially can be dispersed through the gap. The observed value lies closer to the flow area ratio.

5. SUMMARY AND CONCLUSIONS

The experiments discussed in this report are not intended to directly simulate HPME accidents. They are intended to provide insight into relevant processes and to support development of phenomenological models which in turn are incorporated into the system level codes, such as MELPROG and CONTAIN. Realistic assessments of reactor accidents are obtained through integrated analysis using these system level codes.

The results of the HIPS-3J and HIPS-7C experiments suggest that melt retention by freezing on structures may be only a small fraction of the melt actually striking the structure. Freezing of melt on concrete structures is not an efficient retention mechanism. Melt does not stick to concrete due to degradation and outgassing of the surface. Melt does freeze on steel structures. Retention of melt on steel surfaces is limited by the flux of melt striking the surface or the freezing flux based on conduction freezing, whichever is the smaller. The quantity of melt striking the surface is much in excess of the freezing flux; it will splash or drip from the surface and continue to contribute to DCH.

The excavity structure in the HIPS-7C experiment retained only 4% of the melt dispersed from the cavity. The remaining melt splashed or was otherwise reentrained from the structure. Much of this material was directed upwards along the roof of the chamber. Analysis suggests that even less material would be trapped at reactor scale because more debris can be deflected directly by the gas stream.

Preferential dispersal through the annular gap was observed in the HIPS-8C experiment, where 32% of the melt escaped the cavity through the gap. Geometry places an upper limit of 79% on this value while the gap-to-total flow area ratio of 18% represents a lower limit to the possible amount dispersed through the gap. Additional two-phase flow modeling, accounting for gas flow patterns and melt distribution, is required in order to predict the actual quantity of melt that may be dispersed through the annular gap in other geometries or at reactor scales.

The dispersal time is approximately 600 ms for these tests. Real time X-rays of the dispersal process correlate well with pressure measurements in the cavity. The observed dispersal times can be used to verify dispersal rate models that may be developed in the future. Pressure measurements in the cavity may be used in future tests to infer dispersal time.

Pyrometer measurements of the melt consistently yielded temperatures that were at the freezing point of the alumina phase of the melt. This probably represents the surface temperature of a thin crust surrounding a molten core and may not be indicative of the bulk temperature of the drop because of the very fluid

behavior of the melt at locations beyond the measurement location. The surface temperature, however, is the driving potential for the vaporization processes leading to aerosol production.

Copius quantities of aerosols were observed in all tests. The fraction of dispersed debris that is in the form of aerosols (dia<10 μm) is approximately 1-5%, and appears to increase with melt mass and/or interactions with structures. The mechanisms leading to aerosol production in the tests are believed to be operable at reactor scale, but the quantity of aerosol may be different in the reactor case because the melt composition is different. Predictions of aerosol production in reactor accidents await a comprehensive model that incorporates all the relevant phenomena.

These experiments demonstrate that selected containment structures may not decisively mitigate the dispersal and transport of debris throughout the containment. Dispersal can occur through multiple paths if available. Clearly, structure interactions alter the direction and character of melt while multiple interactions with structures can actually promote mixing of melt with itself and with the atmosphere.

Melt does not easily follow changes in gas direction and multiple impacts with structures are assured for most of the melt during the dispersal and transport phases. Structure interactions are characterized by skidding, splashing, and freezing. However, melt interactions with structures do not imply retention.

Models already developed for high pressure melt ejection, gas blowdown, and hole ablation are verified by the experiments. Models characterizing the impact of high velocity melt with surfaces are required and currently under development. Results reported herein show that such models must account for not only retention of melt by interactions with plant structures but also must deal with further break up at the melt stream as it splashes and fragments from these interactions. Additional models describing the dispersal rate and aerosol production rates are also required.

6. REFERENCES

Bergeron, K. D. et al., User's Manual for CONTAIN 1.0. A Computer Code for Severe Nuclear Reactor Accident Containment Analysis, Sandia National Laboratories, Albuquerque, NM, NUREG/CR-4085, SAND84-1204, May 1985.

Brockmann, J. E. and Tarbell, W. W., "Aerosol Generation by Pressurized Melt Ejection," Aerosols: Science, Technology, and Industrial Applications of Airborne Particles, Elsevier, Proceedings of the First International Aerosol Conference, Minneapolis, Minnesota, USA, 489-492, (Sept. 17-21, 1984).

Brockmann, J. E. and Tarbell, W. W., "Aerosol Source Term in High Pressure Melt Ejection," Nuclear Science and Engineering, 88 342-356, 1984.

Butland, A. T. D. et al., Report on Phase 1 of the PWR Severe Accident Containment Study, United Kingdom Atomic Energy Authority, AEEW-R1842, December 1984.

Camp, W. J. et al., MELPROG-PWR/MODO: A Mechanistic Code for Analysis of Reactor Core Melt Progression and Vessel Attack Under Severe Accident Conditions, Sandia National Laboratories, Albuquerque, NM, NUREG/CR-4909, SAND85-0237, April 1987.

Carslaw, H. S. and Jaegar, J. C. Conduction of Heat in Solids, Oxford Press, 2nd Edition, 1959.

Cook, I., Contribution to: Reactor Safety Research Semiannual Report, July-December 1987, Sandia National Laboratories, Albuquerque, NM, NUREG/CR-5039 (2 of 2), SAND87-2411 (2 of 2), Vol 38, to be published.

COMED, Zion Probabilistic Safety Study, Commonwealth Edison Co., Chicago, IL, 1981.

CONED, Indian Point Probabilistic Safety Study, Power Authority of the State of New York, Consolidated Edison Company of New York, Inc., Buffalo, NY, 1982.

Dallman, J. C. and Kirchner, W. L., De-entrainment Phenomena of Vertical Tubes in Droplet Cross Flow, NUREG/CR-1421, LA-8316-MS, Apr. 1980.

Denny, V. E. and Sehgal, B. R., "Analytical Prediction of Core Heatup/Liquefaction/Slumping," Paper 5.4, Proceedings of the International Meeting on Light-Water Reactor Severe Accident Evaluation, Cambridge, MA, August 1983.

Fauske & Associates, Inc., Technical Support for Issue Resolution, Technical Report 85.2 Industry Degraded Core Rulemaking Program Report, July 1985.

IDCOR, Nuclear Power Plant Response to Severe Accidents IDCOR Technical Summary Report, Technology for Energy Corp., Knoxville, TN, November 1984.

Pilch, M. and Tarbell, W. W., High Pressure Ejection of Melt from a Reactor Vessel - The Discharge Phase, Sandia National Laboratories, Albuquerque, NM, NUREG/CR-4383, SAND85-0012, September 1985.

Spencer, B. W., Sienicki, J. J., and McUmber, L. J., Hydrodynamics and Heat Transfer Aspects of Corium-Water Interactions, EPRI NP-5127, March 1987.

Spencer, B. W. et al., Sweepout Thresholds in Reactor Cavity Interactions, ANL/LWR/SAF 82-1, April 1982.

Squarer, D., "The Impact of Heat-Generating Debris on Containment Loading - An Overview," Preliminary Proceedings of Sixth Information Exchange Meeting on Debris Coolability, UCLA, Los Angeles, CA, November 7-9, 1984.

Tarbell, W. W., Brockmann, J. E., and Pilch, M., "High Pressure Melt Ejection," NUREG/CP-0048, Vol. 3, Proceedings of the Eleventh Water Reactor Safety Research Information Meeting, Gaithersburg, MD, 204-217, (Oct. 24-28, 1983).

Tarbell, W. W., Brockmann, J. E., and Pilch, M., High-Pressure Melt Streaming (HIPS) Program Plan, Sandia National Laboratories, Albuquerque, NM, NUREG/CR-3025, SAND82-2477, August 1984.

Tarbell, W. W. et al., Pressurized Melt Ejection Into Water Beds, Sandia National Laboratories, Albuquerque, NM, NUREG/CR-3916, SAND84-1531 (to be published).

Tarbell, W. W. et al., Initial Test Results: SPIT-19, Sandia National Laboratories Memorandum, April 1984.

Tarbell, W. W. et al., Pressurized Melt Ejection into Scaled Reactor Cavities, Sandia National Laboratories, Albuquerque, NM, NUREG/CR-4512, SAND86-0153, October 1986.

Tarbell, W. W. et al., Results from the DCH-1 Experiment, Sandia National Laboratories, Albuquerque, NM, NUREG/CR-4871, SAND86-2483, June 1987.

Touloukian Ed., Thermophysical Properties of High Temperature Solid Material, MacMillan, 1967.

Tutu, N. K. et al., Debris Dispersal from Reactor Cavities During High Pressure Melt Ejection Scenarios (to be published).

USNRC, Reactor Safety Study, An Assessment of Accident Risks in U.S. Commercial Nuclear Power Plants, WASH-1400, USNRC, Washington, DC, NUREG/75-014, October 1975.

WEC, Sizewell-B Probabilistic Safety Study, Westinghouse Electric Corporation, Pittsburgh, PA, WCAP-991, 1982.

Wheeler, C. L., and Thurgood, M. J., "COBRA-NC Application to Containment Analysis," NUREG/CP-0058, Vol. 3, Proceedings of the Twelfth Water Reactor Safety Research Information Meeting, Gaithersburg, MD, 445-459, (Oct. 22-26, 1983).

Williams, D. C., "Impact of Chemical Phenomena in Direct Containment Heating," SAND86-2020C, Presented at American Chemical Society Severe Accident Symposium, Anaheim, CA, September 8-12, 1986.

Distribution:

U.S. Nuclear Regulatory Commission (25)
Office of Nuclear Regulatory Research
Washington, DC 20555
Attn: E. S. Beckjord
D. F. Ross
T. P. Speis
C. N. Kelber
M. Silberberg
G. Marino
L. Chan
C. Ryder
R. W. Wright
T. Walker
R. O. Meyer
J. A. Mitchell
S. B. Burson
T. Lee (5)
M. Cunningham
J. Murphy
P. Wood
F. Eltawilla
L. G. Hulman
B. Hardin
Z. Rosztoczy

U.S. Nuclear Regulatory Commission (3)
Office of Nuclear Regulatory Regulation
Washington, DC 20555
Attn: R. Barrett
S. Long
W. Lyon

U.S. Department of Energy (2)
Albuquerque Operations Office
P.O. Box 5400
Albuquerque, NM 87185
Attn: J. R. Roeder, Director
J. A. Morley, Director
For: C. B. Quinn
R. N. Holton

U.S. Department of Energy
Office of Nuclear Safety Coordination
Washington, DC 20545
Attn: R. W. Barber

Electric Power Research Institute (4)
3412 Hillview Avenue
Palo Alto, CA 94303
Attn: R. Vogel
R. Ritzman
W. Lowonstein
R. Sehgal

Brookhaven National Laboratory (5)
Upton, NY 11973
Attn: R. A. Bari
T. Pratt
N. Tutu
G. Greene
T. Ginsberg

Professor R. Seale
Department of Nuclear Engineering
University of Arizona
Tucson, AZ 85721

Oak Ridge National Laboratory
P.O. Box Y
Oak Ridge, TN 37830
Attn: T. Kress

K. Holtzclaw
General Electric - San Jose
Mail Code 682
175 Kurtner Avenue
San Jose, CA 95125

Argonne National Laboratory (5)
9700 South Cass Avenue
Argonne, IL 60439
Attn: J. Rest
C. Johnson
L. Baker, Jr.
D. Cho
B. Spencer

Cathy Anderson
Nuclear Safety Oversight Commission
1133 15th St., NW
Room 307
Washington, DC 20005

Battelle Columbus Laboratory (3)
505 King Avenue
Columbus, OH 43201
Attn: P. Cybulskis
R. Denning
J. Gieseke

J. E. Antill
Berkeley Nuclear Laboratory
Berkeley GL 139 PB
Gloucestershire
ENGLAND, U.K.

W. G. Cunliffe
Bldg. 396
British Nuclear Fuels, Ltd.
Springfields Works
Salwick, Preston
Lancashire
ENGLAND, U.K.

R. Deem
Power Authority State of NY
10 Columbus Circle
New York, NY 10019

Professor Agustin Alonso
E.T.S. Ingenieros Industriales
Jose Gutierrez Abascal, 2
28006 Madrid, SPAIN

Dr. Alfonso Perez
Department de Seguridad Nuclear
Junta de Energia Nuclear
Avenida Complutense, 22
Madrid - 3, SPAIN

R. Sherry
JAYCOR
P.O. Box 85154
San Diego, CA 92138

Ktech Corp. (5)
901 Pennsylvania NE
Albuquerque, NM 87110
Attn: R. E. Blose
R. T. Nichols
M. S. Oliver
J. Jackson
J. W. Ross

Los Alamos National Laboratories
P.O. Box 1663
Los Alamos, NM 87545
Attn: M. Stevenson

UCLA (2)
Nuclear Energy Laboratory
405 Hilgaard Avenue
Los Angeles, CA 90024
Attn: I. Catton
D. Okrent

University of Wisconsin
Nuclear Engineering Department
1500 Johnson Drive
Madison, WI 53706
Attn: M. L. Corradini

EG&G Idaho
Willow Creek Building, W-3
P.O. Box 1625
Idaho Falls, ID 83415
Attn: R. Hobbins

Battelle Pacific Northwest Laboratory
P.O. Box 999
Richland, WA 99352
Attn: M. Freshley

Wiktor Frid
Swedish State Power Board
S-162 FACH 87 VALLINGBY
SWEDEN

W. Stratton
2 Acoma Lane
Los Alamos, NM 87544

Gesellschaft fur Reaktorsicherheit (GRS)
Postfach 101650
Glockengrasse 2
5000 Koeln 1
Federal Republic of GERMANY

Kraftwerk Union
Hammerbacher Strasse 1214
Postfach 3220
D-8520 Erlangen 2
Federal Republic of GERMANY
Attn: Dr. M. Peehs

UKAEA
Reactor Development Division (5)
Winfrith, Dorchester
Dorset DT2 8DH
ENGLAND, U.K.
Attn: R. Potter
A. Nichols
B. Bowsher
P. Smith
T. Butland

Nucleare e della Protezione Sanitaria (DISP) (2)
Ente Nazionnle Energie Alternative (ENEA)
Viale Regina Margherita, 125
Casella Postale M. 2358
I-00100 Roma A.D., ITALY
Attn: Mr. Manilia
Mr. G. Petrangeli

Dr. K. J. Brinkman
Reactor Centrum Nederland
1755 ZG Petten
THE NETHERLANDS

Dr. S. J. Niemczyk
1545 18th Street, NW
#112
Washington, DC 20036

Kernforschungszentrum Karlsruhe
Postfach 3640
75 Karlsruhe
Federal Republic of GERMANY
Attn: H. Rininsland

Mr. H. Bairiot, Chief
Department LWR Fuel
Belgonucleaire
Rue de Champde Mars. 25
B-1050 Brussels, BELGIUM

Japan Atomic Energy Research Institute
Tokai-Mura, Naka-Gun
Ibaraki-Ken 319-11
JAPAN
Attn: S. Saito

Wang Lu
TVA
400 Commerce, W9C157-CK
Knoxville, TN 37902

M. Fontana
Director, IDCOR Program
ENERGEX
575 Oak Ridge Turnpike
Oak Ridge, TN 37830

Fauske and Associates, Inc. (2)
16W070 West 83rd Street
Burr Ridge, IL 60521
Attn: R. Henry
M. Plys

Peter Bieniarz
Risk Management Associates
2309 Dietz Farm Road, NW
Albuquerque, NM 87107

Dr. K. Soda
Manager,
Chemical Engineering Safety Laboratory
Department of Nuclear Fuel Safety
Japan Atomic Energy Research Institute
Tokai-Muri, Naku-Gun, Ibaraki-Ken
319-11
JAPAN

K. Sato, Director
Department of Reactor Safety Research
Japan Atomic Energy Research Institute
Tokai-Mura, Naka-Gun, Ibaraki-Ken
JAPAN

P. Fehrenbach
Atomic Energy Canada, Ltd.
Chalk River, Ontario
CANADA KOJ IJO

M. Hayns
UKAEA
Safety and Reliability Directorate
Wigshaw Lane
Culcheth
Warrington WA3 4NE
Cheshire,
ENGLAND, U.K.

J. R. Mathews
Aere Harwell
Didcot
Oxfordshire OX11 ORA
ENGLAND, U.K.

F. Briscoe
UKAEA Culham Laboratory
Abingdon
Oxfordshire OX14 3DB
ENGLAND, U.K.

H. J. Teague (3)
UKAEA
Safety and Reliability Directorate
Wigshaw Lane
Culcheth
Warrington, WA3 4NE
ENGLAND, U.K.

M. Jankowski
IAEA
Division of Nuclear Reactor Safety
Wagranerstrasse 5
P.O. Box 100
A/1400 Vienna, AUSTRIA

Statens Karnkraftinspektion
L. Hammer
P. O. 27106
S-10252 Stockholm, SWEDEN

Studsvik Energiteknik AB
K. Johansson
S-611 82 Nykoping, SWEDEN

Atomic Energy Canada Ltd.
M. Notley
Chalk River, Ontario
CANADA KOJ 1JO

Atomic Energy Canada Ltd. (2)
Pinawa, Manitoba
CANADA ROE 1LO
Attn: H. Rosinger
D. Wren

Sandia Distribution:

3141	S. A. Landenberger (5)
3151	W. I. Klein
6400	D. J. McCloskey
6412	A. L. Camp
6413	E. Bergeron
6415	R. M. Cranwell
6420	J. V. Walker
6421	P. S. Pickard
6422	D. A. Powers (5)
6422	F. E. Arellano
6422	J. E. Brockmann (2)
6422	E. R. Copus
6422	T. M. Kerley
6422	D. A. Lucero
6422	W. W. Tarbell (5)
6423	B. W. Marshall, Jr.
6425	W. J. Camp
6425	M. Pilch (5)
6427	M. Berman
6427	L. Pong
6429	K. D. Bergeron
6429	D. E. Carroll
6429	J. L. Tills
6429	K. E. Washington
6429	D. C. Williams
6440	D. A. Dahlgren
6442	W. A. Von Riesemann
6454	G. L. Cano
7530	T. B. Lane
7537	N. R. Keltner
8363	W. Sanders
8363	K. Marx
8524	P. W. Dean

NRC FORM 335 (2-84) NRCM 1102, 3201, 3202

U.S. NUCLEAR REGULATORY COMMISSION

BIBLIOGRAPHIC DATA SHEET

SEE INSTRUCTIONS ON THE REVERSE

1. REPORT NUMBER (Assigned by TIDC, add Vol. No., if any)

NUREG/CR-4914
SAND87-0940

2. TITLE AND SUBTITLE

THE INFLUENCE OF SELECTED CONTAINMENT STRUCTURES ON DEBRIS DISPERSAL AND TRANSPORT FOLLOWING HIGH PRESSURE MELT EJECTION FROM THE REACTOR VESSEL

3. LEAVE BLANK

4. DATE REPORT COMPLETED

MONTH	YEAR
July	1988

5. AUTHOR(S)

M. Pilch, W. W. Tarbell and J. E. Brockmann

6. DATE REPORT ISSUED

MONTH	YEAR
September	1988

7. PERFORMING ORGANIZATION NAME AND MAILING ADDRESS (Include Zip Code)

Sandia National Laboratories
Albuquerque, NM 87185

8. PROJECT/TASK/WORK UNIT NUMBER

9. FIN OR GRANT NUMBER

A1406

10. SPONSORING ORGANIZATION NAME AND MAILING ADDRESS (Include Zip Code)

Division of Systems Research
Office of Nuclear Regulatory Research
U.S. Nuclear Regulatory Commission
Washington, DC 20555

11a. TYPE OF REPORT

Technical

b. PERIOD COVERED (Inclusive dates)

12. SUPPLEMENTARY NOTES

13. ABSTRACT (200 words or less)

High pressure expulsion of molten core debris from the reactor pressure vessel may result in dispersal of the debris from the reactor cavity. In most plants, the cavity exits into the containment such that the debris impinges on structures. Retention of the debris on the structures may affect the further transport of the debris throughout the containment. Two tests were done with scaled structural shapes placed at the exit of 1:10 linear scale models of the Zion cavity. The results show that the debris does not adhere significantly to structures. The lack of retention is attributed to splashing from the surface and reentrainment in the gas flowing over the surface. These processes are shown to be applicable to reactor scale.

A third experiment was done to simulate the annular gap between the reactor vessel and cavity wall. Debris collection showed that the fraction of debris exiting through the gap was greater than the gap-to-total flow area ratio. Film records indicate that dispersal was primarily by entrainment of the molten debris in the cavity.

14. DOCUMENT ANALYSIS – a. KEYWORDS/DESCRIPTORS

DCH, Direct Containment Heating; HPME, High Pressure Melt Ejection; Structures; Hole Ablation, Reactor Safety

b. IDENTIFIERS/OPEN-ENDED TERMS

15. AVAILABILITY STATEMENT

Unlimited

16. SECURITY CLASSIFICATION

(This page)

Unclassified

(This report)

Unclassified

17. NUMBER OF PAGES

18. PRICE

☆U.S. GOVERNMENT PRINTING OFFICE:1988-241-590:80206